ABSTRACT

COFFER, MEGAN MICHELLE. Eyes in the Sky Lend Support for Water Quality Monitoring across Inland and Coastal Environments. (Under the direction of Dr. Helena Mitasova).

Aquatic environments play a prominent role in the United States (US), supporting aquatic life, offering recreational opportunities, and serving as sources of drinking water. It is critical to develop tools for understanding the distribution of both the stressors affecting aquatic environments, including cyanobacterial blooms, and the benefits they provide, including seagrass ecosystems. Cyanobacteria occur naturally, but under the right environmental conditions, they can proliferate leading to harmful cyanobacterial blooms. Seagrasses provide many ecosystem services and act as an indicator of ecosystem health.

Traditionally, field observations are used to monitor cyanobacteria and map seagrass; However, these efforts can be costly. Resources managers require accurate and inexpensive tools to determine the spatio-temporal extent of stressors and services in aquatic systems. Satellite remote sensing can offer a cost-effective complement to field observations. While previous studies have supported the use of satellites for both cyanobacterial monitoring and seagrass mapping, those monitoring cyanobacteria have done so at small spatial scales and those mapping seagrass have not presented transparent guidelines, limiting reproducibility. This dissertation explores the use of both freely available and commercial, high-resolution satellites to map aspects of aquatic resources that are critically important for managers and decision-makers.

Chapter 2 offers the first national assessment quantifying the number of lakes across the continental US (CONUS) impacted by cyanobacterial blooms on a weekly basis. At over 2,000 lakes across CONUS, satellite imagery from the Envisat MEdium Resolution Imaging Spectrometer was obtained for 2008 through 2011, and from the Ocean and Land Colour Instrument (OLCI) for 2017 and 2018. Four thresholds to define when a lake was classified as

experiencing a bloom were explored by comparing results across seasons and lake sizes. National cyanobacterial bloom percentage followed well-documented patterns, peaking in late summer and early fall. Regional results were similar, except in the Southeast and South where bloom percentage peaked in the winter. Results throughout the manuscript were largely based on a 10% spatial area threshold as a threshold based on percent surface area rather than number of pixels had the lowest error across seasons and lake sizes.

Chapter 3 presents the first large-scale assessment of cyanobacterial frequency and abundance at surface drinking water intakes across CONUS. OLCI imagery spanning June 2016 through April 2020 at 685 drinking water sources was analyzed. A subset of satellite data was compared to responses submitted through the U.S. EPA's fourth Unregulated Contaminant Monitoring Rule. Overall agreement was 94%. Temporal frequency of cyanobacterial blooms at all 685 drinking water sources was assessed. In 2019, bloom frequency averaged 2% and peaked at 100%, where 100% indicated a bloom was always present at the source waters when satellite imagery was available. Monthly cyanobacterial abundances were used to assess short-term trends. Generally, 2016-2020 was an insufficient time period for confidently observing changes, instead requiring a decade of data. Five source waters did demonstrate a sustained trend, with one increasing and four decreasing.

Chapter 4 compares two commercial satellites, DigitalGlobe's WorldView-2 and Planet's RapidEye, for delineating seagrass. A single scene from each platform was obtained at St. Joseph Bay in Florida. A reproducible processing regime was developed to transform imagery into analysis-ready data. Satellite-derived surface reflectances were compared against field measurements. WorldView-2 exhibited high disagreement in shorter wavelengths, chronically overpredicting. RapidEye had lower overall disagreement, overpredicting slightly. A deep

convolutional neural network was used to classify imagery into deep water, land, submerged sand, seagrass, and intertidal classes. Results were compared to photointerpreted aerial imagery. Agreement was 96% to 97%, supporting the use of both WorldView-2 and RapidEye for seagrass mapping. The semi-automated workflow presented here can be used to map seagrass across large spatial areas.

Eyes in the Sky lend Support for Water Quality Monitoring across Inland and Coastal Environments

by
Megan Michelle Coffer

A dissertation submitted to the Graduate Faculty of
North Carolina State University
in partial fulfillment of the
requirements for the degree of
Doctor of Philosophy

Geospatial Analytics

Raleigh, North Carolina
2021

APPROVED BY:

Helena Mitasova Committee Chair	Blake Schaeffer
Natalie Nelson	Daniel Obenour

BIOGRAPHY

Megan was born in Frederick, Maryland and was raised in Fairfield, Pennsylvania; Ijamsville, Maryland; Greenville, North Carolina; and Miami, Florida before moving to Raleigh, NC for college. During her undergraduate studies at Meredith College, Megan began working as an undergraduate research assistant at North Carolina State University in the department of Marine, Earth and Atmospheric Science. After receiving her B.S. in Mathematics with minors in Statistics and Psychology in 2015, she began pursuing her M.S. in atmospheric science under the guidance of Dr. Erin Lee Hestir. Her thesis focused on analyzing micrometeorological flux tower data in Arctic wetlands, and through this research, she was introduced to satellite remote sensing. After receiving her M.S. in 2017, Megan began as an Oak Ridge Institute of Science and Education fellow with Dr. Blake Schaeffer at the U.S. Environmental Protection Agency in Durham, NC using satellite imagery to study water quality. A year into her fellowship, Megan decided to return to graduate school to complete her Ph.D. in Geospatial Analytics working under the guidance of Dr. Helena Mitasova. Megan completed her degree in Spring 2021 before transitioning to a post-doctoral fellow in the same research lab at the U.S. EPA.

ACKNOWLEDGMENTS

First and foremost, I thank my mentors at the U.S. EPA, Blake Schaeffer and John Darling, for instilling a sense of confidence in me that transcended research. I thank my committee chair, Helena Mitasova, for her guidance and leadership throughout my time as a graduate student, including as both a Master's student and as a Doctoral student, and my other committee members, Natalie Nelson and Daniel Obenour, for their thoughtful suggestions and expertise. Thank you to Ross Meentemeyer for your flexibility and your willingness to allow me to participate in my fellowship while completing my degree, and to Rachel Kasten for answering countless emails from me over the years. To Erin Hestir, thank you for introducing me to remote sensing and for turning a theoretical mathematician into a scientific researcher. I thank my colleagues and friends at the U.S. EPA: Erin Urquhart, Wilson Salls, Cindy Lebrasse, Peter Whitman, David Graybill, Marirosa Molina, Huiyun Wu, and Jeff Minucci. And thank you to the members of the GeoForAll lab group, both past and present, at NC State University, and a special thank you to cohort members Nikki Inglis and Kellyn Montgomery for their friendship and positivity. Lastly, this research would not have been possible without support and guidance from my colleagues in cyanobacteria: Keith Loftin, Jeremy Werdell, Rick Stumpf, Katie Foreman, Alex Porteous, and Ryan Albert; and from my colleagues in seagrass: Victoria Hill, Dick Zimmerman, and Jiang Li.

TABLE OF CONTENTS

LIST OF TABLES

LIST OF FIGURES

CHAPTER 1: INTRODUCTION

Aquatic environments play a prominent role in the United States (US), supporting aquatic life, offering recreational opportunities, and serving as sources of drinking water. According to the U.S. Census, 94.7 million people, or nearly 30% of the total US population, lived in coastal counties in 2017 (U.S. Census Bureau, 2019). Inland lakes across the US offer prime recreational opportunities that attract millions of visitors each year, including the 7.5 million people who visited Lake Mead in 2019 (National Park Service, 2020), the nearly 5.6 million people who visited the Finger Lakes Region in 2018, and the estimated 20 million people who visit Lake Tahoe each year. Public water systems delivered over 23 billion gallons of surface water per day in 2015 for domestic water use in the US, serving an estimated 283 million people, representing nearly 90% of the US population (Dieter et al., 2018).

Healthy aquatic ecosystems are important for local economies and for human well-being, and it is therefore critical to develop tools for understanding the distribution of both the stressors affecting them and the benefits that these resources provide. For example, cyanobacteria are naturally occurring organisms that exist in many waterbodies. The presence of cyanobacteria is not necessarily problematic, but under the right environmental conditions, cyanobacteria can proliferate leading to harmful cyanobacterial blooms. These harmful cyanobacterial blooms can negatively impact human health (World Health Organization, 2003), ecosystem health (Zanchett and Oliveira-Filho, 2013) and can have negative economic impacts (Steffensen, 2008). Understanding the distribution and frequency of cyanobacterial bloom events can therefore provide essential information to natural resource managers. Similarly, mapping the distribution of services provided by aquatic systems can assist with conservation planning. In coastal environments, for instance, seagrasses act as an indicator of ecosystem health, where changes in abundance and distribution can signify environmental stressors (Congdon et al., 2018). Seagrasses can respond to natural and anthropogenic disturbances rapidly over periods of a few weeks to months (Roca et al., 2016).

Traditionally, field observations are used to monitor cyanobacterial blooms and to map seagrass extent. Field observations of cyanobacteria are typically collected by gathering water samples or through visual observation. Field observations of seagrass extent are typically achieved through photointerpretations of aerial imagery collected via aircraft and field surveys. Large-scale assessments of costs incurred to both monitor cyanobacterial blooms in inland systems and map seagrass extent along coastal systems can be difficult to obtain. However, a few small-scale cost estimates have been noted in the literature. To monitor harmful algal blooms, the Washington State Department of Ecology estimated laboratory costs of event response samples for the state at $60,000 USD annually and staff expenses at $150,000 USD annually (Anderson-Abbs et al., 2016). In Australia, the annual cost of cyanobacterial monitoring and for contingency planning in the event of a bloom was valued at $6.6 USD in 2000 (Atech, 2000). In New Zealand, monitoring costs for a single cyanobacterial bloom in the Waikoto River were valued at $36,000 USD over a three-month period in 2003 (Kouzminov, Ruck, and Wood 2007). To map seagrass extent, a 2011 report by Florida Fish & Wildlife Services estimated the total cost of mapping seagrass one time for the entire coast of Florida using digital aerial imagery and conventional photointerpretation to be about $1.36 million USD, equivalent to $1.57 million today, excluding staff salary expenses (Yarbro and Carlson Jr., 2011).

Satellite remote sensing can offer a cost-effective complement to field observations. For example, Papenfus et al. (2020) valued services provided through remote sensing monitoring programs of chlorophyll *a* at $5.7 million annually for satellite-resolvable lakes and reservoirs in the US. Using a 2018 cyanobacterial bloom in Utah Lake as a case study, socio-economic costs avoided through the use of satellite data as a monitoring tool for this single event were valued at $370,000 (Stroming et al., 2020). While exact cost savings have not been estimated for seagrass mapping, Baumstark et al. (2013) found that satellite remote sensing can offer a cost-effective approach for mapping and monitoring seagrass in coastal ecosystems.

In addition to cost savings, satellite remote sensing can offer improved temporal resolution compared to field monitoring. Since most satellite platforms have collected imagery continuously since launch, satellite data can offer the advantage of historical archives which can then be used to assess trends over time or to put current observations in the context of long-term conditions. Specific to inland water quality measurements, the majority (85%) of field observations are collected from April through September (Schaeffer et al., 2018), but cyanobacterial blooms can occur year-round. In coastal environments, seagrass mapping is conducted at temporal scales ranging from annually to every several years. One of the longest lasting and consistent monitoring programs is conducted through the Virginia Institute of Marine Science Submerged Aquatic Vegetation program, which has mapped much of the Chesapeake Bay via aerial imagery annually since 1984. The Southwest Florida Water Management District has mapped seagrass for several coastal locations in Florida five times since 2004, but data collection is inconsistent and many coastal locations have never been mapped for seagrass coverage.

While previous studies have supported the use of satellite remote sensing for both cyanobacterial monitoring and seagrass mapping, those monitoring cyanobacterial blooms have done so on a relatively small spatial scale and those mapping seagrass extent have not presented transparent guidelines, limiting reproducibility. This dissertation explores the feasibility of developing reproducible methods to monitor cyanobacterial blooms in inland freshwater systems and map seagrass extent along the coast with direct application utility through the use of various remote sensing technologies. This dissertation is presented as three manuscripts, each as its own chapter, two of which have been published in the peer-reviewed journals *Ecological Indicators* (Chapter 2) and *Remote Sensing of Environment* (Chapter 4), and one of which is currently in clearance to be submitted for review in *Water Research* (Chapter 3). These chapters focus on unique, but related, research questions. The overall objective of this dissertation use both freely available and commercial, high-resolution satellites to map aspects of aquatic resources that are critically important for managers and decision-makers. This objective is achieved by developing reproducible workflows for both cyanobacterial monitoring and seagrass extent mapping. More specifically, each chapter addresses the following aims:

- Chapter 2: Propose methods to assess the occurrence of cyanobacterial blooms across the US by quantifying the number of lakes impacted by blooms on a weekly basis using satellite imagery at over 2,000 lakes.
- Chapter 3: Propose methods to assess the abundance and temporal frequency of cyanobacterial blooms using satellite data at source waters for nearly 700 drinking water intakes across the US.

- Chapter 4: Develop a reproducible workflow for processing satellite imagery from two commercial satellite platforms and apply an image classification approach to this processed imagery to map seagrass extent.

Chapter 2 offers the first national-scale assessment quantifying the number of lakes across the US impacted by cyanobacterial blooms on a weekly basis. This assessment leveraged observations from the European Space Agency's MEdium Resolution Imaging Spectrometer (MERIS) onboard Envisat spanning 2008 through 2011 and the Ocean and Land Colour Instrument (OLCI) onboard Sentinel-3A spanning 2017 through 2018. Cyanobacterial occurrence was also assessed at the regional scale and the resulting seasonality was compared to published ecological patterns. Additionally, this study considers different ways of categorizing a lake as experiencing a cyanobacterial bloom based on lake surface area and how these categorizations can influence derived results. While several surface area thresholds have been used previously, including a spatial area threshold of 25% in Hu et al. (2010), 10%, 40%, and 60% in Qin et al. (2015), and 30% in Davis et al. (2019), there are no recommendations in the literature on what threshold should be used, and no studies have explored differences that could arise in results based on the threshold chosen.

Findings from Chapter 2 characterize the number of lakes affected by cyanobacterial blooms on a weekly basis for the years 2008 through 2011, 2017, and 2018. At the national scale, results followed ecological expectations with cyanobacterial blooms peaking in late summer and early fall, a finding supported through previous phenology studies (Xu et al., 2017; Graham et al., 2017; Lugliè et al., 2017). Data coverage in the wintertime was limited, particularly in northern latitude states, due to snow and ice cover during which satellite images were quality flagged and discarded according to Urquhart & Schaeffer (2020). At the regional scale, cyanobacterial occurrence mirrored patterns seen at the national scale for all climate regions except for the South and the Southeast. In the South and Southeast, bloom occurrence reached maximum values in the winter months and reached minimum values in the summer months, a pattern contrary to that seen at the national scale. A case study at Lake Jesup in Florida was explored using field data to confirm patterns observed through satellite imagery. Several possible explanations were addressed, including environmental conditions and satellite artifacts, but further research is needed. In classifying when a lake is experiencing a cyanobacterial bloom, thresholds of 1 pixel, 10% surface area, 20% surface area, and 30% surface area were explored, and differences in these thresholds across seasons and lake sizes were considered. A threshold of 1 pixel was found to be more prone to error when analyzing both seasonal differences and the effect of lake size. Therefore, a threshold based on spatial coverage of a bloom is suggested. While the three percentages considered all appeared to perform fairly equally, results presented throughout the manuscript are largely based on a spatial area threshold of 10%. That threshold had relatively low error across seasons and lake sizes, and exhibited the most consistency during the summer months, when at least recreational exposure to cyanobacterial blooms is highest.

In addition to providing phenological validation of the cyanobacteria index algorithm used by the CyAN project and suggesting an area threshold at which cyanobacterial blooms should be classified, results from Chapter 2 will be used to monitor the state of the environment in the US through the U.S. EPA’s Report on the Environment (ROE; https://www.epa.gov/report-environment). This work was selected as a ROE indicator for tracking water quality of fresh surface waters and is currently in the clearance process for publication on the website. ROE indicators provide environmental policy decision makers and others with scientifically defensible, up-to-date, objective, and relevant indicator-based products that are of national importance for protecting human health and the environment.

Chapter 3 also focuses on characterizing cyanobacterial booms at the national scale by quantifying the temporal frequency and abundance of blooms at source waters for nearly 700 drinking water intakes across the US. This assessment leveraged OLCI imagery in addition to qualitative responses provided as part of the fourth Unregulated Contaminant Monitoring Rule (UCMR 4). UCMR requires public water systems to monitor for contaminants currently unregulated in drinking water every five years, and microcystin, a toxin produced by some cyanobacterial blooms, was included as one of these contaminants in UCMR 4 collected from 2018 through 2020. First, satellite-derived cyanobacterial presence/absence and abundance were compared to qualitative UCMR 4 responses as an independent validation of both datasets. Next, the temporal frequency of cyanobacterial blooms at source waters was analyzed for the year 2019 by finding the percentage of valid satellite pixels (i.e., those not quality flagged and discarded) that indicated a bloom was present. Finally, a formal trend analysis was performed on cyanobacterial abundance measurements across source waters, spanning June 2016 when OLCI imagery first became available through April 2020, to determine if cyanobacterial abundance was increasing, decreasing, or staying the same at drinking water sources. Effect size was computed to provide insight on the data requirements for identifying temporal trends in cyanobacterial abundance.

Findings from Chapter 3 offer a quantitative assessment regarding the frequency in which cyanobacterial blooms occur at source waters near drinking water intakes across the US, although these findings do not characterize such levels in finished drinking water. A total of 685 drinking water sources across 44 US states can be monitored using 300 m OLCI imagery. A comparison between 99 qualitative UCMR 4 responses and satellite-derived observations of cyanobacterial presence and absence at a subset of drinking water sources had 94% agreement, providing independent validation for both the quality of interpretations at each public water system and the algorithm employed in this study. Across all resolvable drinking water sources, not just those with UCMR 4 data, the temporal frequency of blooms had a median value of 2% and reached a maximum value of 100% at two drinking water sources, indicating that for every valid satellite observation, a cyanobacterial bloom was present. A trend analysis spanning June 2016 through April 2020 suggested that, generally, this time period was insufficient to identify trends in cyanobacterial abundance. Instead, a decade of data is generally needed for observed changes to outweigh variability inherent in the data. However, cyanobacterial abundance did change at five drinking water sources, increasing at one and decreasing at four.

Results presented in Chapter 3 have direct applications for both the U.S. EPA Office of Water, which in part ensures safe drinking water and implements the Clean Water Act and the Safe Drinking Water Act, and at the state level for both cyanobacterial monitoring support and as a tool for nutrient criteria considerations. The comparison between visual UCMR 4 responses and satellite-derived cyanobacterial estimates gives the U.S. EPA Office of Water greater confidence in the information provided by each drinking water utility. Additionally, it offers methods for expanding the comparison introduced here to include the entire UCMR 4 dataset once it becomes available. Findings presented in this study will be used by the U.S. EPA Office of Water as direct and concrete support of future regulatory and non-regulatory activities, including informing risk-management activities at drinking water utilities most impacted by cyanobacterial blooms while preventing the expenditure of significant public resources at those less impacted. At the state level, the temporal frequency metric presented here has been used to assess the status of cyanobacterial blooms in Oregon and Oklahoma. In 2018, vulnerable residents in the city of Salem, Oregon were under a “Do Not Drink” advisory for several weeks after elevated levels of cyanotoxins were detected in finished drinking water (The Novak Consulting Group, 2018). Preliminary frequency results were presented to the city of Salem for Detroit Lake to identify areas of high cyanobacterial frequency used to prioritize event response sampling. In Oklahoma, temporal frequency results for 71 drinking water sources across the state are being used to identify which intakes are most prone to cyanobacterial blooms and prioritize where additional sampling efforts should be targeted.

Chapter 4 focuses on coastal ecosystems rather than inland ecosystems and explores the application of remote sensing for mapping ecosystem services rather than stressors. This chapter investigates the applicability of two commercial satellite platforms for seagrass delineation. Seagrasses play a prominent role in the global carbon cycle, but the exact amount of carbon currently stored in these ecosystems is highly uncertain, primarily due to a poor understanding of global seagrass coverage with current estimates ranging nearly 30-fold, between 150,000 and 4,320,000 km^2 (Duarte, 2017). Commercial satellite platforms offer fine spatial resolution, which is an important consideration due to the patchy and heterogeneous nature of seagrass ecosystems (Hill et al., 2014). Although commercial satellite platforms have been leveraged for seagrass detection in previous studies, a consistent and transparent processing workflow has not been presented, which limits reproducibility. Additionally, the radiometric performance of commercial satellite imagery in aquatic environments has not been assessed. This study used St. Joseph Bay in Florida as a case study to assess the radiometric performance of a single scene from both DigitalGlobe's WorldView-2 satellite platform and Planet's RapidEye satellite constellation, and to analyze their performance for classifying seagrass coverage.

Findings from Chapter 4 introduced the first semi-automated and reproducible workflow for processing commercial satellite imagery from WorldView-2 and RapidEye. This workflow was created in ENVI/IDL (Exelis Visual Information Solutions, Boulder, Colorado) and applies radiometric calibration, atmospheric correction, rational polynomial coefficient orthorectification, and mosaicking. Atmospheric correction removes the influence of the atmosphere and is an important step in creating spectral separability necessary for image classification. Typically, atmospheric correction is implemented on a scene-specific basis, hindering reproducibility and large-scale image processing. Instead, the workflow presented as part of Chapter 4 applies both spatial and spectral masks to subset the image to just water pixels before analyzing the distribution of data values and automatically selecting the input parameters required to apply a dark object subtraction approach for atmospheric correction. This advancement allows for bulk processing of such imagery, required for larger scale mapping of seagrass. Processed imagery was compared to field observations of surface reflectance collected during image acquisition. WorldView-2 had higher disagreement with field observations than RapidEye, and had particular error in shorter wavelengths as demonstrated through a strong positive bias. RapidEye had lower overall disagreement than WorldView-2 and a slight positive bias compared to field data. Next, a deep convolution neural network (DCNN) developed by Islam et al. (2020) was used to classify image pixels into five classes: deep water, land, submerged sand, seagrass, and intertidal. Intertidal represents a zone along the land-water interface that would be submerged during high tide and exposed during low tide. Results were compared to an aerial photointerpretation collected approximately one month before the satellite imagery by the Florida Fish and Wildlife Conservation Commission (FL FWC). The WorldView-2 classified image had 97% agreement with the FL FWC photointerpretation, and, despite lower spatial and spectral resolutions, RapidEye had 96% agreement. This workflow was also demonstrated at St. George Sound and Tampa Bay, both in Florida.

The Scientific and Technical Advisory Committee (STAC), which provides scientific and technical guidance to the Chesapeake Bay Program on measures to restore and protect the Chesapeake Bay, held three workshops spanning October 2019 through February 2020 to explore the potential of integrating satellite imagery into the Chesapeake Bay submerged aquatic vegetation monitoring program. Recommendations set forth by STAC as a result of these workshops include the methods and results presented in Chapter 4, suggesting that WorldView-2 imagery processed and classified using the proposed workflow can be an effective approach for continued seagrass mapping throughout the Chesapeake Bay. Additionally, the processing regime proposed in Chapter 4 has already shown utility across time and space through research projects being conducting at the U.S. EPA: one project modified the presented workflow to apply it to Landsat imagery across a 30-year time series and another project has applied this workflow to WorldView-2 imagery at ten additional locations across the United States.

This dissertation provides tools for managers and decision-makers to monitor important aspects of aquatic resources and supports the use of satellite imagery, both obtained as freely available data and as commercial data, for mapping ecosystem stressors and services. Methods to assess cyanobacterial blooms across large spatial scales in inland ecosystems and for mapping seagrasses in coastal ecosystems are presented. Chapter 2 offers further validation of a common spectral shape algorithm used for quantifying cyanobacterial abundance that is also used for assessing the frequency of cyanobacterial blooms in Chapter 3. Both Chapter 2 and Chapter 3 further our understanding of cyanobacterial blooms in the US by offering the first large-scale analyses for over 2,000 large inland lakes (Chapter 2) and for nearly 700 drinking water sources (Chapter 3). Chapter 4 introduces a workflow for processing commercial satellite imagery that may be applied to multiple satellite scenes to classify seagrass across large areas.

The efforts put forth through this dissertation have also been frequently shared at the local, state, and national level, highlighting a unique and important contribution of this dissertation: direct communication and involvement with stakeholders. This communication involves both sharing of the information and technical guidance to assist in the transfer of these analyses to ensure methods presented here can continue to be used to study water quality. At the local level, cyanobacterial frequency results (Chapter 3) were used to prioritize event response sampling when a cyanobacterial bloom breached a drinking water intake. Additionally, the proposed workflow for processing and classifying commercial satellite imagery (Chapter 4) has been proposed to monitor submerged aquatic vegetation throughout the Chesapeake Bay. At the state level, temporal frequency results are being used by the state of Oklahoma to prioritize sampling and understand nutrient loading criteria across 71 drinking water sources (Chapter 3). At the national level, cyanobacterial occurrence results are being implemented into the U.S. EPA report on the environment as a scientifically defensible, up-to-date, objective, and relevant product for understanding how many lakes across the US are impacted by cyanobacterial blooms on a weekly basis (Chapter 2). Additionally, results quantifying the temporal frequency of cyanobacterial blooms at nearly 700 drinking water sources is of direct benefit to the U.S. EPA Office of Water to prioritize resources (Chapter 3). Lastly, methods presented to process and classify commercial satellite imagery are being implemented at locations across the US to quantify the spatial coverage of seagrasses, an important step toward understanding their global carbon storage capacity (Chapter 4). The efforts outlined in this dissertation have immediate implications for management of water quality across broad spatial and temporal scales and are actively being used for decision making relevant for cyanobacterial bloom monitoring and seagrass mapping.

REFERENCES

Anderson-Abbs, B., Howard, M., Taberski, K., Worcester, K., 2016. California Freshwater Harmful Algal Blooms Assessment and Support Strategy.

Atech, 2000. Cost of algal blooms. Report to Land and Water Resources Research and Development Corp.

Baumstark, R., Dixon, B., Carlson, P., Palandro, D., Kolasa, K., 2013. Alternative spatially enhanced integrative techniques for mapping seagrass in Florida's marine ecosystem. International Journal of Remote Sensing 34, 1248–1264. doi:10.1080/01431161.2012.721941.

Congdon, V.M., Dunton, K.H., Brenner, J., Goodin, K.L., Ames, K.W., 2018. Chapter 4. Ecological Resilience Indicators for Seagrass Ecosystems. https://www.natureserve.org/sites/default/files/chapter_4_-_seagrass_indicators.pdf.

Davis, T.W., Stumpf, R., Bullerjahn, G.S., McKay, R.M.L., Chaffin, J.D., Bridgeman, T.B., Winslow, C., 2019. Science meets policy: a framework for determining impairment designation criteria for large waterbodies affected by cyanobacterial harmful algal blooms. Harmful Algae 81, 59-64. 10.1016/J.HAL.2018.11.016.

Dieter, C.A., Maupin, M.A., Caldwell, R.R., Harris, M.A., Ivahnenko, T.I., Lovelace, J.K., Barber, N.L., Linsey, K.S., Survey, U.S.G., 2018. Estimated use of water in the United States in 2015, U.S. Geological Survey Circular 1441. https://doi.org/10.3133/cir1441

Duarte, C.M., 2017. Reviews and syntheses: hidden forests, the role of vegetated coastal habitats in the ocean carbon budget. Biogeosciences, 14, 301-310. 10.5194/bg-14-301-2017.

Graham, J.L., Foster, G.M., Kramer, A.R., 2017. Twenty years of water-quality studies in the Cheney Reservoir Watershed, Kansas, 1996-2016. Technical Report. Reston, VA. https://doi.org/10.3133/fs20173019.http://pubs.er.usgs.gov/publication/fs20173019.

Hill, V. J., Zimmerman, R. C., Bissett, W. P., Dierssen, H., Kohler, D.D.R., 2014. Evaluating light availability, Seagrass biomass, and productivity using hyperspectral airborne remote sensing in Saint Joseph's bay, Florida. Estuaries and Coasts, 37, 1467-1489. 10.1007/s12237-013-9764-3.

Hu, C., Lee, Z., Ma, R., Yu, K., Li, D., Shang, S., 2010. Moderate Resolution Imaging Spectroradiometer (MODIS) observations of cyanobacteria blooms in Taihu Lake, China Journal of Geophysical Research: Oceans, 115. 10.1029/2009JC005511.

Islam, K. A., Hill, V., Schaeffer, B., Zimmerman, R., Li, J., 2020. Semi-supervised adversarial domain adaptation for seagrass detection using multispectral images in coastal areas Data Science and Engineering, 5(2), 111-125. 10.1007/s41019-020-00126-0.

Kouzminov, A., Ruck, J. Wood, S.A., 2007. New Zealand risk management approach for toxic cyanobacteria in drinking water. Australian and New Zealand Journal of Public Health, 31, 275-281. https://doi.org/10.1111/j.1467-842X.2007.00061.x.

Luglià, A., Giacobbe, M. G., Riccardi, E., Bruno, M., Pigozzi, S., Mariani, M.A., Satta, C.T., Bazzoni, A., M., Caddeo, T., Farina, P., Padedda, B.M., Pulina, S., Sechi, N., Miladri, A., 2017. Paralytic shellfish toxins and cyanotoxins in the Mediterranean: New data from Sardinia and Sicily (Italy). Microorganisms. 10.3390/microorganisms5040072.

National Park Service (2020). Annual Park Ranking Report for Recreation Visits in: 2019. Retrieved from [https://irma.nps.gov/STATS/SSRSReports/National%20Reports/Annual%20 Park%20Ranking%20Report%20(1979%20-%20Last%20Calendar%20Year)].

Papenfus, M., Schaeffer, B., Pollard, A.I., Loftin, K., 2020. Exploring the potential value of satellite remote sensing to monitor chlorophyll-a for US lakes and reservoirs. Environmental Monitoring and Assessment, 192(808). https://doi.org/10.1007/s10661-020-08631-5.

Qin, B., Li, W., Zhu, G., Zhang, Y., Wu, T., Gao, G., 2015. Cyanobacterial bloom management through integrated monitoring and forecasting in large shallow eutrophic Lake Taihu (China) Journal of Hazardous Materials, 287, 356-363, 10.1016/j.jhazmat.2015.01.047.

Ritchie, J.C., Zimba, P.V., Everitt, J.H., 2003. Remote sensing techniques to assess water quality. Photogrammetric engineering & remote sensing. 69(6) 675-704.

Roca, G., Alcoverro, T., Krause-Jensen, D., Balsby, T.J.S., M. van Katwijk, N. Marbà, R. Santos, R. Arthur, O. Mascaró, Y. Fernández-Torqemada, M. Pérez, C.M. Duarte, and J. Romero, 2016. Response of seagrass indicators to shifts in environmental stressors: A global review and management synthesis. Ecological Indicators 63: 310–323.

Schaeffer, B. A., Iiames, J., Dwyer, J., Urquhart, E., Salls, W., Rover, R., Seegers, B, 2018. An initial validation of Landsat 5 and 7 derived surface water temperature for US lakes, reservoirs, and estuaries. International Journal of Remote Sensing, 39(22), 7789–7805. https://doi.org/10.1080/01431161.2018.1471545.

Schaeffer, B.A., Loftin, K.A., Stumpf, R.P., Werdell, P.J., 2015. Agencies collaborate, develop a cyanobacteria assessment network. Eos, Earth Sp. Sci. News 96. https://doi.org/10.1029/2015EO038809.

Steffensen, D.A., 2008. Economic cost of cyanobacterial blooms. In Cyanobacterial harmful algal blooms: State of the science and research needs, 855-865. Springer, New York, NY.

Stroming, S., Robertson, M., Mabee, B., Kuwayama, Y., Schaeffer, B., 2020. Quantifying the Human Health Benefits of Using Satellite Information to Detect Cyanobacterial Harmful

Algal Blooms and Manage Recreational Advisories in U.S. Lakes. GeoHealth 4, e2020GH000254. https://doi.org/10.1029/2020GH000254.

The Novak Consulting Group, 2018. City of Salem Water Advisory After-Action Assessment.

Urquhart, E.A., Schaeffer, B.A., 2019. Envisat MERIS and Sentinel-3 OLCI satellite lake biophysical water quality flag dataset for the contiguous United States. Data in Brief, 104826. https://doi.org/10.1016/j.dib.2019.104826.

U.S. Census Bureau, 2019. 94.7M Americans Live in Coastline Regions. Retrieved from [https://www.census.gov/library/stories/2019/07/millions-of-americans-live-coastline-regions.html].

World Health Organization, 2003. Algae and Cyanobacteria in Fresh Water, in: Guidelines for Safe Recreational Water Environments. 136–158.

Xu, H., Paerl, H.W., Zhu, G., Qin, B., Hall, N.S., Zhu, M., 2017. Long-term nutrient trends and harmful cyanobacterial bloom potential in hypertrophic Lake Taihu, China. Hydrobiologia, 787, 229-242. 10.1007/s10750-016-2967-4.

Yarbro, L., Carlson Jr., P., 2011. Seagrass Integrated Mapping and Monitoring for the State of Florida Mapping and Monitoring Report No. 1. Technical Report. Florida Fish and Wildlife Conservation Commission Fish and Wildlife Research Institute. St. Petersburg, USA.

Zanchett, G., Oliveira-Filho, E.C., 2013. Cyanobacteria and cyanotoxins: from impacts on aquatic ecosystems and human health to anticarcinogenic effects. Toxins (Basel). 5, 1896–1917.

CHAPTER 2: QUANTIFYING NATIONAL AND REGIONAL CYANOBACTERIAL OCCURRENCE IN US LAKES USING SATELLITE REMOTE SENSING

Published in Ecological Indicators April 2020 (https://doi.org/10.1016/j.ecolind.2019.105976)

Authors

Megan M. Coffer[1,2], Blake A. Schaeffer[3], John A. Darling[3], Erin A. Urquhart[1], Wilson B. Salls[1]

Affiliations

[1]ORISE Fellow, U.S. Environmental Protection Agency, Office of Research and Development, National Exposure Research Laboratory, USA

[2]Center for Geospatial Analytics, North Carolina State University, Raleigh, NC, USA

[3]U.S. Environmental Protection Agency, Office of Research and Development, National Exposure Research Laboratory, USA

Acknowledgements

This work was supported by the NASA Ocean Biology and Biogeochemistry Program/Applied Sciences Program (proposal 14-SMDUNSOL14-0001) and by U.S. EPA, NOAA, U.S. Geological Survey Toxic Substances Hydrology Program, and Oak Ridge Institute for Science and Technology (ORISE). This article has been reviewed by the National Exposure Research Laboratory and approved for publication. Mention of trade names or commercial products does not constitute endorsement or recommendation for use by the U.S. Government. The views expressed in this article are those of the authors and do not necessarily reflect the views or policies of the U.S. EPA. Portions of this analysis were included as a conference proceeding appearing originally as "A method for quantifying the number of US lakes with cyanobacterial harmful algal blooms using satellite remote sensing" in Proceedings Volume 10767, Remote Sensing and Modeling of Ecosystems for Sustainability XV. This conference proceeding was published in 2018 with the following authors: M. M. Coffer, Blake A. Schaeffer, Erin A. Urquhart, John A. Darling, and Wilson B. Salls. Field observations at Lake Jesup were obtained

from Florida LAKEWATCH (http://lakewatch.ifas.ufl.edu/), School of Forest Resources and Conservation, Institute of Food and Agricultural Sciences, University of Florida.

Abstract

Cyanobacterial harmful algal blooms are the most common form of harmful algal blooms in freshwater systems throughout the world. However, in situ sampling of cyanobacteria in inland lakes is limited both spatially and temporally. Satellite data has proven to be an effective tool to monitor cyanobacteria in freshwater lakes across the United States. This study uses data from the European Space Agency Envisat MEdium Resolution Imaging Spectrometer and the Sentinel-3 Ocean and Land Color Instrument to provide a national overview of the percentage of lakes experiencing a cyanobacterial bloom on a weekly basis for 2008–2011, 2017, and 2018. A total of 2321 lakes across the contiguous United States were included in the analysis. We examined four different thresholds to define when a waterbody is classified as experiencing a bloom. Across these four thresholds, we explored variability in bloom percentage with changes in seasonality and lake size. As a validation of algorithm performance, we analyzed the agreement between satellite observations and previously established ecological patterns, although data availability in the wintertime limited these comparisons on a year-round basis. Changes in cyanobacterial bloom percentage at the national scale followed the well-known temporal pattern of freshwater blooms. The percentage of lakes experiencing a bloom increased throughout the year, reached a maximum in fall, and decreased through the winter. Wintertime data, particularly in northern regions, were consistently limited due to snow and ice cover. With the exception of the Southeast and South, regional patterns mimicked patterns found at the national scale. The Southeast and South exhibited an unexpected pattern as cyanobacterial bloom percentage reached a maximum in the winter rather than the summer. Lake Jesup in Florida was used as a case study to validate this observed pattern against field observations of chlorophyll a. Results from this research establish a baseline of annual occurrence of cyanobacterial blooms in inland lakes across the United States. In addition, methods presented in this study can be tailored to fit the specific requirements of an individual system or region.

Keywords Remote sensing, Harmful algal blooms, Cyanobacteria, Water quality, Inland waters

1 Introduction

Cyanobacterial harmful algal blooms (cyanoHABs) are the most common form of harmful algal blooms in freshwater systems (Hudnell et al., 2008). While the classification of a harmful algal bloom has regional, seasonal, and species-specific aspects, generally, the term harmful algal bloom is a colloquial way of indicating when algal growth has resulted in negative environmental or health consequences (Smayda, 2003). Human exposure occurs through skin contact, accidental ingestion, inhalation during recreational activities, or the consumption of contaminated drinking water (Chorus et al., 2000). A wide range of health risks have been associated with human exposure to cyanobacteria including skin and eye irritation, adverse effects on liver and kidney function, and flu-like symptoms including headache, nausea, diarrhea, and vomiting (World Health Organization, 2003).

CyanoHABs occur worldwide and have been documented across the United States (Loftin et al., 2016). The significance of several recent bloom events has increased national awareness of cyanoHABs. In 2010, Grand Lake St. Marys in Ohio experienced an extensive cyanobacterial bloom that killed thousands of fish and forced a “No Contact” advisory to be issued for the lake. An event in Lake Erie resulted in over half a million people being left without access to clean drinking water in the City of Toledo, Ohio in 2014 (Sonich-Mullin, 2014). Lake Okeechobee in Florida experienced a substantial bloom in 2016 that spread to the coast, prompting a state of emergency in four coastal counties (Neuhaus, 2016).

Traditionally, in situ sampling has been used to assess the status of a bloom in a specific lake. However, these efforts are often limited both spatially and temporally due to the time and cost associated with collecting data. These considerations have encouraged exploration of alternative means for assessing cyanoHAB status. Satellite data has proven to be an effective monitoring tool for inland lakes across the United States (Clark et al., 2017; Stumpf et al., 2016b, 2016a; Urquhart et al., 2017).

While satellite technology cannot currently be used to detect toxins (Stumpf et al., 2016a), it can be used effectively to identify cyanobacterial blooms (Wynne et al., 2008) and to quantify cyanobacterial abundance (Kutser, 2009). Satellite data also has the potential to provide fairly frequent observations both temporally and spatially, although wintertime data are still limited due to snow and ice cover. Estimates of cyanobacteria concentration from satellite data offer a cost-effective approach to fill in temporal and spatial gaps when field sampling is not feasible and when cloud- and ice-free observations are possible.

Several studies have used satellite remote sensing to define the onset or quantify the duration of a cyanobacterial bloom by setting a minimum threshold based on the spatial coverage of the bloom. However, there is no consensus on what this threshold should be, and there are no recommendations regarding differences that might arise based on the threshold chosen. Zhang et al. (2012) defined the onset of cyanobacteria as the earliest date at which cyanobacterial blooms were first recorded by remote sensing. Using satellite observations from Taihu Lake in China, Hu et al. (2010a) defined a significant bloom as one that covered 25% of the surface area. Qin et al. (2015) set thresholds at 10%, 40%, and 60% of the lake surface area to define three risk management levels. Most recently, Davis et al. (2019) used a threshold of 30% of the spatial area to classify a cyanobacterial bloom.

This study uses satellite remote sensing to report on the weekly percentage of lakes across the contiguous United States (CONUS) that are experiencing detectable cyanobacterial blooms. First, four different thresholds on spatial bloom area are explored for classifying whether a waterbody is experiencing a cyanobacterial bloom. Next, we qualitatively consider the agreement between satellite estimates of cyanobacterial occurrence and previously established ecological patterns. Data from the MEdium Resolution Imaging Spectrometer (MERIS) were employed from 2008 to 2011, and Sentinel-3A Ocean and Land Color Instrument (OLCI) data were used for 2017 and 2018. This study aims to address the following research questions:

1. How many large waterbodies nationally and regionally are impacted by cyanobacterial blooms throughout the year?
2. Does the satellite algorithm result in the expected seasonality relative to published ecological patterns?
3. Can satellite data be used to find the most appropriate spatial area threshold for classifying a waterbody as experiencing a cyanobacterial bloom?

2 Data and methods

2.1 Satellite observations

MERIS and OLCI are European Space Agency sensors onboard the Envisat and Sentinel-3A satellites, respectively. The MERIS archive includes a consistent time series over CONUS for the years 2008 through 2011. The OLCI sensor provides data for the years 2017 and 2018, and will be available to perform similar analyses in the future. The five-year data gap between the two sensors is a result of the Envisat mission ending in April 2012 due to a loss of communication with the satellite; no equivalent sensor was available until the launch of Sentinel-3A in February 2016.

Both sensors have a temporal resolution of approximately 2–3 days and a spatial resolution of 300 m at nadir, where nadir is defined as the point on the Earth surface directly below the satellite. With the inclusion of Sentinel-3B data in future analyses, temporal coverage will increase to near-daily across CONUS. Standard MERIS Level-1B data were obtained from the NASA Ocean Color website (https://oceandata.sci.gsfc.nasa.gov) and were processed as described in Urquhart and Schaeffer (2020).

A spectral shape algorithm was used to assess cyanobacteria presence, quantifying its abundance as the cyanobacteria index (CI). Originally described in Wynne et al. (2008), this spectral shape (SS) algorithm uses a baseline defined as a straight line drawn between the 665 nm and the 709 nm bands. If the fluorescence band (681) falls below the baseline between 709 nm and 665 nm, yielding a negative SS(681), cyanobacteria is likely present. In cases without cyanobacteria, the reflectance at 681 nm falls above the 709 nm and 665 nm baseline, yielding a positive SS(681).

This iteration of CI was found to potentially identify other erroneous blooms including chlorophytes (Wynne et al., 2013), causing false positives. To address this issue, the CI algorithm was updated in Lunetta et al. (2015) to examine the ability to separate cyanobacteria from other blooms using a derivative that includes the 620 nm band, which is sensitive to phycocyanin, where SS(665) with = 665 nm, + = 681 nm, and − = 620 nm. This condition was defined by Matthews et al. (2012) (Eqs. 3–4) to separate cyanobacteria from other blooms in

African lakes. The updated CI algorithm was termed in Lunetta et al. (2015) as the CI-multi. The CI-multi uses the CI to estimate biomass, but uses the spectral shape around the 665 nm band as an exclusion criterion. Elevated phycocyanin absorption is presumed to depress the reflectance at 620 nm (e.g., Simis et al. (2005)), causing SS(665) to change from negative to positive. Accordingly, when $SS(665) < 0$, cyanobacteria are presumed absent, and when $SS(665) > 0$, cyanobacteria are presumed present.

While this algorithm has evolved since its first application in Wynne et al. (2008), hereafter, it will be referred to as CI. CI was calculated for each pixel and for each satellite overpass. Observations were then aggregated into weekly composites that preserve the maximum value for each pixel. This algorithm has been well documented across several U.S. states including Florida, Ohio, Rhode Island, Massachusetts, New Hampshire, Vermont, Connecticut, and Maine (Clark et al., 2017; Lunetta et al., 2015); Lake Erie (Stumpf et al., 2016a); from 25 state health advisories in California, Oregon, New York, Idaho, New Jersey, Utah, and Vermont (Schaeffer et al., 2018); and was used by the Wyoming Department of Environmental Quality to issue eight health advisories in 2018 (e.g., in Big Sandy Reservoir (Wyoming DEQ, 2018a), Eden Reservoir (Wyoming DEQ, 2018b), and Pathfinder Reservoir (Wyoming DEQ, 2018c)).

2.2. National and regional coverage of waterbodies

Given the spatial resolution of both MERIS and OLCI (300 m at nadir), only lakes of sufficient size and shape were considered for analysis. Waterbodies used in this analysis were selected according to Urquhart and Schaeffer (2020). A total of 2,321 waterbodies across CONUS were classified as resolvable with at least one resolvable waterbody in each state, except for West

Virginia and Delaware, in which all lakes were either of insufficient size or shape to meet the criteria. These 2,321 waterbodies represent only 0.61% of the 379,097 lakes, ponds, and reservoirs included in the National Hydrography Dataset Plus version 2.0 (NHD). Waterbodies considered in this analysis ranged in size from approximately 0.75 km^2 to over 4,000 km^2 which limits this analysis to relatively large lakes and excludes smaller waterbodies across the United States.

Satellite pixels containing cloud cover, those that fell along the land-water interface, and those that contained snow and ice were discarded as they can confound the satellite signal. Discarding data that contained snow and ice led to some data gaps during the winter months, particularly in northern latitude states. Thus, central and southern latitude states have a more complete time series than northern latitude states. Although this does limit wintertime data in several regions, we can assume that at least recreational exposure to cyanobacteria is limited when snow and ice are present in a waterbody.

To investigate the percentage of lakes experiencing a bloom at a regional level, we used the nine U.S. climate regions defined by the National Center for Environmental Information (Karl and Koss, 1984). The nine U.S. climate regions represent climatically consistent states across CONUS, and were selected for this study in an effort to group together areas that are prone to missing data due to snow and ice events during the winter months (**Figure 1**).

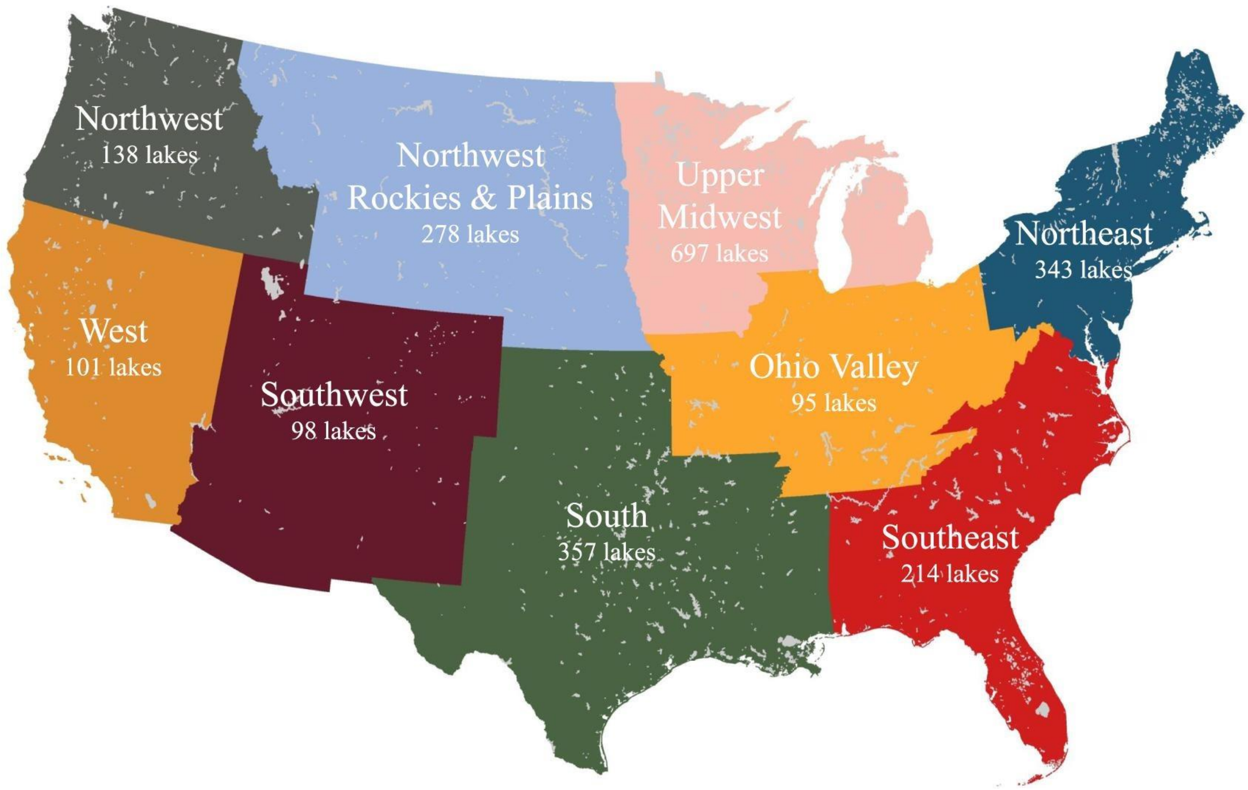

Figure 1. CONUS was divided into nine climatically consistent regions (Karl and Koss, 1984) to consider the percentage of lakes experiencing a cyanobacterial bloom at a regional level. Each color indicates the states included in each climate region and gray polygons indicate all lakes considered in the analysis. The number of resolvable lakes in each region is noted under each region name. The Ohio Valley has the fewest number of resolvable lakes with 95, while the Upper Midwest has the largest number of resolvable lakes with 697.

2.3. Analyzing cyanobacterial bloom percentage

For each weekly composite, each lake was classified according to the satellite derived cyanobacteria count: either the lake was experiencing a bloom, the lake was not experiencing a bloom, or the lake did not have sufficient data for the given weekly composite. A lake was considered to not be experiencing a bloom for the given weekly composite if the given threshold was not met, but there was at least one observable pixel in the lake (i.e. all pixels within the lake were not discarded). A lake was considered to have insufficient data for the given weekly composite if all pixels within the lake were discarded. For each week across the six years of data, percentages were calculated with a constant denominator of 2321, the total number of resolvable lakes. A constant denominator was chosen for all figures except for **Figure 2**. A dynamic denominator would imply resolvable lakes are representative of all lakes across the country or region; however, it is not reasonable to assume resolvable lakes in southern latitude states such as Florida or Texas are representative of lakes in northern latitude states such as Minnesota or Washington. This is particularly important during the winter months when snow and ice cover much of the northern part of the country. While a constant denominator was used in this study, a dynamic denominator might be appropriate on a regional scale in future studies.

2.4. Defining a cyanobacterial bloom based on spatial bloom area

In this study, four different area thresholds were tested, with any pixels above the minimum detection limit counting toward bloom area. The minimum detection limit for cyanobacteria is currently estimated to be at or above a CI value of 1. For reference, this corresponds to the World Health Organization (WHO) low-risk threshold at which there is a relatively low probability of adverse health effects in recreational waters (World Health Organization, 2003). Given the localized characterization at which an algal bloom becomes harmful, this study reports solely on the presence of cyanobacteria and not whether the observed blooms had a negative impact on human or environmental health.

The most sensitive area threshold used in this study requires that at least one pixel in the waterbody be above the detection limit for the entire lake to be classified as experiencing a bloom. Thresholds on the percentage of pixels indicating a bloom rather than the number of pixels indicating a bloom were also tested. Thresholds of 10%, 20%, and 30% were used; if the percentage of pixels indicating a bloom out of all valid pixels was at or above the given threshold, the lake was classified as experiencing a bloom.

Currently, there is no consensus regarding the minimum spatial area a bloom must cover for a waterbody to be characterized as experiencing a bloom; However, several recent studies have defined the onset of a bloom or quantified the duration of a bloom using satellite remote sensing. These studies required that some portion of a waterbody be classified as a bloom before classifying the entire waterbody as a bloom. The most sensitive threshold found in the literature defined the onset of cyanobacteria as the earliest date on which cyanobacteria was first recorded by remote sensing (Zhang et al., 2012). This classification method is similar to using a single point sample to indicate a bloom is present. Thresholds on percent of lake surface area have also been used (Davis et al., 2019; Hu et al., 2010b; Qin et al., 2015).

Herein we outlined a method to calculate weekly bloom percentage; therefore, while four discrete area thresholds were tested, the threshold used can be adjusted to meet the needs of a particular system or study. To understand if some thresholds might be more appropriate for a specific analysis, the effects of both seasonality and lake size were analyzed using 2018 data. To quantitatively compare results across seasons and lake sizes, the mean absolute deviation (MAD) was calculated by comparing bloom percentage for each subset to bloom percentage for all lakes. This allows for an investigation into whether a certain threshold under- or overclassifies bloom percentage when compared to all waterbodies. MAD is calculated similarly to Mean Absolute Error. For each subset of data (i.e. either seasons or lake sizes), the sum of the deviation between observations within each subset and the total population is divided by the number of observations within each subset. Higher values indicate less agreement with the total population.

To evaluate the effect of seasonality on each threshold, a time series was generated to display the difference in bloom percentage between each threshold on a weekly basis. This time series was then normalized to the number of lakes with valid data for each week. In other words, for a given week, the difference in bloom percentage using a 1 pixel threshold and bloom percentage using a 10% area threshold was normalized by the number of valid lakes for that weekly composite. This was repeated to compare bloom percentage between 10% and 20% and between 20% and 30%. This allows for an investigation into whether the spread between thresholds is affected by time of year. When quantifying MAD for seasonality, meteorological seasons were considered with winter as December through February, spring as March through May, summer as June through August, and fall as September through November.

To evaluate the effect of lake size on each threshold, lakes were divided into small, medium, and large lakes. Small lakes were those with fewer than 11 pixels. This cutoff was chosen since this is the smallest number at which if a lake meets the most sensitive threshold (1 pixel), then it automatically meets at least one other threshold. For example, if a lake has 7 pixels and 1 pixel indicates a cyanobacterial bloom, then this lake meets both the 1 pixel and the 10% area thresholds. However, if a lake has 11 pixels and 1 pixel indicates a cyanobacterial bloom, then this lake only meets the 1 pixel threshold. Medium lakes were classified as those with less than 50 pixels, which was chosen to keep the sample size of the three categories similar. All analyses were conducted in R Version 3.4.0 (R Core Team, 2017).

3. Results and discussion

3.1. National cyanobacterial bloom percentage

Based on the four spatial area thresholds considered in this study, a threshold of 10% was shown to reduce variability in the results, which will be further discussed in Section 3.3. Therefore, both national and regional results will be shown based on this threshold. The national pattern of bloom percentage was fairly consistent across the six years of data. **Figure 2** shows two time series representing results at the CONUS scale based on a 10% threshold. The lefthand figure shows a stacked (cumulative) time series indicating the percentage of lakes experiencing a bloom and the percentage of lakes not experiencing a bloom, as a portion of the total 2,321 lakes investigated. Results based on thresholds of 1 pixel, 20%, and 30% are shown in Fig. 9. The righthand figure shows a subset of the year, May through October, which represents the months in which the majority of the country had fairly complete spatial coverage due to reduced snow and ice extent. This time series shows just bloom percentage (i.e. the percentage of lakes without a bloom is not displayed). Bloom percentage displayed here was calculated by dividing the number of lakes experiencing a bloom by the number of observable lakes for a given week (a dynamic denominator), as opposed to the aforementioned method of dividing by the total number of lakes (a static denominator). Including this time series along with the full annual time series highlights the increase in cyanobacterial abundance seen throughout the growing season.

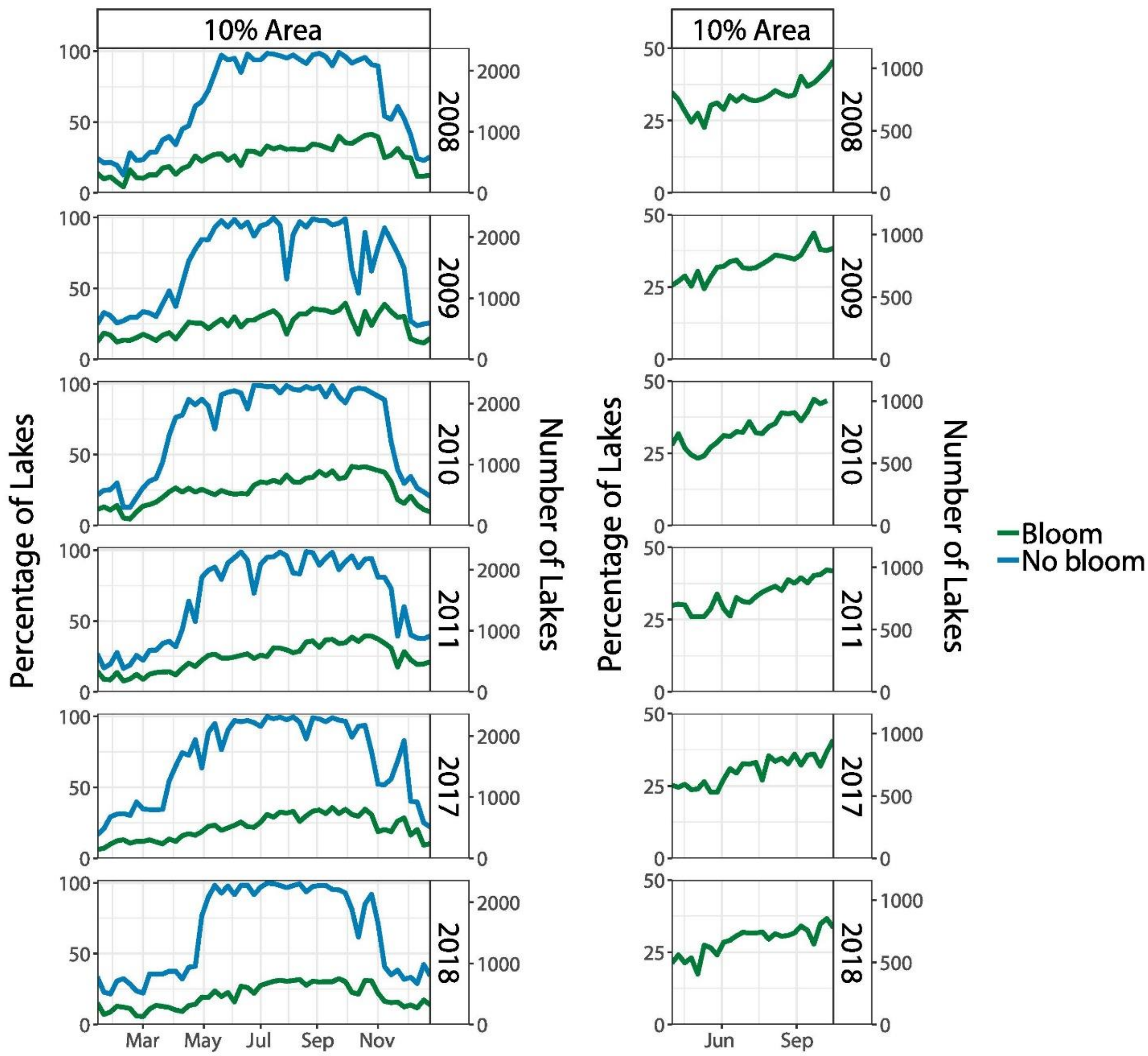

Figure 2. Time series indicating the national percentage (left axis) and number (right axis) of lakes experiencing a cyanobacterial bloom on a weekly basis for the years 2008 through 2011, 2017 and 2018 based on a spatial area threshold of 10%. The lefthand figure shows a stacked (cumulative) time series indicating lakes experiencing a bloom in green and not experiencing a bloom in blue. The righthand figure shows a time series of just the months of May through October during which snow and ice extent are limited, increasing the number of observable lakes. The righthand figure also uses a dynamic denominator in which the denominator reflects the number of observable lakes each week rather than a constant denominator of 2,321.

The minimum bloom percentage across the six years of data ranged from 6% to 15% per year, while the maximum ranged from 63% to 73%. The lowest minimum and lowest maximum both occurred in 2018, while the highest minimum and highest maximum both occurred in 2009. The percentage of lakes with no bloom reached a maximum early in the season and with relative consistency from year to year, ranging from 59% in 2009 to 66% in 2011 and occurring almost always in early July.

While summer and fall have fairly comprehensive temporal coverage, large gaps in observable data persist throughout the winter. Approximately 70% of lakes had no valid data from December through mid-March. A sharp increase in data availability typically occurred in March to April, corresponding to decreased snow and ice cover in northern latitude states. Data availability sharply declined again in November and December. There were a few instances in the summer when data availability momentarily declined which can be attributed to widespread cloud cover resulting in large data gaps across CONUS.

At the CONUS scale, the shapes of seasonal periodicity were as expected, with initiation of blooms around April, a maximum between September and November, and senescence of cyanobacteria occurring in November and December. Qualitatively, this offers some support that the satellite data agrees with previously published ecological studies describing the phenology of cyanobacteria in inland lakes. Most studies to date have been limited to either a smaller spatial or temporal subset, such as a single waterbody or a single season. Of the few year-round datasets that do exist, most report cyanobacterial bloom occurrence is highest during late-summer with minimum occurrence during winter months. Using chlorophyll a as a proxy for cyanobacteria, Lake Taihu, China indicated maximum levels from 1992–2012 in late summer and early fall with lower values observed in winter and spring (Xu et al., 2017). Using data collected from 2001–2016 in the Cheney Reservoir Watershed in Kansas, Graham et al. (2017) found cyanobacterial abundances to reach a maximum in late summer and early fall. At several sites along the Sodus Bay in Lake Ontario, the highest concentrations of cyanobacteria pigment occurred toward the end of the summer in 2011 and 2012 (Lugliè et al., 2017).

3.2. Regional cyanobacterial bloom percentage

To account for states more prone to snow and ice cover during winter, a regional bloom percentage assessment was performed where states with similar climates were grouped together. A stacked time series was generated for the percentage of lakes with a bloom and the percentage of lakes without a bloom for each of the nine climate regions based on a threshold of 10% (**Figure 3**, **Figure A1**).

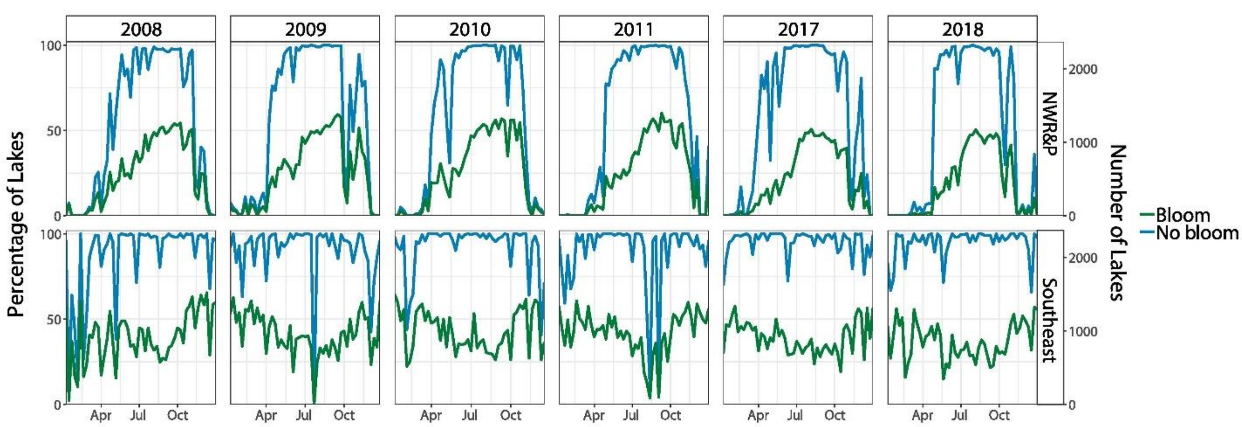

Figure 3. Stacked time series indicating regional percentage (left axis) and number (right axis) of lakes experiencing a bloom in green and not experiencing a bloom in blue for the years 2008 to 2011, 2017, and 2018. Results are shown for the Northwest Rockies & Plains (NWR&P) and the Southeast based on a spatial area threshold of 10%.

Regardless of notable differences in the timing and duration, every region reached a maximum bloom percentage of approximately 75%. Northern regions such as the Ohio Valley and Northwest Rockies and Plains reached this maximum only briefly, while the Southeast and the West had several weeks throughout the year in which at least 75% of lakes contained cyanobacteria. Bloom percentage in the South and the Southeast was persistently high with only a few weeks dropping below the 50% line across the entire time series.

Despite differences in cyanobacterial bloom percentage across each climate region, there is fairly strong temporal agreement within each climate region. With only a few exceptions, the timing of maximums and minimums as well as their relative magnitude is fairly consistent from year-to-year in each climate region, suggesting temporal stability across the years of data.

The Northwest Rockies and Plains and the Southeast were selected for **Figure 3** since each illustrates a distinct seasonal pattern. Results from the Northwest Rockies and Plains highlight difficulties in collecting year-round data in colder regions. During the winter months, the percentage of lakes with valid data was at or near 0%, indicating that we cannot fully evaluate annual time series in this region. During snow- and ice-free months, results were consistent with those observed across CONUS.

Unlike the higher latitude regions of the United States, the Southeast has a nearly complete annual time series. There were only a few notable missing data peaks in the summertime due to widespread cloud cover as confirmed with aerial imagery in both June 2009 and June 2011. Given the near-continuous time series in the Southeast, a unique pattern was observed compared to the other eight climate regions: the maximum bloom percentage actually occurred in the winter as opposed to summer. The percentage of lakes experiencing a bloom hovered at nearly 90% at the beginning of the year before gradually decreasing, reaching a minimum in late summer, and increasing again through the end of the year. The percentage of lakes without a bloom reached its highest value in late summer before decreasing through the winter. To a lesser degree, the South also showed this pattern. This finding will be further discussed in Section 3.4.

3.3. The effect of threshold choice on bloom percentage

When comparing national cyanobacterial occurrence across different thresholds, there are noticeable shifts in the magnitude of lakes with a bloom, but the overall pattern remains consistent (**Figure A2**). Bloom percentage between the four thresholds is nearly identical during the winter months when observable data is at a minimum. Results begin to separate during the spring, but differences between each threshold remain approximately stable throughout the growing season. Their deviation begins to close again during the fall and into the winter.

While all thresholds displayed the same pattern of cyanobacterial blooms throughout the year, the reported number of lakes experiencing cyanobacterial blooms at the regional and national scale can differ drastically between the most sensitive (a minimum of 1 pixel) and least sensitive (a minimum of 30% surface area) thresholds. We believe the choice of threshold should be up to those making management decisions; however, we aimed to explore how seasonality or lake size might affect bloom percentage under different threshold requirements.

To consider the effect of seasonality, we used weekly data from 2018 and compared the normalized and non-normalized differences in bloom percentage between each of the four thresholds (**Figure 4**). The difference between bloom percentage based on a 1 pixel threshold and a 10% surface area threshold was highly variable over time. When normalized by the number of observable lakes per week, the difference between 10% and 20% and the difference between 20% and 30% was relatively consistent throughout the year, indicating that the time of year does not cause large deviations in observed bloom percentage using these thresholds. This result suggests the 1 pixel threshold might produce more sporadic bloom percentage results than a threshold based on spatial coverage. MAD was calculated to compare bloom percentage for each season to annual bloom percentage (**Table 1**). Within each threshold, MAD was fairly consistent across seasons, but, of the four thresholds considered, a 1 pixel threshold had the highest MAD.

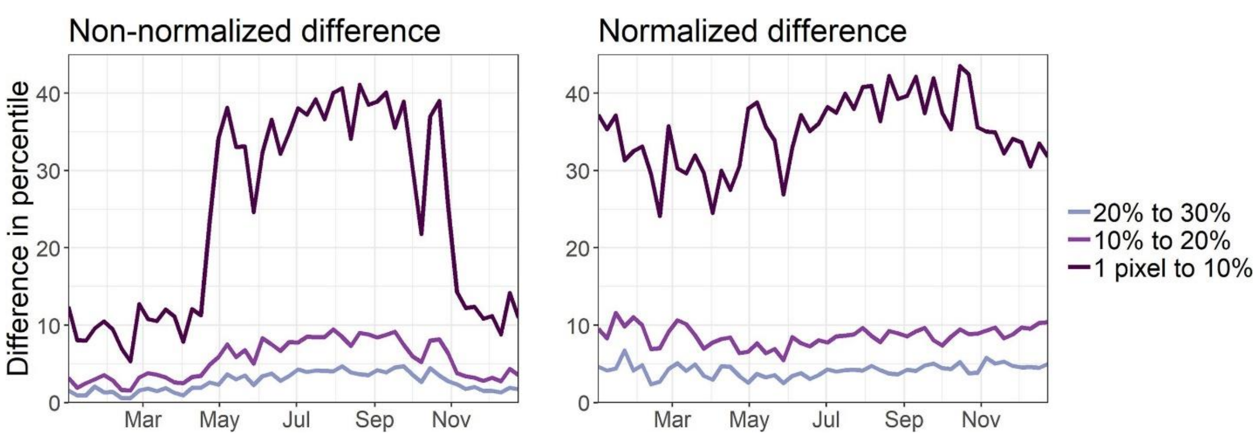

Figure 4. The difference in bloom percentage for 2018 between each of the four thresholds, both non-normalized (left) and normalized by the number of observable lakes for each week (right).

Table 1. Mean absolute deviation (MAD) comparing bloom percentage for each season to annual bloom percentage for each of the four spatial area thresholds (1 pixel, 10%, 20%, and 30%). Spring, summer, fall, and winter were defined by meteorological seasons. A larger MAD indicates increased variability for a particular season compared to all seasons.

	Season				
Threshold	**Spring**	**Summer**	**Fall**	**Winter**	**Total**
1 Pixel	22.54	25.21	22.80	23.30	93.84
10% Area	19.58	23.26	21.04	20.05	83.93
20% Area	17.47	21.37	19.25	17.79	75.89
30% Area	15.11	19.12	17.44	15.47	67.14

We also tested whether different sized lakes were under- or overclassified at each threshold. Lakes were categorized into small, medium, and large lakes based on the number of potential satellite pixels contained within the lake (**Figure 5**). At the 1 pixel threshold, large lakes tend to be overclassified and small lakes tend to be underclassified relative to all lakes. Large lakes are likely overclassified due to the extreme sensitivity of the 1 pixel threshold relative to others. This also makes the 1 pixel threshold more susceptible to false positive bloom classifications based on rare erroneous pixels. At 10%, there is very little variation indicating lake size does not seem to cause deviation at this threshold. At the 20% and 30% surface area thresholds, large lakes tend to be underclassified, although only slightly. This is likely because a much larger bloom would be required for these lakes to indicate that a bloom is present. MAD confirmed these findings with a much larger value found for the 1 pixel threshold compared to all lakes. A 30% threshold had the lowest MAD across all lake sizes, although results for 10%, 20%, and 30% were similar (**Table 2**). Based on the analyses of seasonality and lake size, it seems that a threshold on spatial area, rather than just a single pixel, is most appropriate to avoid potentially erroneous bloom percentage results.

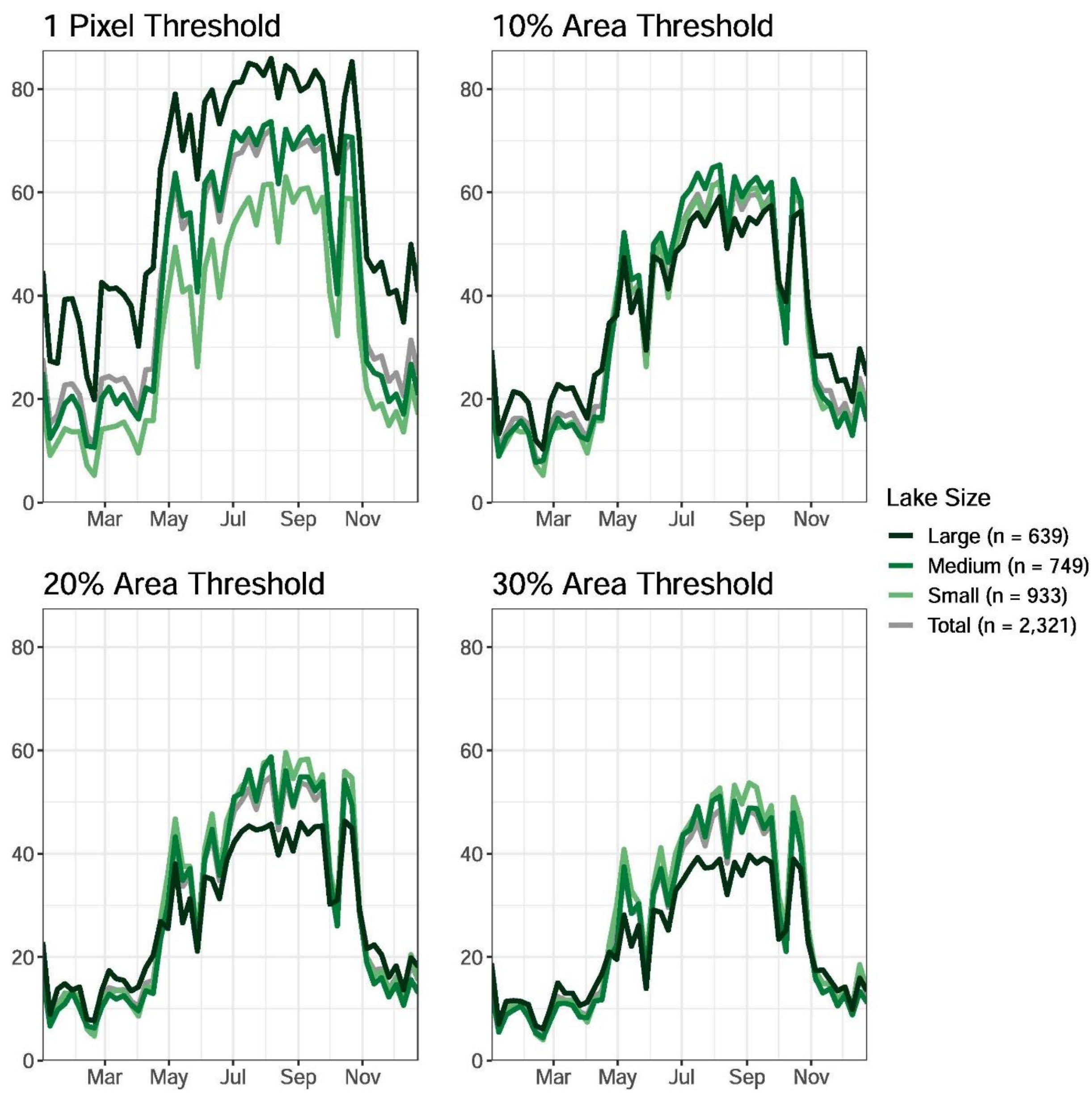

Figure 5. Bloom percentage for 2018 for each spatial area threshold (1 pixel, 10%, 20%, and 30%) and for different lake sizes. Lakes were divided into small, medium, and large lakes based on the number of valid pixels within the waterbody.

Table 2. Mean absolute deviation (MAD) comparing bloom percentage for each lake size to all lakes for each of the four spatial area thresholds (1 pixel, 10%, 20%, and 30%). Small lakes were those with less than 11 pixels, medium lakes were those with less than 50 pixels, and large lakes were those with 50 or more pixels. A larger MAD indicates increased variability for a given lake size compared to all lakes.

	Lake Size			
Threshold	**Small**	**Medium**	**Large**	**Total**
1 Pixel	10.16	2.35	15.83	28.34
10% Area	1.56	2.17	3.88	7.61
20% Area	1.91	1.52	4.07	7.50
30% Area	2.09	1.248	3.73	7.05

3.4. A case study at Lake Jesup in Florida

Regional bloom percentage was consistent with results at the CONUS scale, indicating agreement with previously published ecological patterns for all regions except the Southeast and South. These regions showed a pattern contrary to what was expected in which bloom percentage reached a maximum in the winter months, with the effect in the Southeast being more prominent than the South. To investigate the observed anomaly at a finer spatial scale, we tested our approach on Lake Jesup in Florida using monthly averages of weekly maximum CI values for each pixel in a given month (**Figure 6**). In 2018, Lake Jesup began the year with relatively low levels of cyanobacteria, but an extensive bloom began in February and persisted until June with the highest cyanobacterial values occurring in the month of March. This bloom dissipated when we would typically expect to see maximum cyanobacterial occurrence (in July through September), with the lowest values occurring in August. Another bloom began in October lasting through the end of the year. A detailed investigation of several lakes across the Southeast region revealed that this pattern is not unique to Lake Jesup.

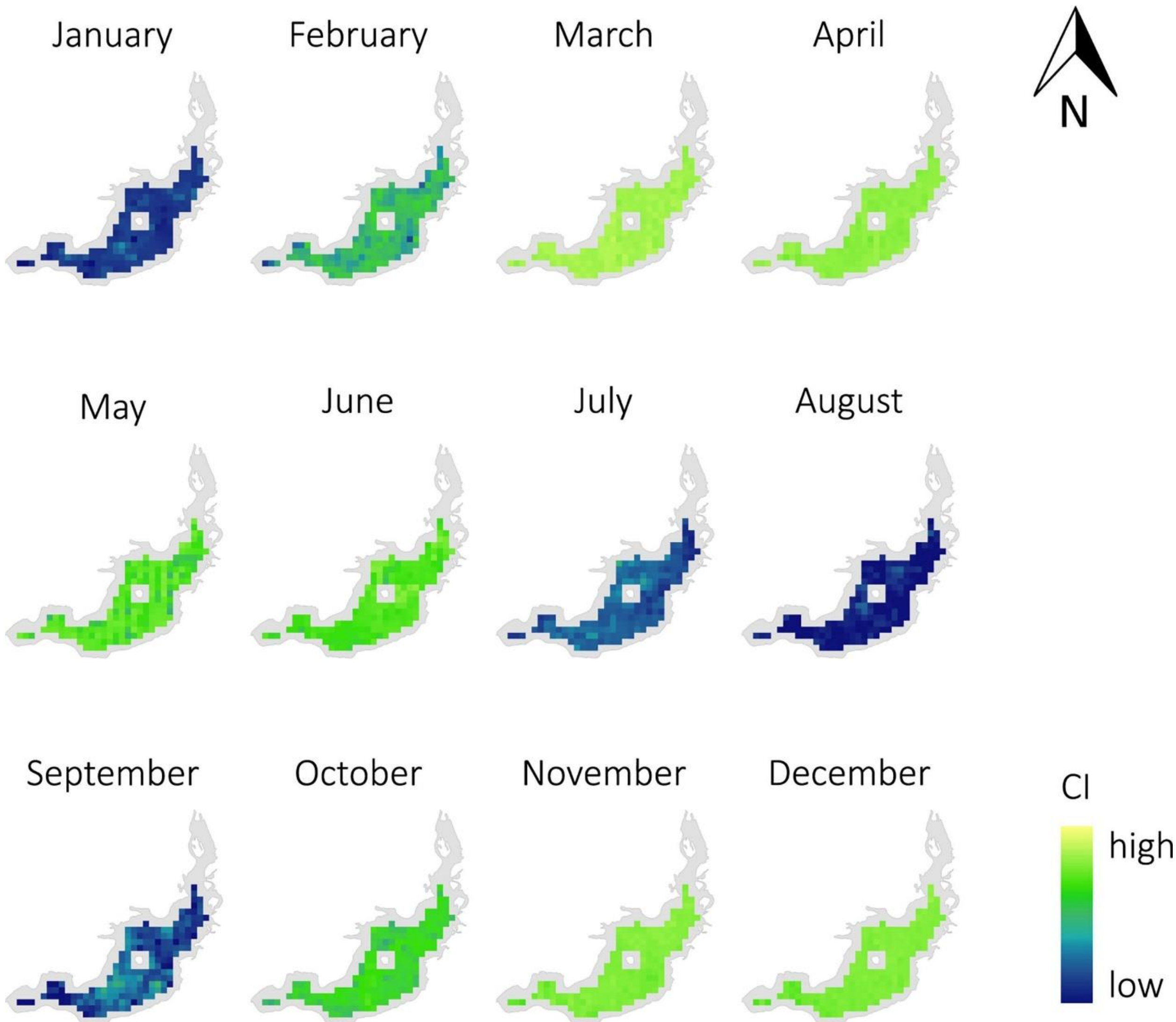

Figure 6. 2018 monthly composite CI values for Lake Jesup in Florida (28.7302°N, 81.2023°W) computed as the average of the weekly maximum CI values for each pixel in a given month. The data for Lake Jesup shows an anomalous pattern where CI reaches its highest values in the spring and winter months rather than the summer months.

To verify the phenology suggested by satellite data, monthly field observations of chlorophyll a were obtained for three sites in Lake Jesup during the months of February through November (**Figure 7**). Satellite observations were converted from CI to chlorophyll a estimates using a conversion from Tomlinson et al. (2016) which established a relationship between the two parameters using data from inland waterbodies across the state of Florida. Although there is a slight offset in the data, with satellite data consistently indicating lower values than field data, the observed patterns are well-supported between the two datasets. Low values of chlorophyll a are observed in February followed by a strong increase that reaches a maximum in spring. The lowest values occur in July and August, depending on the site, before increasing again throughout the fall and early winter. This supports the phenology observed through satellite data in this system, suggesting the bloom season may not be as well-understood as previously thought, particularly in subtropical climates where there is little seasonality.

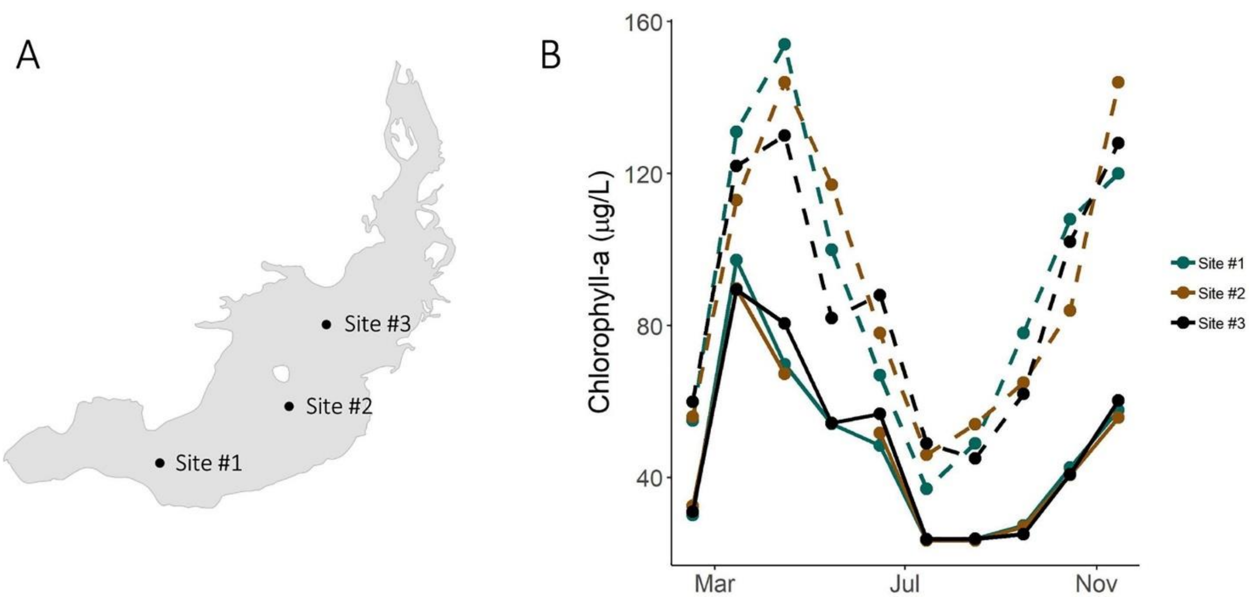

Figure 7. (A) Location of monthly chlorophyll a measurements used to validate monthly satellite imagery at Lake Jesup in Florida. (B) Monthly match-ups for field observations (dashed lines) and satellite observations (solid lines) of chlorophyll a at three point locations in Lake Jesup.

3.5. Exploring cold-season blooms across the Southeast

Although most studies are focused on the growing season, cold-weather cyanobacterial blooms have been noted throughout the literature. Cyanobacteria have been documented under ice

(Bertilsson et al., 2013), in high-latitude freshwater systems (Vincent and Quesada, 2012), and in Antarctic, Arctic, and alpine systems (Zakhia et al., 2008). Binding et al. (2012) used satellite remote sensing to observe winter blooms in Lake Erie in February 2011. Over an 11-year period from 1999–2010, Babanazarova et al. (2013) found cyanobacterial blooms throughout the winter months in Lake Nero in Western Russia. In January 2017, a winter cyanobacterial bloom was studied at a lake in Western Poland (Wejnerowski et al., 2018).

The occurrence of winter blooms in the southeast could be explained by either environmental conditions or artifacts in the satellite data. While several studies have found a minimum temperature threshold below which cyanobacterial growth is inhibited (Carey et al., 2012; Reynolds, 2006), little research has been done to investigate if a maximum temperature threshold exists. Paerl (2014) found that cyanobacteria growth diminished once reaching a water temperature of about 35 °C. It is possible that water temperatures in some lakes in the Southeast region are too warm during the summer for optimal cyanobacterial growth meaning their biomass peaks in colder months when water temperatures are lower.

Another possible explanation is the timing of the summer rainy season in Florida. The large influx of freshwater from rain events and tropical systems could dilute the water in these lakes, resulting in lower detectable levels of cyanobacteria. Berger et al. (2008) found that dilution of a cyanobacterial bloom can be used as a mitigation technique. Additionally, increased precipitation leads to less water stratification; well-mixed environments may lead to underrepresentation of cyanobacteria as the bloom is distributed throughout the water column (Reynolds, 2006), and the satellite cannot always detect blooms that are deeper in the water column.

Additionally, light availability has been found to affect the buoyancy of cyanobacteria, as these cells prefer conditions without excessive amounts of direct sunlight (Mur et al., 1999). Cyanobacteria can adjust their buoyancy (Reynolds et al., 1987), and it may be possible that under direct summer sunlight, they move lower in the water column and are not as readily detected by the sensor, leading to a reduced CI. Perhaps the increased direct solar radiation in southern latitude states during the summer months, likely in combination with warmer water temperatures, is causing cyanobacteria to shift toward more optimal conditions lower in the water column.

Field observations at Lake Jesup are an indicator that the satellite data, in at least one case, seems to be accurately reflecting in situ conditions. However, there are still several limitations that could create an artifact in the data in other waterbodies, leading us to believe that winter bloom events are more prevalent than they actually are. Of the 2,321 NHD lakes considered in this study, 297 of them are controlled by at least one dam (U.S. Army Corps of Engineers, 2016). Fluctuating water levels in these lakes could expose more pixels along the edge of the lake, or, particularly in optically shallow water, could cause bottom reflectance or benthic ecosystems to be misinterpreted as cyanobacteria.

3.6. Limitations

While this study offers a unique analysis that includes weekly observations of large inland waterbodies across CONUS, there are several limitations that should be acknowledged. Only waterbodies of sufficient size and shape were considered in order to accommodate the spatial resolution of the satellite data. As explained in Section 2.2, pixels along the land–water interface were removed which prevents consideration of the shoreline where blooms often occur. Finer resolution sensors such as those on Landsat-8 or Sentinel-2 could potentially provide more complete data across additional waterbodies in the future. Moreover, regions affected by snow and ice in the winter cannot provide year-round datasets. Thus, the observed patterns discussed here could change if a more continuous dataset were available. The snow and ice mask used here is likely more conservative than is needed; however, it is the best approach available at this time to avoid artificial winter peaks caused by signal contamination. Another satellite limitation is the inability of the sensor to detect lower portions of the water column, particularly in high attenuation waters. Cyanobacteria in well-mixed systems could appear to be less concentrated than cyanobacteria that has become stratified at the top of the water column.

4 Conclusions

This study provides a validation of algorithm performance through comparing annual changes with previously established ecological patterns on cyanobacteria population dynamics. Here, we also demonstrate a metric to quantify the percentage of lakes experiencing cyanobacterial blooms for each week from 2008–2011, 2017, and 2018. Using satellite data, we presented results for the percentage of lakes with a bloom and the percentage of lakes without a bloom for each weekly composite at both a national and regional level. Our analysis focused on relatively large lakes across the United States. At this time, there is no evidence that these findings can be extrapolated to smaller lakes, although finer spatial resolution data would offer insight into this limitation. The CONUS bloom season exhibited phenology that is well-supported in the literature, with cyanobacterial blooms increasing gradually throughout the growing season before reaching a maximum in late-summer or early-autumn. Wintertime data was persistently limited due to snow and ice cover, particularly in northern latitude regions. Contrary to the pattern seen at the CONUS scale, the percentage of lakes experiencing a bloom in the Southeast reached its highest values during winter. A small case study on Lake Jesup in Florida illustrated this phenomenon on a monthly timescale, and field data validated these findings for chlorophyll a. Several possible explanations were addressed, including environmental conditions and satellite artifacts, but further research is needed.

Results presented throughout the manuscript were largely based on a spatial area threshold of 10% for a waterbody to be classified as experiencing a bloom. A threshold of 1 pixel was found to potentially be more prone to error when analyzing both seasonal differences and the effect of lake size. Therefore, a threshold based on spatial coverage of a bloom is suggested, although of the three percentages considered, all appeared to perform fairly equally. Methods presented in this study can be used to monitor annual patterns of cyanobacterial presence in inland lakes across CONUS. Additionally, as finer spatial resolution data become available, this study can be expanded to include waterbodies not considered in this study due to spatial resolution limitations.

The primary objective of this study was to develop a methodology for monitoring inland cyanobacterial blooms across the United States on a weekly basis. Several studies have summarized large-scale drivers of cyanobacteria. Eutrophication is commonly cited as a primary driver of cyanobacterial blooms (Huisman et al., 2018; Paerl et al., 2011; Pick, 2016). A review article by Huisman et al. (2018) also credited increases in cyanobacterial occurrence to rising CO_2 concentrations and global warming. In addition to eutrophication and climate change, Pick (2016) also identified food web alterations as a compounding factor contributing to a rise in algal blooms across Canada. Although outside the scope of this study, future research should focus on drivers of these cyanobacterial blooms, particularly on a regional basis to better understand the phenology presented here.

REFERENCES

Babanazarova, O., Sidelev, S., Schischeleva, S., 2013. The structure of winter phytoplankton in Lake Nero, Russia, a hypertrophic lake dominated by Planktothrix-like Cyanobacteria. Aquatic Biosyst. 9, 18 http://aquaticbiosystems.biomedcentral.com/ articles/10.1186/2046-9063-9-18, 10.1186/2046-9063-9-18.

Berger, P., Brooks, J., Evens, T., Gobler, C., Graham, J., Berger, P., Brooks, J., Evens, T., Graham, J., Hyde, J., Karner, D.O., Shea, D., Paul, K., Paerl, V., Piehler, H., Rosen, M., Santelmann, B., Tester, M., Westrick, P., Cyanobacterial, J., 2008. Cyanobacterial Harmful Algal Blooms: Chapter 9: Causes, Prevention, and Mitigation Workgroup Report http://digitalcommons.unl.edu/usepapapers/33.

Bertilsson, S., Burgin, A., Carey, C.C., Fey, S.B., Grossart, H.P., Grubisic, L.M., Jones, I.D., Kirillin, G., Lennon, J.T., Shade, A., Smyth, R.L., 2013. The under-ice microbiome of seasonally frozen lakes. Limnol. Oceanogr. 58. https://doi.org/10.4319/lo.2013.58.6.1998.

Binding, C.E., Greenberg, T.A., Bukata, R.P., Smith, D.E., Twiss, M.R., 2012. The MERIS MCI and its potential for satellite detection of winter diatom blooms on partially ice covered Lake Erie. J. Plankton Res. 34, 569–573. https://doi.org/10.1093/plankt/ fbs021.

Carey, C.C., Ibelings, B.W., Hoffmann, E.P., Hamilton, D.P., Brookes, J.D., 2012. Ecophysiological adaptations that favour freshwater cyanobacteria in a changing climate. Water Res. 46, 1394–1407. https://doi.org/10.1016/J.WATRES.2011.12.016.

Chorus, I., Falconer, I.R., Salas, H.J., Bartram, J., 2000. Health risks caused by freshwater Cyanobacteria in recreational waters. J. Toxicol. Environ. Health, Part B 3, 323–347. https://doi.org/10.1080/109374000436364.

Clark, J.M., Schaeffer, B.A., Darling, J.A., Urquhart, E.A., Johnston, J.M., Ignatius, A.R., Myer, M.H., Loftin, K.A., Werdell, P.J., Stumpf, R.P., 2017. Satellite monitoring of cyanobacterial harmful algal bloom frequency in recreational waters and drinking water sources. Ecol. Ind. 80, 84–95. https://doi.org/10.1016/j.ecolind.2017.04.046.

Davis, T.W., Stumpf, R., Bullerjahn, G.S., McKay, R.M.L., Chaffin, J.D., Bridgeman, T.B., Winslow, C., 2019. Science meets policy: a framework for determining impairment designation criteria for large waterbodies affected by cyanobacterial harmful algal blooms. Harmful Algae 81, 59–64. https://doi.org/10.1016/J.HAL.2018.11.016.

Graham, J.L., Foster, G.M., Kramer, A.R., Survey, U.S.G., 2017. Twenty years of water quality studies in the Cheney Reservoir Watershed, Kansas, 1996-2016. Technical Report. Reston, VA.https://doi.org/10.3133/fs20173019.http://pubs.er.usgs.gov/ publication/fs20173019.

Hu, C., Lee, Z., Ma, R., Yu, K., Li, D., Shang, S., 2010. Moderate Resolution Imaging Spectroradiometer (MODIS) observations of cyanobacteria blooms in Taihu Lake, China. J. Geophys. Res.: Oceans 115. https://doi.org/10.1029/2009JC005511.

Hudnell, H.K., Dortch, Q., Zenick, H., 2008. An Overview of the Interagency, International Symposium on Cyanobacterial Harmful Algal Blooms (ISOC-HAB): Advancing the Scientific Understanding of Freshwater Harmful Algal Blooms. In: Hudnell, H.K. (Ed.), Springer New York, New York, NY, pp. 1–16 URL: https:// doi.org/10.1007/978-0-387-75865-7_1, 10.1007/978-0-387-75865-7_1.

Huisman, J., Codd, G.A., Paerl, H.W., Ibelings, B.W., Verspagen, J.M.H., Visser, P.M., 2018. Cyanobacterial blooms. Nat. Rev. Microbiol. 16, 471–483. https://doi.org/10. 1038/s41579-018-0040-1.

Karl, T., Koss, W.J., 1984. Regional and National Monthly, Seasonal, and Annual Temperature Weighted by Area, 1895–1983.

Kutser, T., 2009. Passive optical remote sensing of cyanobacteria and other intense phytoplankton blooms in coastal and inland waters. Int. J. Remote Sens. 30, 4401–4425. https://doi.org/10.1080/01431160802562305.

Loftin, K.A., Graham, J.L., Hilborn, E.D., Lehmann, S.C., Meyer, M.T., Dietze, J.E., Griffith, C.B., 2016. Cyanotoxins in inland lakes of the United States: Occurrence and potential recreational health risks in the EPA National Lakes Assessment 2007. Harmful Algae 56, pp. 77–90. doi: 10.1016/j.hal.2016.04.001.

Lugliè, A., Giacobbe, M.G., Riccardi, E., Bruno, M., Pigozzi, S., Mariani, M.A., Satta, C.T., Stacca, D., Bazzoni, A.M., Caddeo, T., Farina, P., Padedda, B.M., Pulina, S., Sechi, N., Milandri, A., 2017. Paralytic shellfish toxins and cyanotoxins in the Mediterranean: New data from Sardinia and Sicily (Italy). Microorganisms 10.3390/microorganisms5040072.

Lunetta, R.S., Schaeffer, B.A., Stumpf, R.P., Keith, D., Jacobs, S.A., Murphy, M.S., 2015. Evaluation of cyanobacteria cell count detection derived from MERIS imagery across the eastern USA. Remote Sens. Environ. 157, 24–34. https://doi.org/10.1016/j.rse. 2014.06.008.

Matthews, M.W., Bernard, S., Robertson, L., 2012. An algorithm for detecting trophic status (chlorophyll-a), cyanobacterial-dominance, surface scums and floating vegetation in inland and coastal waters. Remote Sens. Environ. 124, 637–652. https://doi.org/10.1016/j.rse.2012.05.032.

Mur, L.R., Skulberg, O.M., Utkilen, H., 1999. Cyanobacteria in the environment. In: Chorus, I., Bartram, J. (Eds.), Toxic Cyanobacteria in Water: A guide to their public health consequences, monitoring and management. E & FN Spon, London chapter 2.

Neuhaus, L., 2016. Reeking, Oozing Algae Closes South Florida Beaches.https://www.nytimes.com/2016/07/02/us/reeking-oozing-algae-closes-south-florida-beaches.html?_r=2.

Paerl, H.W., 2014. Mitigating harmful cyanobacterial blooms in a human- and climatically-impacted world. Life 4, 988–1012. https://doi.org/10.3390/life4040988.

Paerl, H.W., Hall, N.S., Calandrino, E.S., 2011. Controlling harmful cyanobacterial blooms in a world experiencing anthropogenic and climatic-induced change. Sci. Total Environ. 409, 1739–1745. https://doi.org/10.1016/j.scitotenv.2011.02.001.

Pick, F.R., 2016. Blooming algae: a Canadian perspective on the rise of toxic cyanobacteria. Can. J. Fish. Aquat. Sci. 73, 1149–1158. https://doi.org/10.1139/cjfas2015-0470.

Qin, B., Li, W., Zhu, G., Zhang, Y., Wu, T., Gao, G., 2015. Cyanobacterial bloom management through integrated monitoring and forecasting in large shallow eutrophic Lake Taihu (China). J. Hazard. Mater. 287, 356–363. https://doi.org/10.1016/j. jhazmat.2015.01.047.

R Core Team, 2017. R: A Language and Environment for. Statistical Computing. URL: http://www.R-project.org/.

Reynolds, C.S., 2006. Ecology of phytoplankton. Ecology, biodiversity, and conservation. Cambridge University Press, Cambridge. URL: https://catalog.lib.ncsu.edu/record/NCSU1912943.

Reynolds, C.S., Oliver, R.L., Walsby, A.E., 1987. Cyanobacterial dominance: the role of buoyancy regulation in dynamic lake environments. NZ J. Mar. Freshwat. Res. 21, 379–390. https://doi.org/10.1080/00288330.1987.9516234.

Schaeffer, B.A., Bailey, S.W., Conmy, R.N., Galvin, M., Ignatius, A.R., Johnston, J.M., Keith, D.J., Lunetta, R.S., Parmar, R., Stumpf, R.P., Urquhart, E.A., Werdell, P.J., Wolfe, K., 2018. Mobile device application for monitoring cyanobacteria harmful algal blooms using Sentinel-3 satellite Ocean and Land Colour Instruments. Environ. Model. Software 109, 93–103. https://doi.org/10.1016/j.envsoft.2018.08.015.

Simis, S.G.H., Peters, S.W.M., Gons, H.J., 2005. Remote sensing of the cyanobacterial pigment phycocyanin in turbid inland water. Limnol. Oceanogr. 50, 237–245. https://doi.org/10.4319/lo.2005.50.1.0237.

Smayda, T.J., 2003. What is a bloom? A commentary. Limnol. Oceanogr. 42, 1132–1136. https://doi.org/10.4319/lo.1997.42.5_part_2.1132.

Sonich-Mullin, C., 2014. EPA Science In Action: Keeping an Eye on. Harmful Algal Blooms.

Stumpf, R.P., Davis, T.W., Wynne, T.T., Graham, J.L., Loftin, K.A., Johengen, T.H., Gossiaux, D., Palladino, D., Burtner, A., 2016a. Challenges for mapping cyanotoxin patterns from remote sensing of cyanobacteria. Harmful Algae 54, 160–173. https://doi.org/10.1016/j.hal.2016.01.005.

Stumpf, R.P., Johnson, L.T., Wynne, T.T., Baker, D.B., 2016b. Forecasting annual cyanobacterial bloom biomass to inform management decisions in Lake Erie. J. Great Lakes Res. 42, 1174–1183. https://doi.org/10.1016/j.jglr.2016.08.006.

Tomlinson, M.C., Stumpf, R.P., Wynne, T.T., Dupuy, D., Burks, R., Hendrickson, J., Fulton III, R.S., 2016. Relating chlorophyll from cyanobacteria-dominated inland waters to a MERIS bloom index. Remote Sens. Lett. 7, 141–149. https://doi.org/10.1080/2150704X.2015.1117155.

Urquhart, E.A., Schaeffer, B.A., 2020. Envisat MERIS and Sentinel-3 OLCI satellite lake biophysical water quality flag dataset for the contiguous United States. Data in Brief, 104826. https://doi.org/10.1016/j.dib.2019.104826.

Urquhart, E.A., Schaeffer, B.A., Stumpf, R.P., Loftin, K.A., Werdell, P.J., 2017. A method for examining temporal changes in cyanobacterial harmful algal bloom spatial extent using satellite remote sensing. Harmful Algae 67, 144–152. https://doi.org/10.1016/J.HAL.2017.06.001.

U.S. Army Corps of Engineers, 2016. National Inventory of Dams.

Vincent, W.F., Quesada, A., 2012. Cyanobacteria in High Latitude Lakes, Rivers and Seas. In: Whitton, B.A. (Ed.), Ecology of Cyanobacteria II: Their Diversity in Space and Time. Springer, Netherlands, Dordrecht, pp. 371–385. https://doi.org/10.1007/978- 94-007-3855-3_13.

Wejnerowski, U., Rzymski, P., Kokociński, M., Meriluoto, J., 2018. The structure and toxicity of winter cyanobacterial bloom in a eutrophic lake of the temperate zone. Ecotoxicology 27, 752–760. https://doi.org/10.1007/s10646-018-1957-x.

World Health Organization, 2003. Algae and Cyanobacteria in Fresh Water, in: Guidelines for safe recreational water environments. chapter 8, pp. 136–158.

Wynne, T.T., Stumpf, R.P., Tomlinson, M.C., Fahnenstiel, G.L., Dyble, J., Schwab, D.J., Joshi, S.J., 2013. Evolution of a cyanobacterial bloom forecast system in western Lake Erie: development and initial evaluation. J. Great Lakes Res. 39, 90–99. https://doi.org/10.1016/j.jglr.2012.10.003.

Wynne, T.T., Stumpf, R.P., Tomlinson, M.C., Warner, R.A., Tester, P.A., Dyble, J., Fahnenstiel, G.L., 2008. Relating spectral shape to cyanobacterial blooms in the Laurentian Great Lakes. Int. J. Remote Sens. 29, 3665–3672. https://doi.org/10.1080/01431160802007640.

Wyoming DEQ, 2018a. Big Sandy Reservoir Harmful Cyanobacterial Investigation 2018. Technical Report. Wyoming Department of Environmental Quality. http://deq.wyoming.gov/media/attachments/Water.

Wyoming DEQ, 2018b. Eden Reservoir Harmful Cyanobacterial Investigation 2018. Technical Report. Wyoming Department of Environmental Quality. http://deq.wyoming.gov/media/attachments/Water.

Wyoming DEQ, 2018c. Pathfinder Reservoir Harmful Cyanobacterial Bloom Investigation 2018. Technical Report. Wyoming Department of Environmental Quality. http://deq.wyoming.gov/media/attachments/Water.

Xu, H., Paerl, H.W., Zhu, G., Qin, B., Hall, N.S., Zhu, M., 2017. Long-term nutrient trends and harmful cyanobacterial bloom potential in hypertrophic Lake Taihu, China. Hydrobiologia 787, 229–242. https://doi.org/10.1007/s10750-016-2967-4.

Zakhia, F., Jungblut, A.D., Taton, A., Vincent, W.F., Wilmotte, A., 2008. Cyanobacteria in Cold Ecosystems. In: Margesin, R., Schinner, F., Marx, J.C., Gerday, C. (Eds.), Psychrophiles: from Biodiversity to Biotechnology. Springer, Berlin, Heidelberg, Berlin, Heidelberg, pp. 121–135. https://doi.org/10.1007/978-3-540-74335-4_8.

Zhang, M., Duan, H., Shi, X., Yu, Y., Kong, F., 2012. Contributions of meteorology to the phenology of cyanobacterial blooms: Implications for future climate change. Water Res. 46, 442–452. https://doi.org/10.1016/j.watres.2011.11.013.

CHAPTER 3: ASSESSING CYANOBACTERIAL FREQUENCY AND ABUNDANCE AT SURFACE WATERS NEAR DRINKING WATER INTAKES ACROSS THE UNITED STATES

Prepared for submission to Water Research

Authors

Megan M. Coffer[1,2], Blake A. Schaeffer[3], Katherine Foreman[4], Alex Porteous[4], Keith A. Loftin[5], Richard P. Stumpf[6], Jeremy Werdell[7], Erin A. Urquhart[8], Ryan J. Albert[4], John A. Darling[3]

Affiliations

[1]ORISE Fellow, U.S. Environmental Protection Agency, Office of Research and Development, National Exposure Research Laboratory, USA

[2]Center for Geospatial Analytics, North Carolina State University, Raleigh, NC, USA

[3]U.S. Environmental Protection Agency, Office of Research and Development, Durham, NC, USA

[4]U.S. Environmental Protection Agency, Office of Water, Washington, DC, USA

[5]United States Geological Survey, Kansas Water Science Center, Lawrence, KS, USA

[6]National Oceanic and Atmospheric Administration, National Centers for Coastal Ocean Science, Silver Spring, MD, USA

[7]Ocean Ecology Laboratory, NASA Goddard Space Flight Center, Greenbelt, MD, USA

[8]Science Systems and Applications, Inc., Ocean Ecology Laboratory, NASA Goddard Space Flight Center, Greenbelt, MD, USA

Acknowledgements

The authors thank Michael Elovitz, Nicholas Dugan, Lesley D'Anglada, Tom Waters, Melissa Simic, and Crystal Rodgers-Jenkins for their contributions in manuscript technical review and suggestions. This work was supported by the NASA Ocean Biology and Biogeochemistry Program/Applied Sciences Program (proposal 14-SMDUNSOL14-0001 and SMDSS20-0006) and by U.S. EPA, NOAA, U.S. Geological Survey Toxic Substances Hydrology Program, and Oak Ridge Institute for Science and Technology (ORISE). This article has been reviewed by the CEMM and approved for publication. Mention of trade names or commercial products does not constitute endorsement or recommendation for use by the U.S. Government. The views expressed in this article are those of the authors and do not necessarily reflect the views or policies of the U.S. EPA.

Abstract

This study presents the first large-scale assessment of cyanobacterial frequency and abundance at surface drinking water intakes across the United States. Public water systems serve drinking water to nearly 90% of the United States population. Cyanobacteria and their toxins may degrade the quality of finished drinking water and can lead to negative health consequences. Satellite imagery can serve as a cost-effective and consistent monitoring technique for surface cyanobacterial blooms in source waters and can provide drinking water treatment operators information for managing their systems. This study uses satellite imagery from the European Space Agency's Ocean and Land Colour Instrument (OLCI) spanning June 2016 through April 2020. At 300-m spatial resolution, OLCI imagery can be used to monitor cyanobacteria in 685 drinking water sources across 285 lakes in 44 states, referred to here as resolvable drinking water sources. First, a subset of satellite data was compared to a subset of 99 responses submitted as part of the U.S. Environmental Protection Agency's fourth Unregulated Contaminant Monitoring Rule (UCMR 4). These UCMR 4 qualitative responses included visual observations of algal bloom presence and absence near drinking water intakes from March 2018 through November 2019. Overall agreement between satellite imagery and UCMR 4 qualitative responses was high at over 94% with a Kappa coefficient of 0.70. Next, temporal frequency of cyanobacterial blooms at all resolvable drinking water sources was assessed. In 2019, bloom frequency averaged 2% and peaked at 100%, where 100% indicated a bloom was always present at the source waters when satellite imagery was available. Monthly cyanobacterial abundances were used to assess short-term trends across all resolvable drinking water sources and effect size was computed to provide insight on the number of years of data that must be obtained to increase confidence in an observed change. Generally, 2016-2020 was an insufficient time period for confidently observing changes at these source waters; On average, a decade of satellite imagery would be required for observed environmental trends to outweigh variability in the data. However, five source waters did demonstrate a sustained short-term trend, with one increasing in cyanobacterial abundance from June 2016 to April 2020 and four decreasing.

Keywords Cyanobacteria, Drinking water, Source water quality, Remote sensing, Inland water, Water Quality

1 Introduction

Public water systems (PWSs) delivered over 23 billion gallons of surface water per day in 2015 for domestic water use in the United States (US), providing freshwater for services such as drinking, food preparation, bathing, and landscaping (Dieter et al., 2018). These PWSs served an estimated 283 million people in 2015, representing approximately 87% of the US population. Cyanobacterial blooms can degrade the quality drinking water sources, and some blooms can contain toxins, called cyanotoxins, which pose a human health risk when occurring at elevated levels in finished drinking water. Whether a bloom contains cyanotoxins or not, high levels of cyanobacteria in source water can necessitate that drinking water systems simultaneously address multiple treatment objectives including managing taste and odor concerns, cyanotoxin breakthrough, and disinfection byproduct (DBP) formation (U.S. EPA, 2016a).

In recent years, cyanobacterial blooms have resulted in several large-scale drinking water advisories. In September 2013, a cyanobacterial bloom along the western shore of Lake Erie resulted in nearly two thousand people being left without access to clean drinking water in the Carroll Township in Ohio (GLCR, 2013). Toledo, Ohio issued a multi-day “Do Not Drink” advisory for more than 500,000 people in 2014 because of elevated cyanotoxins found in their finished drinking water (Great Lakes Commission, 2014). In 2018, the city of Salem, Oregon was under a “Do Not Drink” advisory applying to vulnerable populations for several weeks, impacting several hundreds of thousands of people, after elevated levels of the cyanotoxins microcystins and cylindrospermopsin were found in its finished drinking water (The Novak Consulting Group, 2018).

Conventional drinking water treatment (i.e. coagulation, flocculation, filtration) has been proven effective in removing cyanobacterial cells and intracellular cyanotoxins (Szlag et al., 2015; U.S. EPA, 2016a). However, additional treatment approaches are typically necessary in the presence of extracellular toxins. Ultimately, ensuring cyanotoxins do not breakthrough to finished drinking water is dependent on the type and amount of toxins present and the treatment approaches, management, and operations drinking water treatment plants use to respond to the bloom in source waters.

PWSs will benefit from any advance knowledge regarding cyanobacterial bloom development in their source waters to prepare for, and if possible, mitigate the risks posed by blooms to finished drinking water. The implementation of early warning indicators (EWIs) has proven effective in managing cyanobacterial blooms, allowing managers to proactively make critical decisions to prevent further bloom proliferation (Pace et al., 2017; Wilkinson et al., 2018). EWIs are typically focused on measuring known drivers of cyanobacterial blooms where a certain predetermined threshold must be met before triggering the EWI.

Satellite imagery is a a cost-effective and standardized monitoring technique for cyanobacterial blooms (Coffer et al., 2020; Kahru and Elmgren, 2014; Mishra et al., 2019; Stroming et al., 2020; Stumpf et al., 2016a, 2016b; Urquhart et al., 2017), including for drinking water sources (Clark et al., 2017). While satellite imagery is typically not used to measure drivers of cyanobacterial blooms, it can provide consistent temporal coverage of cyanobacterial abundance and can serve a similar purpose as EWIs. Advanced knowledge can alert drinking water managers to blooms in their source waters, suggesting the need for cyanotoxin sampling in source and finished water. Results of that sampling could guide managers in implementing mitigation strategies in the source water itself, optimizing existing treatment approaches, or implementing additional treatment, with the goal of reducing the risk of cyanotoxins breaching the treatment system.

Motivated by concern for the impact of cyanobacterial blooms on drinking water quality, this study uses satellite imagery to assess the frequency and abundance of cyanobacteria at surface source waters for nearly 700 drinking water intakes across 44 US states. Additionally, this study investigates the potential connection at a subset of these source waters between satellite remotely sensed data and a subset of qualitative visual observations collected under the fourth Unregulated Contaminant Monitoring Rule (UCMR 4). UCMR 4 qualitative responses assessed whether an algal bloom was visible near the intake within a month of quantitative finished drinking water sampling; A subset of these responses was considered as those reported up to April 2020 and represents a portion of the data collected from March 2018 through November 2019. Satellite data were obtained from the European Space Agency's Ocean and Land Colour Instrument (OLCI) onboard the Sentinel-3A satellite from June 2016 through April 2020. The following research objectives were addressed:

1. Using a subset of observable drinking water sources, assess agreement between satellite-derived cyanobacterial abundance and qualitative visual reporting of algal bloom presence/absence collected as part of UCMR 4.
2. Using satellite imagery collected at all resolvable drinking water sources, quantify average annual frequency of cyanobacterial blooms for the year 2019.

3. Using satellite imagery collected at all resolvable drinking water sources, analyze short-term trends in cyanobacterial abundance from June 2016 through April 2020.

2 Data and methods

2.1 Satellite observations

Satellite observations were obtained from the European Space Agency's Ocean and Land Colour Instrument (OLCI) onboard the Sentinel-3A satellite, launched in February 2016. OLCI offers a revisit frequency of approximately 2-3 days and a spatial resolution of 300 m at nadir, where nadir is defined as the point on Earth's surface directly below the satellite. Data is collected in 21 spectral bands with center wavelengths ranging from 400 to 1,020 nanometers (nm). Standard OLCI Level-1B data were obtained from the NASA Ocean Biology Processing Group (https://oceandata.sci.gsfc.nasa.gov). Following Urquhart & Schaeffer (2020) criteria for satellite pixel inclusion and exclusion, satellite pixels were quality flagged and discarded if they contained cloud cover, fell along the land-water interface, were adjacent to a land pixel, or contained snow or ice. Valid satellite pixels represent those not quality flagged and discarded according to these criteria.

This study focuses on the Cyanobacterial Index product (CI-cyano) generated under the auspices of the Cyanobacterial Assessment Network (CyAN) Project (Schaeffer et al., 2015).The CI-cyano algorithm leverages spectral bands centered at 665 nm, 681 nm, and 709 nm to assess bloom biomass (Wynne et al., 2008), and those centered at 620 nm, 665 nm, and 681 nm as exclusion criterion to prevent the identification of non-cyanobacterial blooms, as reflectance at 620 nm is sensitive to phycocyanin (Lunetta et al., 2015). Coffer et al. (2020) details the evolution of the CI-cyano including the differentiation between cyanobacterial blooms and other algae defined by Matthews et al. (2012). Observations were aggregated into weekly composites preserving the maximum CI-cyano value for each pixel. Throughout this study, a bloom detected by satellite imagery is defined as any cyanobacterial abundance that exceeds the detection limit of the sensor, which is preliminarily estimated to be between 10,000 to 20,000 cells/mL.

CI-cyano has been validated quantitatively with cell counts and chlorophyll-a across 38 US states (Clark et al., 2017; Lunetta et al., 2015; Schaeffer et al., 2018) and as presence and absence (Mishra et al., 2021). Additionally, it has been successfully demonstrated for state (Clark et al., 2017; Urquhart et al., 2017) and national (Coffer et al., 2020) assessments of cyanobacterial occurrence. It has also been used by several states to issue recreational advisories; for example, the Wyoming Department of Environmental Quality issued such recreational advisories at Big Sandy Reservoir (Wyoming DEQ, 2018a), Eden Reservoir (Wyoming DEQ, 2018b), and Pathfinder Reservoir (Wyoming DEQ, 2018c). Coffer et al. (2020) demonstrated expected seasonality via CI-cyano across 46 US states.

There are 2,196 lakes and reservoirs across 46 US states that can be observed given the spatial resolution of OLCI (**Figure 1**; Urquhart and Schaeffer, 2020). Lakes and reservoirs were required to be of sufficient size and shape to accommodate at least one 300-m water-only satellite pixel after the exclusion criteria described above. These range in size from 1.3 km2 to over 4,000 km2, limiting this analysis to relatively large lakes and reservoirs across the US. Hereafter, lakes and reservoirs will be referred to exclusively as lakes, and those lakes that can be observed with 300-m satellite imagery are referred to as observable lakes.

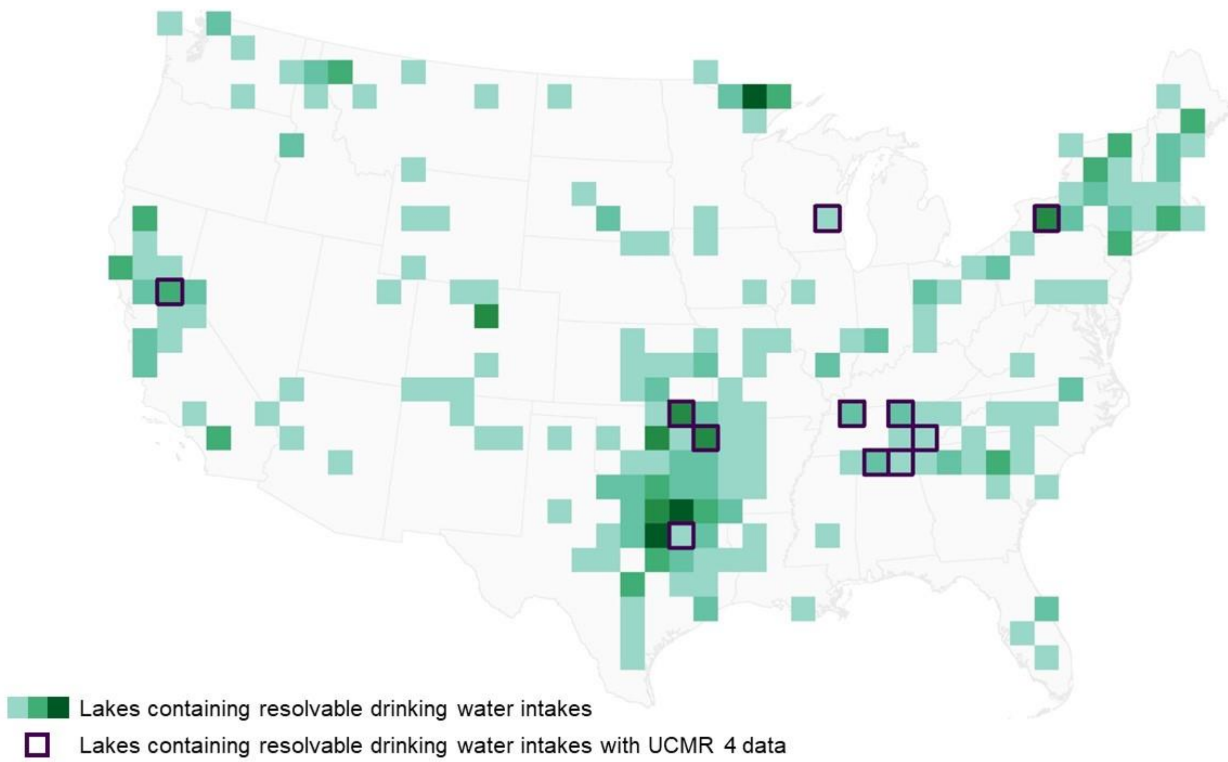

Figure 1. A total of 285 lakes across 44 states contain drinking water intakes and are observable given the spatial resolution of OLCI (300 m). Green polygons indicate the density of these lakes, where lighter green indicates a lower density of observable lakes per area and darker green indicates a higher density of observable lakes per area. Polygons with a purple border represent the 11 lakes across 6 states that also contain drinking water intakes where UCMR 4 qualitative responses were collected from March 2018 through November 2019. Lakes with drinking water intakes displayed in this figure are grouped spatially to protect the locations of the drinking water intakes.

2.2 Resolvable drinking water intake locations

Surface intake locations extracted from the Safe Drinking Water Information System (SDWIS) database were previously described in Clark et al. (2017). Locations of drinking water intakes for each PWS facility are based on information contained in the SDWIS database. SDWIS intake location information is sensitive for homeland security reasons and access to locational data was provided as part of this study. This assigned location will hereafter be referred to as the "drinking water intake location" or "drinking water intake."

These drinking water intakes were first subset to include just those within 100 m of an observable lake following Clark et al. (2017). A total of 877 drinking water intake locations were within 100 m of an observable lake. These locations were then subset to include just those within 900 m of a valid satellite pixel, a slight variation from Clark et al. (2017), selected to represent a minimum distance of three 300-m pixels in each direction. This left 685 drinking water intake locations, corresponding to 285 lakes across 44 states (**Figure 1**). These remaining 685 drinking water intakes are referred to as resolvable drinking water intakes.

Drinking water intakes that were within 100 m of an observable lake and within 900 m of a valid satellite pixel are referred to as resolvable drinking water intakes. "Drinking water sources" refer to the aggregated satellite pixels in an observable lake within the immediate vicinity of the drinking water intake location. For each of these resolvable drinking water intake locations, source waters were characterized by selecting all valid satellite pixels intersecting or falling within a 900 m buffer of the intake (**Figure 2**).

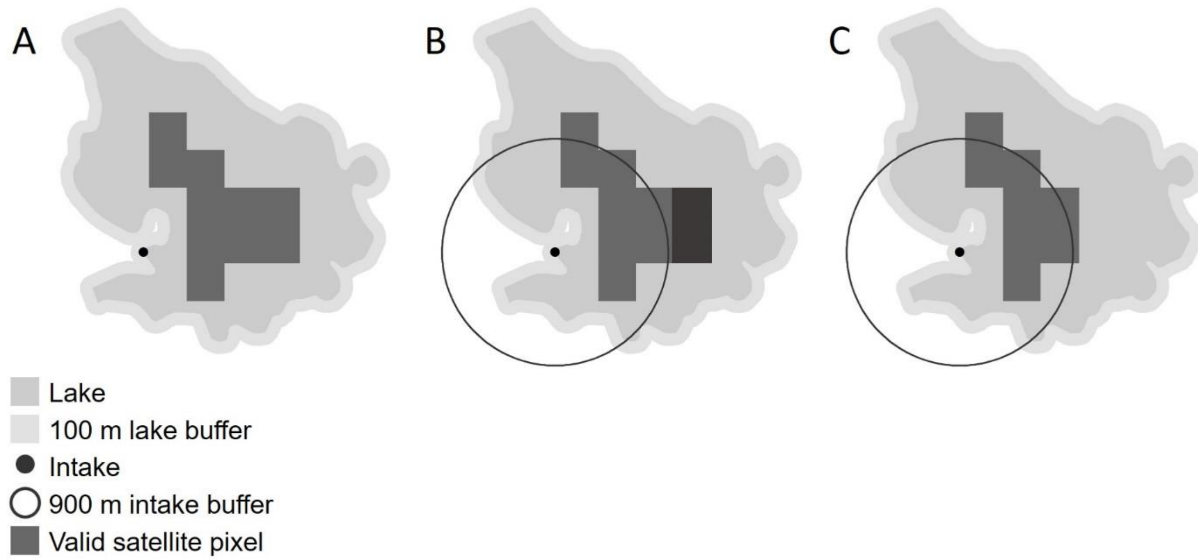

Figure 2. A conceptual diagram illustrating data extraction at each drinking water intake location. For a drinking water intake to be considered resolvable, it must first (A) fall within a 100 m buffer of the lake boundary, then it must (B) fall within 900 m of a valid satellite pixel. (C) All valid pixels that intersect or fall within a 900 m buffer of the location represent the drinking water sources and are selected for analysis.

2.3 UCMR 4 qualitative responses

The U.S. EPA collects nationally representative finished drinking water data for unregulated contaminants suspected to be present and pose a health risk in drinking water under the Unregulated Contaminant Monitoring Rule (UCMR) program (U.S. EPA, 2016b, 2016c). This monitoring is used by the U.S. EPA to understand the frequency and level of occurrence of unregulated contaminants in the nation's PWSs. As part of a Safe Drinking Water Act mandate, every five years the U.S. EPA develops a new list of UCMR contaminants.

UCMR 4 required monitoring for 30 chemicals between 2018 and 2020. This included monitoring for 10 cyanotoxins in finished water as well as qualitative data collected regarding the presence of an algal bloom and other characteristics in source waters around the same time as the quantitative sample collection. Cyanotoxin monitoring as part of UCMR 4 was required to be conducted twice a month for each PWS for four consecutive months, excluding the months of December, January, and February, and was required to be collected during one single year between 2018 and 2020. UCMR 4 cyanotoxin monitoring was required at all large public water systems (i.e. systems serving more than 10,000 customers) and a small, statistically representative subset of small systems that use surface water as their sources. A subset of UCMR 4 responses was obtained from the 2020Q1 release. Given the temporal lag between data collected by the PWS and data available for distribution, this dataset was obtained in April 2020 but only contained data from March 2018 through November 2019 and does not represent all the data collected during that timeframe.

This study is not utilizing the quantitative UCMR 4 cyanotoxin finished water data; instead it utilizes responses provided at the time of finished water monitoring in which the PWS determined if a surface algal bloom was present near the intake within a specified period of time. More specifically, UCMR 4 asked the following question: “Preceding the finished water sample collection, did you observe an algal bloom in your source waters near the intake?” Only responses to this question of “Yes,” “No,” or “Don’t know” were considered. Some PWSs did not respond, while several PWSs recorded multiple responses over the time period. This resulted in 99 UCMR 4 qualitative responses for comparison to satellite imagery.

If the PWS responded “Yes,” they were asked to specify when the algal bloom was observed. Available responses included: the day the UCMR 4 cyanotoxin sample was collected, between the day the sample was collected and the past week, between the past week and the past month, between the past month and the past 12 months, and more than a year ago. Each PWS was asked to select all that applied. When PWSs responded "Yes," this study considered algal blooms observed between the day the cyanotoxin sample was collected and the past month. This framework can lead to limitations in the temporal matchup between UCMR 4 qualitative responses and satellite observations. Additionally, it is not possible to confirm that UCMR 4 qualitative responses identified the presence of cyanobacterial blooms specifically rather than other types of algal blooms.

Despite potential temporal limitations, these visual observation responses provided via UCMR 4 are ideal for satellite comparison given that the satellite signal also measures the water's surface, penetrating only up to a depth of about 2 m for a typical satellite in clear water (Mishra et al., 2005) and less than 2 m in more turbid waters (Wynne et al., 2010). This comparison is helpful in interpreting the UCMR 4 qualitative responses by using satellite data to validate the presence or absence of cyanobacteria with visual observations.

After identifying the drinking water intake locations corresponding to each UCMR 4 qualitative response, intake locations were subset to those identified as resolvable as described in Section 2.2. A total of 22 intakes with UCMR 4 responses from March 2018 through November 2019 corresponded to a resolvable drinking water intake location, representing 11 lakes across 6 states (**Figure 1**). Low spatial coverage of UCMR 4 qualitative responses is the result of both sample design and sample reporting. While all large surface water systems are required to sample cyanotoxins in finished water as part of UCMR 4, only 800 small systems are required to sample. Additionally, not all PWS submitted qualitative source water data as part of their UCMR 4 finished water cyanotoxin sampling. Drinking water intakes assigned to the systems sampled then needed to correspond to a lake observable with 300-m satellite imagery and fit the selection criteria described in Section 2.3.

Responses were collected at a subset of PWS facilities. UCMR 4 responses are a qualitative visual response corresponding to the presence or absence of surface algal blooms near the intake. Hereafter, these responses will be referred to more generally as “UCMR 4 qualitative responses.” UCMR 4 data collection was completed in November 2020; Data from this study spanned March 2018 through November 2019 and represents a fraction of data from systems required to sample and an even smaller fraction have reported their results leading to a temporal lag associated with UCMR 4 qualitative responses. Spatial coverage of these locations will likely improve as all UCMR 4 data becomes available.

2.4 Comparing UCMR 4 qualitative responses to satellite observations

Satellite data were extracted for each UCMR 4 qualitative response location by taking the average CI-cyano value of all valid pixels contained within a 900-m buffer of the drinking water intake as descried in Section 2.3. Each date associated with the UCMR 4 quantitative sampling was matched to the corresponding satellite weekly composite. This produced a cyanobacterial abundance estimate to accompany the observed presence or absence of an algal bloom at the source waters near each intake.

To assess the agreement between the two datasets, two approaches were used. First, a presence-absence agreement matrix was developed to compare, on a class-by-class basis, binary satellite data and binary UCMR 4 qualitative responses. Overall agreement was computed as the number of instances that generated the same response in both satellite data and UCMR 4 qualitative responses normalized to the total number of instances considered. The Kappa coefficient was computed to indicate how well the two datasets agreed compared to a random assignment of classes (Cohen, 1960; Goodman and Kruskal, 1954). Kappa is a ratio between -1 and 1 where higher values indicate better agreement and was computed via the fmsb package in R version 4.0.0 (Nakazawa, 2019; R Core Team, 2020).

Next, the non-parametric Mann-Whitney U test was used to assess if cyanobacterial abundance values for UCMR 4 qualitative responses of “Yes” and “No” were generated from the same population (Mann and Whitney, 1947; Wilcoxon, 1945). A nonparametric approach is appropriate here for several reasons: the data are not normally distributed, the sample size is relatively small, and the satellite observations contain non-detects. Cohen’s d was then used to quantify the effect size (Cohen, 1992) via the effsize package in R version 4.0.0 (R Core Team, 2020; Torchiano, 2020), where, generally, absolute values above 0.5 indicate a “large” difference between the two means. While p-values are provided with these statistical tests, they are not reported here. The conventional p-value is often reported because of its familiarity to many readers although it provides negligible information on the validity of the reported model (Wasserstein et al., 2019). Instead, effect size statistics are used to characterize results.

2.5 Assessing bloom frequency at all resolvable drinking water sources

To assess the frequency of cyanobacterial blooms at all resolvable source waters near each drinking water intake (see **Figure 2**), satellite observations were aggregated into annual detections. Frequency was computed per pixel as the proportion of valid satellite pixels that indicate either a detection of cyanobacteria (i.e., those above the detection limit of the sensor) or non-detection, where invalid pixels are those with quality flags (**Figure 3**). In other words, bloom frequency is simply the cyanobacteria detected pixels divided by the total number of detect and non-detect pixels, excluding invalid quality flagged pixels. This produces a percentage between 0 and 100, where 0% indicates no bloom was present at that pixel for the given year and 100% indicates a bloom was always present at that pixel for the given year. At each drinking water source, annual bloom frequency for the year 2019 represented the average bloom frequencies for all pixels contained within a 900 m buffer of each drinking water intake.

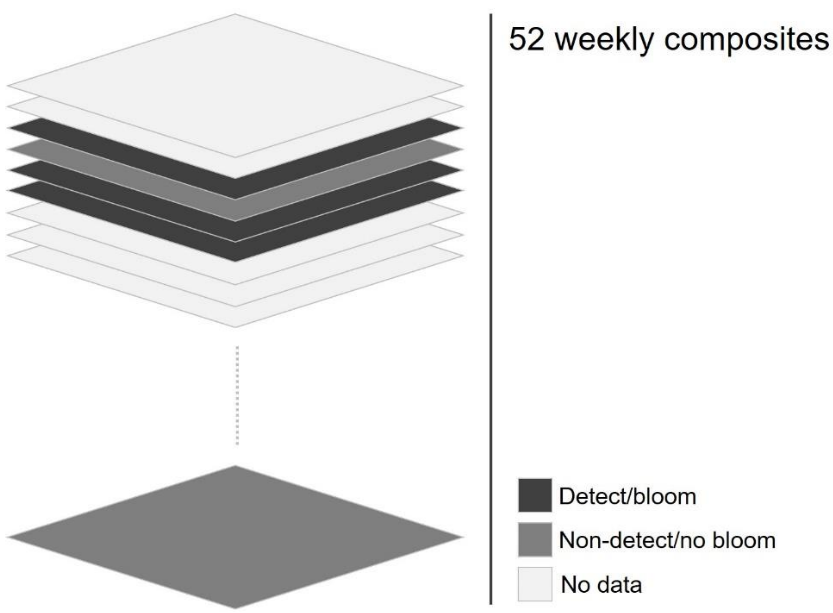

Figure 3. A conceptual diagram illustrating the computation of annual bloom frequency. At each pixel, annual bloom frequency is calculated from weekly composite imagery as the proportion of valid pixels above the detection limit of the sensor. In other words, annual bloom frequency is simply the detect pixels divided by the total number of detect and non-detect pixels.

2.6 Quantifying effect size at all resolvable drinking water source waters

To quantify effect size at all resolvable drinking water source waters, a γ statistic was used which is conceptually equivalent to Cohen's d and has been used for several environmental applications (Coffer and Hestir, 2019; Henson et al., 2010; Urquhart et al., 2017). In this study, this statistic was used to determine the number of observations needed for a trend in the data to be sustained despite the residual variability in the data and can provide insight into how many years of data must be obtained to increase confidence in an observed change (Equation 1). If γ is less than the time period of observations, the magnitude of the trend exceeds the residual variability in the data.

To compute γ, cyanobacterial abundance values were first extracted within the previously described 900 m buffer of each drinking water intake. CI-cyano values for all pixels contained in or intersecting this buffer were averaged for each weekly composite satellite image. Weekly averages were assigned months based on the middle day of the week, and monthly averages were computed for June 2016 through April 2020. These monthly averages were used to quantify γ at each intake, and those with a γ of less than four years were considered for a trend analysis. The γ statistic was computed as:

$$\text{Effect size } (\gamma) = \frac{\sqrt{\frac{\Sigma_1^n (y-\hat{y})^2}{n-1}}}{|m|} \qquad \text{(Equation 1)}$$

where n is the sample size, ŷ represents the residuals of y, and m is the Thiel-Sen Slope.

The Thiel-Sen slope determines the magnitude of the trend by computing the slope for all pairs of data and taking their median (Sen, 1968; Theil, 1992). Relatively short time series have been used in previous studies for trend detection. Kim et al. (2007) assessed linear trends in air quality using three and five years of satellite data. Psilovikos et al. (2006) analyzed trends in water quality using three years of field observations. To assess short-term trends at each drinking water sources, the nonparametric seasonal Mann Kendall test for trend and the associated Thiel-Sen Slope were computed. The seasonal Mann Kendall test for trend is a variation of the Mann Kendall test for trend (Kendall, 1955; Mann, 1945), checking for a monotonic increase or decrease across the time series. The trend analysis was performed via the rkt package in R version 4.0.0 (Marchetto, 2017; R Core Team, 2020).

3 Results

3.1 Agreement between UCMR 4 qualitative responses and satellite observations

Of the 99 UCMR 4 qualitative responses in drinking water sources corresponding to satellite imagery, in responding to the question of whether there was an algal bloom preceding the sampling event, 15 responded “Don’t know,” 76 responded “No,” and 8 responded “Yes.” Those that responded “Yes” indicated this algal bloom was present between the day of quantitative sampling and the past month.

72 of the 76 UCMR 4 qualitative responses in drinking water sources of “No” corresponded to an absence of cyanobacteria in satellite imagery, and 7 of the 8 UCMR 4 qualitative responses in drinking water sources of “Yes” corresponded to a presence of cyanobacteria in satellite imagery (**Table 1**). There were five UCMR 4 qualitative responses in drinking water sources that

disagreed with satellite imagery, one in which the UCMR 4 qualitative response in drinking water sources indicated a bloom was present while satellite imagery indicated a bloom was absent and four in which the UCMR 4 qualitative responses in drinking water sources indicated a bloom was absent and satellite imagery indicated a bloom was present. This corresponded to an overall accuracy of 94.05% and a Kappa coefficient of 0.704.

Table 1. An agreement matrix analyzing cyanobacteria presence and absence as indicated by UCMR 4 qualitative responses in drinking water sources and cyanobacteria detect and non-detect as indicated by satellite imagery.

	Satellite-derived cyanobacteria	
UCMR 4 qualitative response	Detect	Non-detect
Algal bloom observed	7	1
Algal bloom not observed	4	72

In addition to cyanobacterial presence and absence, the satellite-derived cyanobacterial abundance was analyzed for each of the 99 UCMR 4 qualitative responses in drinking water sources (**Figure 4**). For all UCMR 4 qualitative responses in drinking water sources in which the observer did not know if an algal bloom was present, satellite imagery indicated non-detection of cyanobacteria. When UCMR 4 qualitative responses in drinking water sources indicated an algal bloom was not observed, median cyanobacterial abundance corresponded to the detection limit of the satellite imagery. When UCMR 4 qualitative responses in drinking water sources indicated an algal bloom was observed, median cyanobacterial abundance exceeded 1,200,000 cells/mL. Results of the Mann Whitney U test and associated Cohen's d indicate satellite-estimated cyanobacterial abundance corresponding to UCMR 4 qualitative responses of "Yes" and "No" are not derived from the same population (U = 82, n = 84, Cohen's d = -4.14). This suggests that visual observations during UCMR 4 monitoring and satellite observations have strong agreement in assessing cyanobacterial occurrence at drinking water source waters.

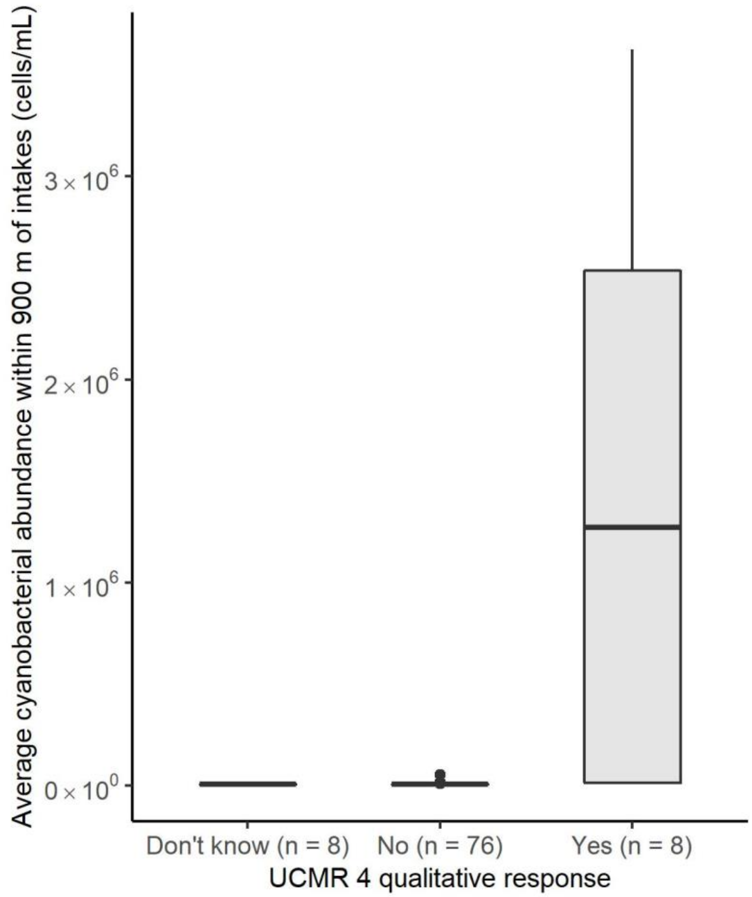

Figure 4. Boxplots representing satellite-derived cyanobacterial abundance corresponding to fourth Unregulated Contaminant Monitoring Rule (UCMR 4) qualitative responses in drinking water sources. Satellite-derived cyanobacterial abundance was averaged within a 900 m buffer of drinking water intakes containing UCMR 4 data. UCMR 4 qualitative responses in drinking water sources (n = 99) of “Don’t know,” “No,” and “Yes” were considered regarding whether a visible algal bloom was present within one month of quantitative sampling.

3.2 Bloom frequency at drinking water sources

For the year 2019, average annual bloom frequency was assessed at all 685 resolvable drinking water sources, not just those corresponding to UCMR 4 qualitative responses. For each weekly composite, an average of 19 satellite pixels were considered within a 900 m buffer of each drinking water intake to compute average annual bloom frequency. Average bloom frequency in 2019 peaked at 100%, meaning that for all valid satellite pixels, the average of those closest to the intake always indicated a cyanobacterial bloom was present (**Figure 5A**). Average bloom frequency reached 100% at source waters in Morgan Lake, NM and Grand Lake St. Mary's, OH throughout the entire year in 2019. Despite relatively high average bloom frequency within 900 m at several intakes, the majority of the distribution fell below the third quartile at 13%, and the median was 2%. Outliers existed at source waters with an average frequency above 35%.

The four states with the maximum number of resolvable drinking water sources were selected to demonstrate cyanobacterial frequency in more detail (**Figure 5B**). Texas contains 130 resolvable intakes whose statewide average bloom frequency was 18% in 2019, exceeding the third quartile of all resolvable intakes for the same period of time. Three source waters had an average bloom frequency of 80% in 2019 while all others were below 70%. New York contains 96 resolvable intakes which averaged the lowest statewide bloom frequency in 2019 of these four states at only 2%, equivalent to the median of all resolvable source waters. The resolvable source waters with the highest average bloom frequency in New York were below 20%. California contains 75 resolvable intakes that exhibited a statewide average bloom frequency of 3% in 2019. Two source waters had the highest average frequencies for this state with values of 50%. Over half of the resolvable source waters in California had an average bloom frequency of 0% for 2019.

Oklahoma contains 71 resolvable intakes that exhibited a statewide average bloom frequency of 5% in 2019. The source waters that exhibited the highest average bloom frequency had a value below 50%, and many of the subsequently ranked source waters showed a relatively high average bloom frequencies compared to New York and California.

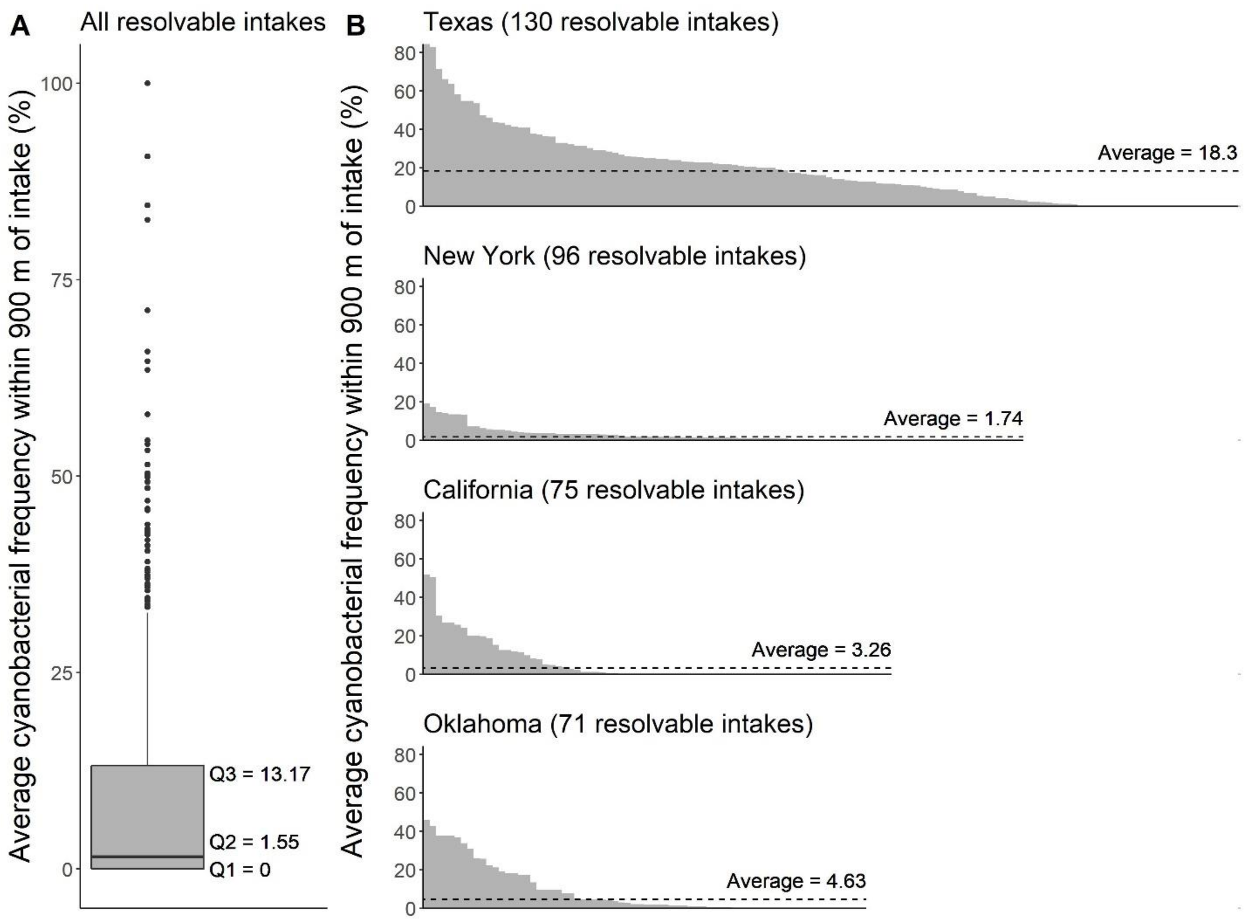

Figure 5. (A) Distribution of average cyanobacterial bloom frequency for 2019 within 900 m of all 685 resolvable drinking water intakes. (B) Average cyanobacterial bloom frequency for 2019 within 900 m for resolvable drinking water intakes in the states of Texas, New York, California, and Oklahoma. The length of the x-axis reflects the number of resolvable intakes in each state. Average bloom frequency for each state is represented by the dashed line.

3.3 Analysis of effect size at drinking water sources

Effect size was analyzed at all 685 resolvable drinking water sources, as described in Section 2.7. There were five source waters that were excluded due to low temporal coverage as they did not contain at least four observations for any given month in that time period. This left 680 resolvable source waters to include in the analysis of effect size. A trend analysis was first applied to average monthly frequencies, but no source waters had an effect size indicative of a sustained change (i.e. $\gamma \leq 4$ years), so this metric was not considered further. Instead, a trend analysis was applied to average satellite-derived cyanobacterial abundance values (cells/mL). Thus, results presented here report on changes in cyanobacterial abundance while more data would be required to identify changes in temporal frequency.

A time period of four years did not provide sufficient cyanobacterial abundance data to determine a sustained trend amid inherent variability in the data for nearly all resolvable source waters, instead requiring a median temporal period of just over a decade of observations given current sampling frequency (**Figure 6**). The nature of the γ statistic requires a detectable slope in order for this statistic to be quantified, and a relatively small slope will result in a very large γ. Thus, a cutoff on γ of 50 years was selected for **Figure 6** to focus the analysis on more achievable monitoring time periods, which resulted in a subset of 36 intakes being selected for computing the median γ statistic.

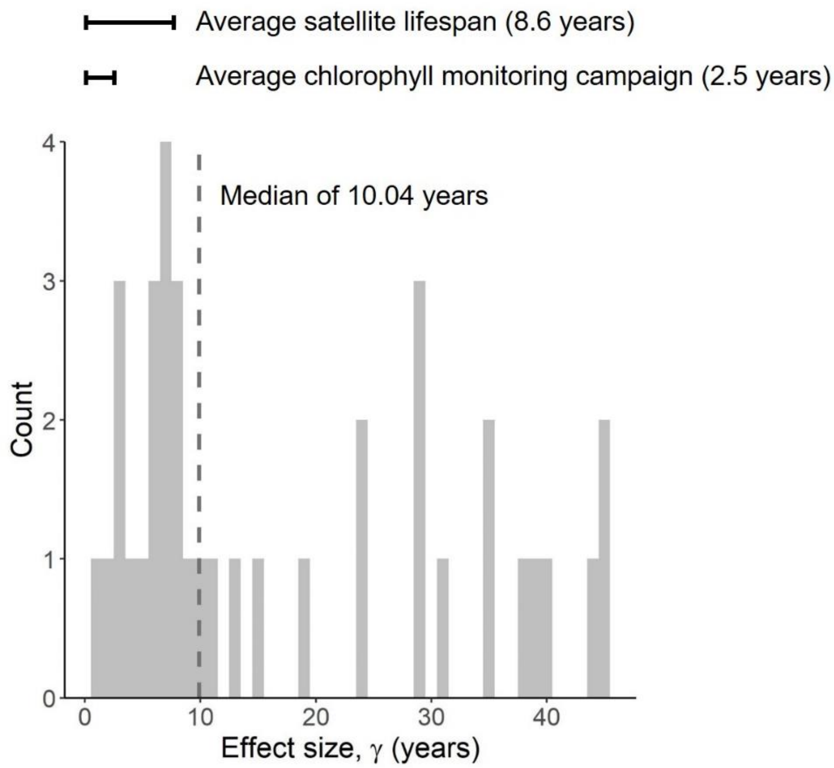

Figure 6. A histogram of the effect size (γ) representing the length of observations needed for the current trend to exceed the residual variability at 36 source waters, selected based on a γ of less than 50 years. The median γ value was 10.04 years based on current sampling frequency. This value is slightly higher than the average satellite lifespan from the 1990's of 8.6 years (Belward and Skøien, 2015) and nearly 8 years longer than the average water quality field campaign for chlorophyll measurements based on information from the Water Quality Portal. Chlorophyll monitoring was used as a proxy for cyanobacteria monitoring as field monitoring for cyanobacteria typically do not report results to larger databases and are only available at the state or local level.

Five source waters did exhibit an effect size indicative of a sustained trend from June 2016 through April 2020 (γ ≤ 4 years), but conclusions cannot be drawn regarding changes that may have occurred outside of this time period (**Table 2**, **Figure 7**). Source waters at Morgan Lake, NM increased in average cyanobacterial abundance by 60% per year from 2016 to 2020, and a γ of 3 years indicates that this increase represents a sustained trend. Source waters at Lake

Overholser, OK, Grand Lake St. Mary's, OH, Choke Canyon Reservoir, TX, and Lake Eufaula, OK decreased in cyanobacterial abundance from 2016 to 2020. Lake Overholser, OK decreased by 30% per year and exhibited the lowest γ of the entire dataset, requiring only 1 year of observations to draw a conclusion about the observed trend. Grand Lake St. Mary's, OH decreased in cyanobacterial abundance by only 10% per year, but the γ statistic still supported a sustained trend requiring 3 years of data. Both Choke Canyon Reservoir, TX and Lake Eufaula, OK decreased by 20% per year and required 3 years of observations for the trend to overcome residual variability in the data.

Table 2. Results of a short-term trend analysis using satellite imagery at five drinking water sources that exhibited a sustained trend ($\gamma \leq 4$ years) based on monthly observations spanning June 2016 through April 2020; effect size is expressed in years. A negative change indicates a decrease in cyanobacterial frequency over the time period considered.

	Sample size	**Kendall's tau**	**Annual percent change**	**Effect size (γ)**
Morgan Lake, NM	47	0.4	60%	3
Lake Overholser, OK	47	-0.7	-30%	1
Grand Lake St. Mary's, OH	40	-0.7	-10%	3
Choke Canyon Reservoir, TX	47	-0.4	-20%	3
Lake Eufaula, OK	47	-0.5	-20%	3

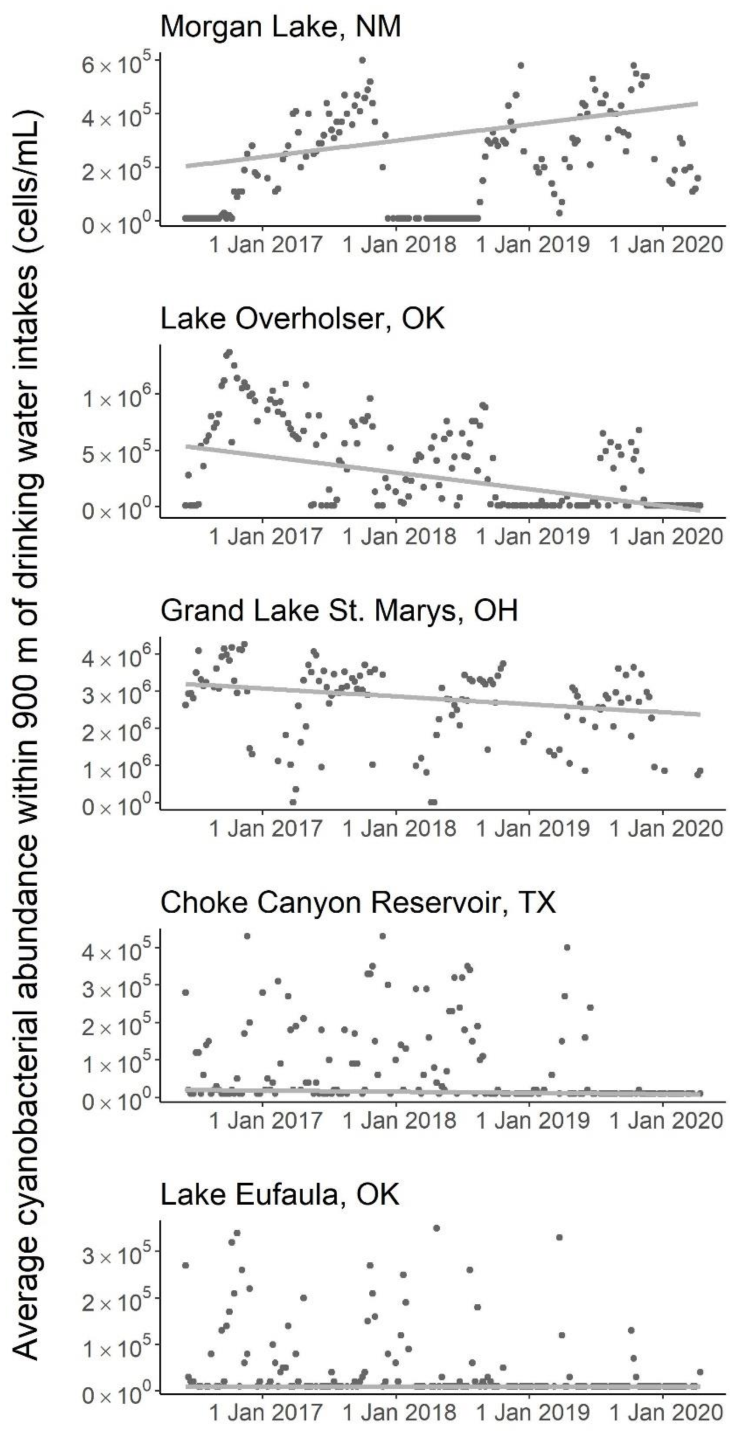

Figure 7. Time series of average cyanobacterial abundance within 900 m of the drinking water intakes at Morgan Lake, NM, Lake Overholser, OK, Grand Lake St. Mary's, OH, Choke Canyon Reservoir, TX, and Lake Eufaula, OK. These five drinking water sources had an effect size less than the time period of observations ($\gamma \leq 4$ years) and were thus considered to have a sustained trend. The gray line represents the Thiel-Sen slope accompanying the change detection.

4 Discussion

4.1 Comparison of satellite-derived data with field observations

This study serves as the first quantitative comparison between satellite remote sensing data and UCMR 4 qualitative responses, providing an assessment of two independent approaches for assessing the presence of cyanobacterial blooms in drinking water sources. Agreement between UCMR 4 qualitative responses in drinking water sources of algal presence and satellite-derived cyanobacterial abundances increase confidence in both the accuracy of PWS samplers' visual interpretation of algal blooms and the use of satellite imagery for detecting cyanobacteria at surface source waters. A Kappa coefficient of 0.71 was found between the two datasets. Kappa coefficients between 0.60 and 0.79 are considered to have a moderate level of agreement (McHugh, 2012).

While 79 responses agreed between the two datasets, there were five disagreements. In four cases, UCMR 4 qualitative responses in drinking water sources recorded no visual observation of an algal bloom, but corresponding satellite measurements indicated cyanobacteria detections were present. At these four cases, at least one of the pixels extracted within a 900 m buffer of the intake had a non-detect, but other pixels within the 900 m buffer did have detects, resulting in the aggregation of these pixels indicating cyanobacteria presence. Thus, the discrepancy could partially be explained by spatial mismatches between the exact visual observations and the 900 m buffer. Additionally, temporal offset between the two datasets could exist.

In one case, UCMR 4 qualitative responses in drinking water sources recorded a bloom, but corresponding satellite measurements indicated non-detect. For this sample, the UCMR 4 qualitative response in drinking water sources to the question "Preceding the finished water sample collection, did you observe an algal bloom in your source waters near the intake?" was that an algal bloom was observed between the past week and past month. A temporal offset could explain this discrepancy, or a bloom could have been present below the detection limit of the satellite sensor. Additionally, it is possible to have cyanobacteria with no detectable surface bloom, particularly given that cyanobacteria can move horizontally and vertically throughout the water column within hours (Qi et al., 2018; Qin et al., 2018). A surface bloom could have been present at the time of UCMR 4 data collection but not at the time of satellite overpass as it may have moved within the water column. Moreover, the ability of the satellite to detect picocyanobacteria is still uncertain; picocyanobacteria could have been observed during UCMR 4 data collection, but not registered through the CI-cyano algorithm (Śliwińska-Wilczewska et al., 2018).

4.2 Large-scale assessments of cyanobacterial frequency at source waters

Monitoring and assessment of cyanobacterial blooms has not been routinely conducted in a nationally consistent manner with adequate spatial and temporal resolution. Infrequent field monitoring has been conducted at the national level, including the National Lakes Assessment occurring every five years in the United States (NLA; Blocksom et al., 2016). Regional field monitoring has also been conducted, including across 142 Chinese lakes and reservoirs over two multi-year periods (Huang et al., 2020). As field monitoring can be both time- and cost-intensive, satellite-based monitoring could be included as a supplemental tool for monitoring cyanobacterial blooms. Satellite observations offer the potential for increased temporal and spatial resolution when lakes are of sufficient size and in the absence of cloud cover which has been demonstrated in previous studies (Coffer et al., 2020; Duan et al., 2017; Zhang et al., 2017).

Satellite-based monitoring has shown promise for detection of cyanobacterial blooms to assist with early warning which allows utilities to respond more effectively. However, field efforts such as the NLA, state, and local efforts are still required to validate satellite observations and measure toxins and other parameters not resolvable with satellite imagery, particularly in areas not observable using satellite imagery such as the land-water interface.

Despite efforts to monitor cyanobacterial blooms across broad spatial and temporal scales, monitoring specific to drinking water sources is not routinely collected at the national level. In the US, Clark et al. (2017) used satellite imagery from the MEdium Resolution Imaging Spectrometer (MERIS) spanning 2008-2011 to assess cyanobacterial bloom frequency at source waters in the states of Florida and Ohio. The average cyanobacterial frequency for all resolvable source waters in Florida was 30% and for Ohio, 5%. Using a different method to extract nearby satellite pixels at each intake and using a different satellite sensor, Clark et al. (2017) found Grand Lake St. Mary's to have the highest temporal frequency for the state of Ohio at 83% from 2008 through 2011.

This study presents the first large-scale assessment of cyanobacterial frequency and abundance at surface drinking water intakes across the US. National-level assessments of cyanobacterial occurrence at drinking water sources have not been conducted through either field or satellite observations. Upon completion of data reporting, UCMR 4 will serve as the first field-based dataset of cyanobacteria in source waters across the US, while methods presented here can be used to monitor approximately 700 drinking water sources across 44 states with consistent temporal coverage in the absence of cloud contamination or snow and ice cover.

Excessive levels of cyanobacteria and their toxins can have significant public health, environmental, and economic consequences (Anderson et al., 2000; Hallegraeff, 2003; Smayda, 2003), including the human health risks posed by elevated levels of cyanotoxins in finished drinking water. Results presented here suggest that satellite imagery can be an important pre-screening tool that drinking water quality managers may use for early detection of cyanobacteria in their drinking water sources. Cost-effective and timely early detection of cyanobacteria in source waters can help inform critical treatment, monitoring, and management steps from PWSs, protecting drinking water quality from the risks posed by cyanotoxins and cyanobacteria and improving the quality of finished drinking water to ensure public health.

4.3 Assessing effect size of cyanobacterial abundance

Anderson et al. (2002) indicated coastal systems in recent decades had increased in occurrence of toxic and otherwise harmful algal blooms, but did not provide quantitative evidence of this change. It was noted, however, that this increase could either reflect heightened scientific awareness or an actual increase in the number, magnitude, or frequency of blooms (Anderson, 1989). A lack of historic data was cited as a limitation for quantifying long-term change. He et al. (2016) also indicated the frequency of cyanobacterial blooms in freshwater systems is increasing. More recently, Huisman et al. (2018) summarized projected increases in cyanobacterial occurrence due to eutrophication, rising CO2 levels, and changing climatic conditions. Despite repeated suggestions that cyanobacterial blooms have or will increase, few large-scale trend analyses have been performed to support this claim.

Using over 200 years of sediment cores from northern hemisphere lakes, Taranu et al. (2015) suggested that cyanobacteria have increased substantially in almost 60% of lakes since the industrial revolution and that cyanobacteria have increased disproportionally compared to other phytoplankton. Using satellite imagery, Urquhart et al. (2017) analyzed changes in spatial extent of cyanobacterial blooms from 2008 through 2011 for large lakes in the states of California, Ohio, and Florida. Florida indicated an increase in spatial extent of blooms but exhibited a γ of 4.1 over the 4-year time series, suggesting the observed trend did not quite statistically outweigh residual variability in the data.

This study found that a median of over 10 years of observations were needed for observed changes to show a sustained trend outside of the residual variability in the data given current sampling frequency. For reference, the average satellite lifespan was 8.6 years in the 1990's (Belward and Skøien, 2015) and the average water quality field campaign for chlorophyll monitoring lasts approximately 2.5 years. The average length of water quality field monitoring was found by averaging the difference between start years and end years for all Water Quality Portal (https://www.waterqualitydata.us) datasets with a characteristic name "chlorophyll". Chlorophyll monitoring was used as a proxy for cyanobacteria monitoring as field measurements for cyanobacteria typically are often only available through state or local databases (U.S. EPA, 2020). Belward and Skøien (2015) also summarized satellite lifespans for more recent decades, but these values were artificially reduced given that many of the sensors considered were at the beginning of their life cycles.

OLCI completed its fourth full year of data collection in June 2020. The operational lifespan of Sentinel-3A is set to seven years with consumables available for up to twelve. An identical sensor is housed on ESA's Sentinel-3B satellite platform, launched in 2018. Moving forward, ESA plans to ensure consistent, long-term coverage through the launch of Sentinel-3C and Sentinel-3D. Upon successful launch of all four satellites in the Sentinel-3 satellite series, mission continuity will then be expected for at least 25 years from the launch of Sentinel-3A. Thus, the Sentinel-3 satellite constellation offers promise for providing sufficient temporal coverage to observe sustained changes at drinking water sources.

Schaeffer et al. (2013) found that mission continuity is critical for end-users. Findings here also encourage the longevity of monitoring programs, both satellite-based and field campaigns, in order to defend or refute statements regarding large-scale changes in cyanobacterial frequency, extent, and abundance. Insufficient temporal coverage was a primary concern for this study with nearly all drinking water sources failing to achieve a γ less than the time period of observations. Additionally, the median required time period of 10.04 years was based on an assumed sampling frequency and could be longer if the frequency of observations decreases compared to the reference 2016-2020 period used here. This supports the need for continued, consistent monitoring to better understand long-term cyanobacterial bloom trends in drinking water sources. The planned constellation of Sentinel-3 satellites will improve temporal coverage in the future.

Despite the need for increased temporal coverage, source waters at five intakes did exhibit a sustained trend from 2016 to 2020, but these trends cannot be extrapolated outside of this time period and are not indicative of ongoing changes. Morgan Lake is located on the Navajo Nation in northwest New Mexico. This source water exhibited the highest possible bloom frequency and was the only source water considered to increase in abundance. Lake Overholser is located in Oklahoma City, OK and decreased in cyanobacterial abundance from 2016 to 2020. Grand Lake St. Mary's in western Ohio once ranked in the 99th percentile for microcystins in the US (U.S. EPA, 2009). While Jacquemin et al. (2018) found significant improvements in water quality over the past decade, they concluded that this lake's waters remain impaired. Choke Canyon Reservoir in southern Texas provides drinking water for the City of Corpus Christi, and Lake Eufaula, Oklahoma's largest lake, provides drinking water to Eufaula, OK. At both of these source waters, changes were driven by much lower cyanobacterial abundance values in the last year of observations compared to the first three years. Temporal patterns at these sites resembled more of a step change rather than a trend, but insufficient information exists to determine a potential cause of the sudden decline in cyanobacterial abundances. At all sites, additional information would be needed to determine drivers of these changes given the short time period considered.

4.4 Limitations

While this study offers the first large-scale investigation of cyanobacterial frequency and abundance at drinking water sources across the US, there are several limitations that must be considered. Only drinking water intakes located in or near relatively large lakes were considered and pixels that fell along the land/water interface were discarded, meaning approximately 80% of all drinking water intakes were not studied. When considering a subset of these drinking water intakes for matching with UCMR 4 qualitative responses in drinking water sources, coverage was even lower as UCMR 4 sampling was ongoing through the end of 2020. This study only considered UCMR 4 data reported up to April 2020 and represented a portion of data collected up to November 2019. The estimated PWS locations are based on the best available locational data provided by the states in SDWIS and are chosen to represent a PWS for this national-scale analysis. In some cases, this may cause discrepancies given the 100 m buffer used to assign a lake to each intake. Applying a similar analysis to finer resolution sensors such as Sentinel-2 at 20 m multispectral resolution or Landsat-8 at 30 m multispectral resolution could improve spatial coverage. Sentinel-2 has the potential for detecting chlorophyll (Gilerson et al., 2010; Pahlevan et al., 2020), but cyanobacteria-specific algorithms have yet to be validated for large-scale applications.

Satellite observations of cyanobacterial frequency or abundance do not represent levels in finished drinking water. When investigating cyanobacterial abundance near these intakes, it is important to remember that this analysis focuses on source waters only. The quality of finished drinking water is a reflection of treatment practices employed by the PWS in response to changes in intake water quality. For example, a 2016 report found 43.9% of source waters in Ohio to exceed the total microcystins U.S. EPA Health Advisory level for young children and vulnerable populations of 0.3 μg/L, but only 1.16% of treated drinking water samples exceeded this threshold (AWWA, 2016), demonstrating effective treatment practices for the intakes considered. Moreover, satellite imagery can only detect cyanobacteria, not the presence of cyanotoxins (Stumpf et al., 2016a), and it is possible for both a visible bloom to be present without cyanotoxins and cyanotoxins to be present without a visible bloom. This issue is further complicated by the presence and the possibility of the growth/regrowth of cyanobacteria within the treatment utility, potentially leading to toxin or taste and odor production even in the absence of a bloom in the source water (Almuhtaram et al., 2018; Greenstein et al., 2020).

Several limitations exist in the acquisition of satellite imagery. Data gaps exist due to cloud cover and the presence of snow and ice. Northern latitude regions are particularly affected by lower data coverage in the winter months (Coffer et al., 2020), although during the cold season proliferation of cyanobacterial blooms is believed to be more limited. However, occasional blooms and in some cases cyanotoxins have been noted under ice (Bertilsson et al., 2013; Hampton et al., 2017; Üveges et al., 2012; Wejnerowski et al., 2018). Additionally, difficulties can arise in performing short-term trend analyses given limited observations. Satellites typically cannot detect benthic cyanobacteria except in the case of optically shallow water. However, benthic systems can contribute to contamination of drinking water sources (Gaget et al., 2017). Moreover, drinking water intakes can be located at a water's surface or at depths of up to 30 to 40 m (Hoeger et al., 2005), but the satellite signal is only able to penetrate the top later of the water column, typically up to 2 m for a typical satellite in clear water (Mishra et al., 2005) and less than 2 m in more turbid waters (Wynne et al., 2010). This vertical offset can be important if using this information to inform drinking water management approaches. A vertical offset is not accounted for here and is difficult to address given that some intakes have several depths at which water can be drawn, which can be adjusted to accommodate water level and water quality (U.S. EPA, 2016a).

5 Conclusions

This study used satellite imagery to detect cyanobacteria at nearly 700 drinking water sources across the US. Additionally, agreement between a subset of 22 of these source waters and visual observations extracted from UCMR 4 qualitative responses indicating the presence/absence of a visible surface algal bloom was analyzed. The following conclusions were reached:

- A subset of UCMR 4 qualitative responses in drinking water sources spanning March 2018 through November 2019 and corresponding satellite-derived cyanobacteria detect and non-detect measurements demonstrated high agreement, achieving an overall accuracy of 94% and a Kappa coefficient of 0.70 across 84 observations. This demonstrates the utility for use of satellite imagery as a complement to ground-based measurements for assessing cyanobacterial occurrence at drinking water sources.
- Across all resolvable drinking water sources, the majority of detectable cyanobacterial bloom frequencies for 2019 averaged less than 35%, but several outliers existed at higher frequencies reaching a maximum value of 100% for source waters at two drinking water intakes.
- Nearly all source waters analyzed did not have sufficient data for a trend analysis, as suggested by effect size statistics that were longer than the time period of observations. Instead, a decade of observations would be required for trends to outweigh residual variability in the data.
- Five source waters demonstrated a short-term trend from June 2016 through April 2020 with source waters at one intake increasing in cyanobacterial abundance over this time period and source waters at four intakes decreasing in cyanobacterial abundance. However, conclusions are only valid within the observed time period and cannot be

extrapolated to support long-term trends at any source waters. Additional data are needed to determine drivers of these changes.

REFERENCES

Almuhtaram, H., Cui, Y., Zamyadi, A., Hofmann, R., 2018. Cyanotoxins and Cyanobacteria Cell Accumulations in Drinking Water Treatment Plants with a Low Risk of Bloom Formation at the Source. Toxins (Basel). 10, 430. https://doi.org/10.3390/toxins10110430

Anderson, D.M., 1989. Toxic algal blooms and red tides: a global perspective. Red tides Biol. Environ. Sci. Toxicol. 11–16.

Anderson, D.M., Glibert, P.M., Burkholder, J.M., 2002. Harmful algal blooms and eutrophication: Nutrient sources, composition, and consequences. Estuaries 25, 704–726. https://doi.org/10.1007/BF02804901

Anderson, D.M., Hoagland, P., Kaoru, Y., White, A.W., 2000. Estimated annual economic impacts from harmful algal blooms (HABs) in the United States. National Oceanic and Atmospheric Administration, Norman, OK.

AWWA, 2016. Cyanotoxins in US Drinking Water: Occurrence, Case Studies and State Approaches to Regulation. Denver, CO.

Belward, A.S., Skøien, J.O., 2015. Who launched what, when and why; trends in global land-cover observation capacity from civilian earth observation satellites. ISPRS J. Photogramm. Remote Sens. 103, 115–128. https://doi.org/https://doi.org/10.1016/j.isprsjprs.2014.03.009

Bertilsson, S., Burgin, A., Carey, C.C., Fey, S.B., Grossart, H.-P., Grubisic, L.M., Jones, I.D., Kirillin, G., Lennon, J.T., Shade, A., Smyth, R.L., 2013. The under-ice microbiome of seasonally frozen lakes. Limnol. Ocean. 58. https://doi.org/10.4319/lo.2013.58.6.1998

Blocksom, K., Kaufmann, P., Kincaid, T., Olsen, T., Paulsen, S., Peck, D., Stoddard, J., Sickle, J. Van, Weber, M., Holdsworth, S., Landis, M., Lehmann, S., Mitchell, R., Soo-Hoo, M., 2016. National Lakes Assessment 2012.

Clark, J.M., Schaeffer, B.A., Darling, J.A., Urquhart, E.A., Johnston, J.M., Ignatius, A.R., Myer, M.H., Loftin, K.A., Werdell, P.J., Stumpf, R.P., 2017. Satellite monitoring of cyanobacterial harmful algal bloom frequency in recreational waters and drinking water sources. Ecol. Indic. 80, 84–95. https://doi.org/https://doi.org/10.1016/j.ecolind.2017.04.046

Coffer, M.M., Hestir, E.L., 2019. Variability in Trends and Indicators of CO_2 Exchange Across Arctic Wetlands. J. Geophys. Res. Biogeosciences 124, 1248–1264. https://doi.org/10.1029/2018JG004775

Coffer, M.M., Schaeffer, B.A., Darling, J.A., Urquhart, E.A., Salls, W.B., 2020. Quantifying national and regional cyanobacterial occurrence in US lakes using satellite remote sensing. Ecol. Indic. 111, 105976. https://doi.org/10.1016/j.ecolind.2019.105976

Cohen, J., 1992. A power primer. Psychol. Bull. 112, 155.

Cohen, J., 1960. A coefficient of agreement for nominal scales. Educ. Psychol. Meas. 20, 37–46. https://doi.org/10.1177/001316446002000104

Dieter, C.A., Maupin, M.A., Caldwell, R.R., Harris, M.A., Ivahnenko, T.I., Lovelace, J.K., Barber, N.L., Linsey, K.S., Survey, U.S.G., 2018. Estimated use of water in the United States in 2015, U.S. Geological Survey Circular 1441. https://doi.org/10.3133/cir1441

Duan, H., Tao, M., Loiselle, S.A., Zhao, W., Cao, Z., Ma, R., Tang, X., 2017. MODIS observations of cyanobacterial risks in a eutrophic lake: Implications for long-term safety evaluation in drinking-water source. Water Res. 122, 455–470. https://doi.org/https://doi.org/10.1016/j.watres.2017.06.022

Gaget, V., Humpage, A., Huang, Q., Monis, P., Brookes, J., 2017. Benthic cyanobacteria: A source of cylindrospermopsin and microcystin in Australian drinking water reservoirs. Water Res. 124. https://doi.org/10.1016/j.watres.2017.07.073

Gilerson, A.A., Gitelson, A.A., Zhou, J., Gurlin, D., Moses, W., Ioannou, I., Ahmed, S.A., 2010. Algorithms for remote estimation of chlorophyll-a in coastal and inland waters using red and near infrared bands. Opt. Express 18, 24109–24125.

GLCR, 2013. Microcystis Outbreak Closes Lake Erie Water Treatment Plant.

Goodman, L.A., Kruskal, W.H., 1954. Measures of Association for Cross Classifications. J. Am. Stat. Assoc. 49, 732–764. https://doi.org/10.1080/01621459.1954.10501231

Great Lakes Commission, 2014. City of Toledo Drinking Water Advisory and Ohio EPA Response to Harmful Algal Blooms.

Greenstein, K.E., Zamyadi, A., Glover, C.M., Adams, C., Rosenfeldt, E., Wert, E.C., 2020. Delayed Release of Intracellular Microcystin Following Partial Oxidation of Cultured and Naturally Occurring Cyanobacteria. Toxins (Basel). 12, 335. https://doi.org/10.3390/toxins12050335

Hallegraeff, G.M., 2003. Harmful algal blooms: a global overview. Man. harmful Mar. microalgae 33, 1–22.

Hampton, S.E., Galloway, A.W.E., Powers, S.M., Ozersky, T., Woo, K.H., Batt, R.D., Labou, S.G., O'Reilly, C.M., Sharma, S., Lottig, N.R., Stanley, E.H., North, R.L., Stockwell, J.D., Adrian, R., Weyhenmeyer, G.A., Arvola, L., Baulch, H.M., Bertani, I., Bowman, L.L., Carey, C.C., Catalan, J., Colom-Montero, W., Domine, L.M., Felip, M., Granados, I., Gries, C., Grossart, H.-P., Haberman, J., Haldna, M., Hayden, B., Higgins, S.N., Jolley, J.C., Kahilainen, K.K., Kaup, E., Kehoe, M.J., MacIntyre, S., Mackay, A.W., Mariash, H.L., McKay, R.M., Nixdorf, B., Nõges, P., Nõges, T., Palmer, M., Pierson, D.C., Post, D.M., Pruett, M.J., Rautio, M., Read, J.S., Roberts, S.L., Rücker, J., Sadro, S., Silow, E.A., Smith, D.E., Sterner, R.W., Swann, G.E.A., Timofeyev, M.A., Toro, M., Twiss, M.R., Vogt, R.J., Watson, S.B., Whiteford, E.J., Xenopoulos, M.A., 2017. Ecology under lake ice. Ecol. Lett. 20, 98–111. https://doi.org/10.1111/ele.12699

He, X., Liu, Y.L., Conklin, A., Westrick, J., Weavers, L.K., Dionysiou, D.D., Lenhart, J.J., Mouser, P.J., Szlag, D., Walker, H.W., 2016. Toxic cyanobacteria and drinking water: Impacts, detection, and treatment. Harmful Algae 54, 174–193. https://doi.org/10.1016/j.hal.2016.01.001

Henson, S.A., Sarmiento, J.L., Dunne, J.P., Bopp, L., Lima, I., Doney, S.C., John, J., Beaulieu, C., 2010. Detection of anthropogenic climate change in satellite records of ocean chlorophyll and productivity. Biogeosciences 7, 621–640. https://doi.org/10.5194/bg-7-621-2010

Hoeger, S.J., Hitzfeld, B.C., Dietrich, D.R., 2005. Occurrence and elimination of cyanobacterial toxins in drinking water treatment plants. Toxicol. Appl. Pharmacol. 203, 231–242.

Huang, J., Zhang, Y., Arhonditsis, G.B., Gao, J., Chen, Q., Peng, J., 2020. The magnitude and drivers of harmful algal blooms in China’s lakes and reservoirs: A national-scale characterization. Water Res. 181, 115902. https://doi.org/https://doi.org/10.1016/j.watres.2020.115902

Huisman, J., Codd, G.A., Paerl, H.W., Ibelings, B.W., Verspagen, J.M.H., Visser, P.M., 2018. Cyanobacterial blooms. Nat. Rev. Microbiol. 16, 471–483. https://doi.org/10.1038/s41579-018-0040-1

Jacquemin, S.J., Johnson, L.T., Dirksen, T.A., McGlinch, G., 2018. Changes in Water Quality of Grand Lake St. Marys Watershed Following Implementation of a Distressed Watershed Rules Package. J. Environ. Qual. 47, 113–120. https://doi.org/10.2134/jeq2017.08.0338

Kahru, M., Elmgren, R., 2014. Multidecadal time series of satellite-detected accumulations of cyanobacteria in the Baltic Sea. Biogeosciences 11, 3619.

Kendall, M.G., 1955. Rank correlation methods, 2nd ed., Rank correlation methods, 2nd ed. Hafner Publishing Co., Oxford, England.

Kim, S.-W., Heckel, A., Frost, G., Richter, A., Gleason, J., Burrows, J., McKeen, S., Hsie, E.-Y., Granier, C., Trainer, M., 2007. NO2 columns in the western United States observed from space and simulated by a regional chemistry model and their implications for NOx emissions. J. Geophys. Res. 114, D11301. https://doi.org/10.1029/2008JD011343

Lunetta, R.S., Schaeffer, B.A., Stumpf, R.P., Keith, D., Jacobs, S.A., Murphy, M.S., 2015. Evaluation of cyanobacteria cell count detection derived from MERIS imagery across the eastern USA. Remote Sens. Environ. 157, 24–34. https://doi.org/https://doi.org/10.1016/j.rse.2014.06.008

Mann, H.B., 1945. Nonparametric Tests Against Trend. Econometrica 13, 245–259. https://doi.org/10.2307/1907187

Mann, H.B., Whitney, D.R., 1947. On a Test of Whether one of Two Random Variables is Stochastically Larger than the Other. Ann. Math. Stat. 18, 50–60. https://doi.org/10.1214/AOMS/1177730491

Marchetto, A., 2017. rkt: Mann-Kendall Test, Seasonal and Regional Kendall Tests.

Matthews, M.W., Bernard, S., Robertson, L., 2012. An algorithm for detecting trophic status (chlorophyll-a), cyanobacterial-dominance, surface scums and floating vegetation in inland and coastal waters. Remote Sens. Environ. 124, 637–652. https://doi.org/https://doi.org/10.1016/j.rse.2012.05.032

Mishra, D.R., Narumalani, S., Rundquist, D., Lawson, M., 2005. Characterizing the vertical diffuse attenuation coefficient for downwelling irradiance in coastal waters: Implications for water penetration by high resolution satellite data. ISPRS J. Photogramm. Remote Sens. 60, 48–64. https://doi.org/https://doi.org/10.1016/j.isprsjprs.2005.09.003

Mishra, S., Stumpf, R.P., Schaeffer, B.A., Werdell, P.J., Loftin, K.A., Meredith, A., 2019. Measurement of Cyanobacterial Bloom Magnitude using Satellite Remote Sensing. Sci. Rep. 9, 18310. https://doi.org/10.1038/s41598-019-54453-y

Nakazawa, M., 2019. fmsb: Functions for Medical Statistics Book with some Demographic Data.

Pace, M.L., Batt, R.D., Buelo, C.D., Carpenter, S.R., Cole, J.J., Kurtzweil, J.T., Wilkinson, G.M., 2017. Reversal of a cyanobacterial bloom in response to early warnings. Proc. Natl. Acad. Sci. 114, 352–357.

Pahlevan, N., Smith, B., Schalles, J., Binding, C., Cao, Z., Ma, R., Alikas, K., Kangro, K., Gurlin, D., Hà, N., 2020. Seamless retrievals of chlorophyll-a from Sentinel-2 (MSI) and Sentinel-3 (OLCI) in inland and coastal waters: A machine-learning approach. Remote Sens. Environ. 111604.

Psilovikos, Aris, Margoni, S., Psilovikos, Antonios, 2006. Simulation and Trend Analysis of the Water Quality Monitoring Daily Data in Nestos River Delta. Contribution to the Sustainable Management and Results for the Years 2000–2002. Environ. Monit. Assess. 116, 543–562. https://doi.org/10.1007/s10661-006-7671-9

Qi, L., Hu, C., Visser, P.M., Ma, R., 2018. Diurnal changes of cyanobacteria blooms in Taihu Lake as derived from GOCI observations. Limnol. Oceanogr. 63, 1711–1726. https://doi.org/10.1002/lno.10802

Qin, B., Yang, G., Ma, J., Wu, T., Li, W., Liu, L., Deng, J., Zhou, J., 2018. Spatiotemporal Changes of Cyanobacterial Bloom in Large Shallow Eutrophic Lake Taihu, China. Front. Microbiol. 9, 451.

R Core Team, 2020. R: A Language and Environment for Statistical Computing.

Schaeffer, B.A., Iiames, J., Dwyer, J., Urquhart, E., Salls, W., Rover, J., Seegers, B., 2018. An initial validation of Landsat 5 and 7 derived surface water temperature for U.S. lakes, reservoirs, and estuaries. Int. J. Remote Sens. 1–17. https://doi.org/10.1080/01431161.2018.1471545

Schaeffer, B.A., Loftin, K.A., Stumpf, R.P., Werdell, P.J., 2015. Agencies collaborate, develop a cyanobacteria assessment network. Eos, Earth Sp. Sci. News 96. https://doi.org/10.1029/2015EO038809

Schaeffer, B.A., Schaeffer, K.G., Keith, D., Lunetta, R.S., Conmy, R., Gould, R.W., 2013. Barriers to adopting satellite remote sensing for water quality management. Int. J. Remote Sens. 34, 7534–7544. https://doi.org/10.1080/01431161.2013.823524

Sen, P.K., 1968. Estimates of the Regression Coefficient Based on Kendall’s Tau. J. Am. Stat. Assoc. 63, 1379–1389. https://doi.org/10.1080/01621459.1968.10480934

Smayda, T.J., 2003. What is a bloom? A commentary. Limnol. Oceanogr. 42, 1132–1136. https://doi.org/10.4319/lo.1997.42.5_part_2.1132

Stroming, S., Robertson, M., Mabee, B., Kuwayama, Y., Schaeffer, B., 2020. Quantifying the Human Health Benefits of Using Satellite Information to Detect Cyanobacterial Harmful Algal Blooms and Manage Recreational Advisories in U.S. Lakes. GeoHealth 4, e2020GH000254. https://doi.org/10.1029/2020GH000254

Stumpf, R.P., Davis, T.W., Wynne, T.T., Graham, J.L., Loftin, K.A., Johengen, T.H., Gossiaux, D., Palladino, D., Burtner, A., 2016a. Challenges for mapping cyanotoxin patterns from remote sensing of cyanobacteria. Harmful Algae 54, 160–173. https://doi.org/https://doi.org/10.1016/j.hal.2016.01.005

Stumpf, R.P., Johnson, L.T., Wynne, T.T., Baker, D.B., 2016b. Forecasting annual cyanobacterial bloom biomass to inform management decisions in Lake Erie. J. Great Lakes Res. 42, 1174–1183. https://doi.org/https://doi.org/10.1016/j.jglr.2016.08.006

Szlag, D.C., Sinclair, J.L., Southwell, B., Westrick, J.A., 2015. Cyanobacteria and cyanotoxins occurrence and removal from five high-risk conventional treatment drinking water plants. Toxins (Basel). 7, 2198–2220.

Taranu, Z.E., Gregory-Eaves, I., Leavitt, P.R., Bunting, L., Buchaca, T., Catalan, J., Domaizon, I., Guilizzoni, P., Lami, A., McGowan, S., 2015. Acceleration of cyanobacterial dominance in north temperate-subarctic lakes during the Anthropocene. Ecol. Lett. 18, 375–384.

The Novak Consulting Group, 2018. City of Salem Water Advisory After-Action Assessment.

Theil, H., 1992. A Rank-Invariant Method of Linear and Polynomial Regression Analysis, in: Raj, B., Koerts, J. (Eds.), Henri Theil's Contributions to Economics and Econometrics: Econometric Theory and Methodology. Springer Netherlands, Dordrecht, pp. 345–381. https://doi.org/10.1007/978-94-011-2546-8_20

Torchiano, M., 2020. effsize: Efficient Effect Size Computation. https://doi.org/10.5281/zenodo.1480624

U.S. EPA, 2020. State HABs Monitoring Programs and Resources [WWW Document]. URL https://www.epa.gov/cyanohabs/state-habs-monitoring-programs-and-resources

U.S. EPA, 2016a. Water treatment optimization for cyanotoxins.

U.S. EPA, 2016b. The Fourth Unregulated Contaminant Monitoring Rule (UCMR 4) General Information.

U.S. EPA, 2016c. The Fourth Unregulated Contaminant Monitoring Rule (UCMR 4) Cyanotoxins – Fact Sheet for Assessment Monitoring.

U.S. EPA, 2009. National lakes assessment: a collaborative survey of the nation's lakes.

Urquhart, E.A., Schaeffer, B.A., 2020. Envisat MERIS and Sentinel-3 OLCI satellite lake biophysical water quality flag dataset for the contiguous United States. Data Br. 104826. https://doi.org/https://doi.org/10.1016/j.dib.2019.104826

Urquhart, E.A., Schaeffer, B.A., Stumpf, R.P., Loftin, K.A., Werdell, P.J., 2017. A method for examining temporal changes in cyanobacterial harmful algal bloom spatial extent using satellite remote sensing. Harmful Algae 67, 144–152. https://doi.org/10.1016/J.HAL.2017.06.001

Üveges, V., Tapolczai, K., Krienitz, L., Padisák, J., 2012. Photosynthetic characteristics and physiological plasticity of an Aphanizomenon flos-aquae (Cyanobacteria, Nostocaceae) winter bloom in a deep oligo-mesotrophic lake (Lake Stechlin, Germany), in: Phytoplankton Responses to Human Impacts at Different Scales. Springer Netherlands, pp. 263–272. https://doi.org/10.1007/978-94-007-5790-5_20

Wasserstein, R.L., Schirm, A.L., Lazar, N.A., 2019. Moving to a World Beyond "p < 0.05." Am. Stat. 73, 1–19. https://doi.org/10.1080/00031305.2019.1583913

Wejnerowski, Ł., Rzymski, P., Kokociński, M., Meriluoto, J., 2018. The structure and toxicity of winter cyanobacterial bloom in a eutrophic lake of the temperate zone. Ecotoxicology 27, 752–760. https://doi.org/10.1007/s10646-018-1957-x

Wilcoxon, F., 1945. Individual Comparisons by Ranking Methods, Biometrics Bulletin.

Wilkinson, G.M., Carpenter, S.R., Cole, J.J., Pace, M.L., Batt, R.D., Buelo, C.D., Kurtzweil, J.T., 2018. Early warning signals precede cyanobacterial blooms in multiple whole-lake experiments. Ecol. Monogr. 88, 188–203.

Wynne, T., Stumpf, R., Tomlinson, M., Dyble, J., 2010. Characterizing a cyanobacterial bloom in Western Lake Erie using satellite imagery and meteorological data. Limnol. Oceanogr. 55, 2025–2036. https://doi.org/10.4319/lo.2010.55.5.2025

Wynne, T.T., Stumpf, R.P., Tomlinson, M.C., Warner, R.A., Tester, P.A., Dyble, J., Fahnenstiel, G.L., 2008. Relating spectral shape to cyanobacterial blooms in the Laurentian Great Lakes. Int. J. Remote Sens. 29, 3665–3672. https://doi.org/10.1080/01431160802007640

Wyoming DEQ, 2018a. Big Sandy Reservoir Harmful Cyanobacterial Investigation 2018.

Wyoming DEQ, 2018b. Eden Reservoir Harmful Cyanobacterial Investigation 2018.

Wyoming DEQ, 2018c. Pathfinder Reservoir Harmful Cyanobacterial Bloom Investigation 2018.

Zhang, F., Hu, C., Shum, C.K., Liang, S., Lee, J., 2017. Satellite Remote Sensing of Drinking Water Intakes in Lake Erie for Cyanobacteria Population Using Two MODIS-Based Indicators as a Potential Tool for Toxin Tracking. Front. Mar. Sci. 4, 124.

CHAPTER 4: PERFORMANCES ACROSS WORLDVIEW-2 AND RAPIDEYE FOR REPRODUCIBLE SEAGRASS MAPPING

Published in Remote Sensing of Environment December 2020
(https://doi.org/10.1016/j.rse.2020.112036)

Authors

Megan M. Coffer[1,2], Blake A. Schaeffer[3], Richard C. Zimmerman[4], Victoria Hill[4], Jiang Li[5], Kazi A. Islam[5], Peter J, Whitman[1]

Affiliations

[1]ORISE Fellow, U.S. Environmental Protection Agency, Office of Research and Development, National Exposure Research Laboratory, USA

[2]Center for Geospatial Analytics, North Carolina State University, Raleigh, NC, USA

[3]U.S. Environmental Protection Agency, Office of Research and Development, Durham, NC, USA

[4]Department of Ocean, Earth & Atmospheric Sciences, Old Dominion University, Norfolk, VA, USA

[5]Department of Electrical & Computer Engineering, Old Dominion University, Norfolk, VA, USA

Acknowledgements

The authors thank M. C. Lebrasse, D. Graybill, W. Salls, J. Darling, and P. Colarusso for their contributions in both method development and manuscript review. This work was supported by the NASA Ocean Biology and Biogeochemistry Program NRA #NNH16ZDA001N and augmented by the NASA Commercial Data Buy. Work was also supported by the U.S. EPA, and Oak Ridge Institute for Science and Technology (ORISE). Digital Globe imagery was made available through the U.S. Government NextView license. Planet's RapidEye imagery was made available through the NASA Commercial Data Buy. This article has been reviewed by the Center for Environmental Measurement and Modeling and approved for publication. Mention of trade names or commercial products does not constitute endorsement or recommendation for use by the U.S. Government. The views expressed in this article are those of the authors and do not necessarily reflect the views or policies of the U.S. EPA. Lastly, we thank three anonymous reviewers for their assistance in improving the structure and communication of the study.

Abstract

Satellite remote sensing offers an effective remedy to challenges in ground-based and aerial mapping that have previously impeded quantitative assessments of global seagrass extent. Commercial satellite platforms offer fine spatial resolution, an important consideration in patchy seagrass ecosystems. Currently, no consistent protocol exists for image processing of commercial data, limiting reproducibility and comparison across space and time. Additionally, the radiometric performance of commercial satellite sensors has not been assessed against the dark and variable targets characteristic of coastal waters. This study compared data products derived from two commercial satellites: DigitalGlobe's WorldView-2 and Planet's RapidEye. A single scene from each platform was obtained at St. Joseph Bay in Florida, USA, corresponding to a November 2010 field campaign. A reproducible processing regime was developed to transform imagery from basic products, as delivered from each company, into analysis-ready data usable for various scientific applications. Satellite-derived surface reflectances were compared against field measurements. WorldView-2 imagery exhibited high disagreement in the coastal blue and blue spectral bands, chronically overpredicting. RapidEye exhibited better agreement than WorldView-2, but overpredicted slightly across all spectral bands. A deep convolutional neural network was used to classify imagery into deep water, land, submerged sand, seagrass, and intertidal classes. Classification results were compared to seagrass maps derived from photointerpreted aerial imagery. This study offers the first radiometric assessment of WorldView-2 and RapidEye over a coastal system, revealing inherent calibration issues in shorter wavelengths of WorldView-2. Both platforms demonstrated as much as 97% agreement with aerial estimates, despite differing resolutions. Thus, calibration issues in WorldView-2 did not appear to interfere with classification accuracy, but could be problematic if estimating biomass. The image processing routine developed here offers a reproducible workflow for WorldView-2 and RapidEye imagery, which was tested in two additional coastal systems. This approach may become platform independent as more sensors become available.

Keywords Remote sensing, Atmospheric correction, WorldView-2, RapidEye, Seagrass, Image classification

1 Introduction

Seagrass meadows occupy less than 0.2% of the ocean floor, but store approximately 10% of the ocean's carbon per year (Duarte et al., 2013; Fourqurean et al., 2012). Despite their prominent role in the global carbon cycle, carbon storage in these ecosystems is poorly quantified, with estimates ranging from 4.2 to 19.9 Pg of total organic carbon currently stored in seagrass ecosystems (Fourqurean et al., 2012). This uncertainty results, to a large extent, from a poor understanding of global seagrass coverage, ranging between 150,000 and 4,320,000 km2 (Duarte, 2017). The 2016 Commission for Environmental Cooperation report concluded that seagrasses represent the greatest data gap in Blue Carbon habitat mapping, where Blue Carbon represents carbon captured by ocean and coastal sediments (CEC, 2016).

Seagrass extent has been poorly quantified largely due to logistical and labor challenges involved in aerial and ground-based efforts, including the high cost of comprehensive mapping (Björk et al., 2008; Dekker et al., 2006). In contrast, satellite remote sensing can offer an effective approach for mapping and monitoring seagrass in coastal ecosystems (Baumstark et al., 2013). Several classification techniques have been used for seagrass detection, including maximum likelihood, object based image analysis (OBIA), support vector machines, and random forests. These algorithms have been applied to a range of satellite platforms (Hill et al., 2014), with accuracies ranging from 73% to 85% (Traganos and Reinartz, 2017; Pasqualini et al., 2005; Pu et al., 2014; Pu and Bell, 2013; Meyer and Pu, 2012; Traganos and Reinartz, 2018).

The Landsat series, which provides imagery at 30 m spatial resolution in five visible to near infrared spectral bands (Dekker et al., 2005; Mumby et al., 1997; Ward et al., 2003; Hossain et al., 2015), and other moderate-scale sensors such as Sentinel-2A at 10 m spatial resolution (Fauzan et al., 2017; Thalib et al., 2018), have been used to monitor seagrass ecosystems. Commercial platforms such as RapidEye at 5 m (Traganos and Reinartz, 2018), PlanetScope at 3 m (Wicaksono and Lazuardi, 2018), Quickbird-2 at 2.4 m (Phinn et al., 2008a; Lyons et al., 2011), and WorldView-2 at 2 m (Baumstark et al., 2016; Roelfsema et al., 2014) offer finer spatial resolution, but have been included in fewer studies due to costs associated with the imagery. High spatial resolution (< 10 m) allows for improved seagrass biomass retrieval, productivity estimates, and patch size statistics (Hill et al., 2014).

Although commercial platforms have been successfully employed for seagrass delineation, previous studies have not presented a consistent nor transparent processing regime, limiting reproducibility. Atmospheric correction, for example, is an essential step for creating separability in spectra (Huang et al., 2016), required for both classification (Knudby and Nordlund, 2011) and comparison across space and time (Coppin et al., 2004). However, optimization of atmospheric correction parameters specific to commercial satellite platforms remains largely an ad hoc process, limited at least in part by the low signal to noise ratio of commercial platforms over dark pixels.

Moreover, radiometric performance of commercial imagery in coastal environments has not been quantitatively assessed. Analyzing agreement of radiometric measurements is important for increasing user confidence, determining appropriate applications, and to allow informed use of the imagery (Mélin et al., 2016). An understanding of radiometric performance is necessary for tasks such as merging different datasets (Pottier et al., 2006) and performing trend analyses (Vantrepotte and Mélin, 2011).

Machwitz et al. (2014) found RapidEye reflectance values to be higher than field observations in land-based applications. Less quantitative validation exists for WorldView-2 data. Looking into the literature of the radiometric performance of WorldView-2 in terrestrial systems, Latif et al. (2012) quantified disagreement between WorldView-2 reflectance measurements and field measurements of a forest habitat. The two datasets varied by about 5%, and reflectance measurements in shorter shorter wavelengths were higher in WorldView-2 imagery as compared to field observations and lower in longer wavelengths.

We used DigitalGlobe's WorldView-2 satellite platform, which collects imagery in eight multispectral bands at 2 m resolution, and Planet's RapidEye satellite constellation, which collects imagery in five multispectral bands at 6.5 m resolution. Here we report our efforts to:

1. Develop a reproducible workflow for processing commercial satellite imagery from DigitalGlobe's WorldView-2 satellite platform and Planet's RapidEye satellite constellation.
2. Evaluate and compare radiometric performance of each sensor by analyzing agreement between satellite-derived reflectance measurements and field-derived reflectance measurements.
3. Apply a deep learning approach presented in Islam et al. (2020) to estimate seagrass coverage and assess classification agreement with an aerial photointerpretation.

2 Data and methods

2.1. Study area

St. Joseph Bay is located along the Florida panhandle in the northern Gulf of Mexico (29.797°N, 85.353°W; **Figure 1**). Selection of St. Joseph Bay was motivated by the presence of existing field data and extensive familiarity with the site (i.e., Hill et al., 2014). St. Joseph Bay is approximately 24 km long and 10 km wide, opening in the north to the Gulf of Mexico. The Gulf County Canal flows into the northeast portion of the bay at the town of Port St. Joe. Water depth ranges up to 12 m at the center of the bay. At the southern end, an extensive shallow area less than 3 m deep occupies about a third of the entire bay (Hill et al., 2014).

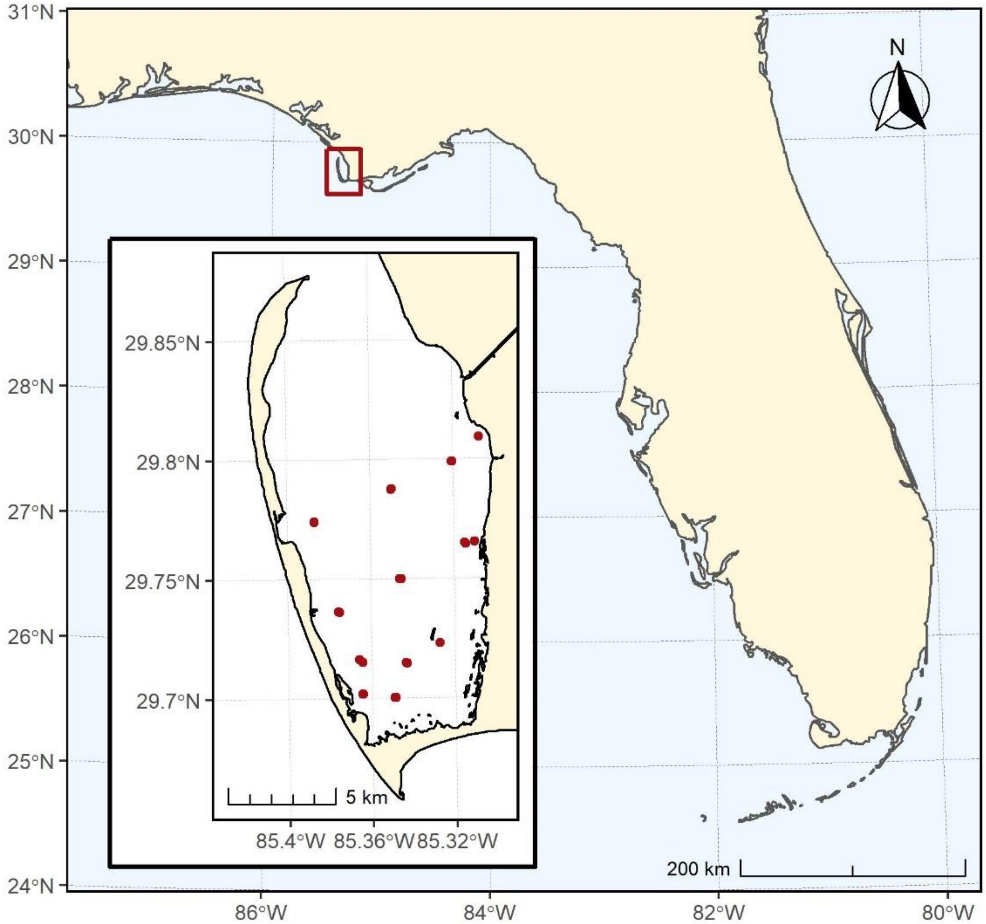

Figure 1. St. Joseph Bay is located along the Florida panhandle in the northern Gulf of Mexico (29.797°N, 85.353°W). Hyperspectral field measurements were taken at 24 locations throughout the bay (red points) on 2, 6, and 9 Nov 2010.

Waters in St. Joseph Bay are characterized by moderately high concentrations of phytoplankton, colored dissolved organic matter (CDOM), and suspended nonalgal particulate (detritus and sediment), creating a potentially challenging optical environment (Conmy et al., 2017). The seagrass within the bay is dominated by turtlegrass (*Thalassia testudinum*) which forms dense meadows at depths less than 2 m (Hill et al., 2014). Manateegrass (*Syringodium filiforme*), shoalgrass (*Halodule wrightii*), widgeongrass (*Ruppia maritima*), and stargrass (*Halophila* *engelmannii*) are also present in lower densities. Manateegrass can reach depths of up to 2 m while the other species tend to dominate at shallower depths.

2.2. Satellite data

Satellite data were obtained from two commercial platforms, WorldView-2 and RapidEye (**Table B1**). DigitalGlobe launched WorldView-2 in October 2009, offering multispectral data at a 1.84 m ground sample distance (GSD) at nadir. Basic level 1B data were obtained from DigitalGlobe's EnhancedView Web Hosting Service (evwhs.digitalglobe.com) at a spatial resolution of 2 m for 14 Nov 2010 (Maxar, 2019), which was the closest cloud-free overpass to field data collection.

RapidEye was a constellation of five satellite sensors launched in August 2008 and decomissioned in December 2019 (Planet Team, 2017). While new imagery will not be collected from the RapidEye constellation, over a decade of archived imagery exists and Planet has announced a plan to launch Super-Dove platforms with similar resolutions as RapidEye. Each Planet's RapidEye satellite offered multispectral data at a 6.5 m GSD at nadir. Basic level 1B data were obtained for the RapidEye-2 satellite through Planet Explorer (https://www.planet.com/explorer/) for 11 Nov 2010 (Planet Labs Inc, 2019), which, again, was the closest cloud-free overpass to field data collection. Off-nadir images were intentionally selected to avoid challenges presented with sunglint. View angles for the selected images ranged from 10° to 16°.

RapidEye offered five multispectral bands with four in the visible and one in the near infrared (NIR). WorldView-2 offers six bands in the visible, two in the NIR, and an order-of-magnitude finer spatial resolution than RapidEye (**Figure 2**, **Table 1**). The dynamic range, which describes the amount of information that can be measured within a pixel, was higher in RapidEye (12-bit) than WorldView-2 (11-bit). Signal to noise ratio (SNR) was computed following Dadon et al. (2011). WorldView-2 offered improved SNR compared to RapidEye in shorter wavelengths; RapidEye offered improved SNR compared to WorldView-2 in longer wavelengths (**Table 1**).

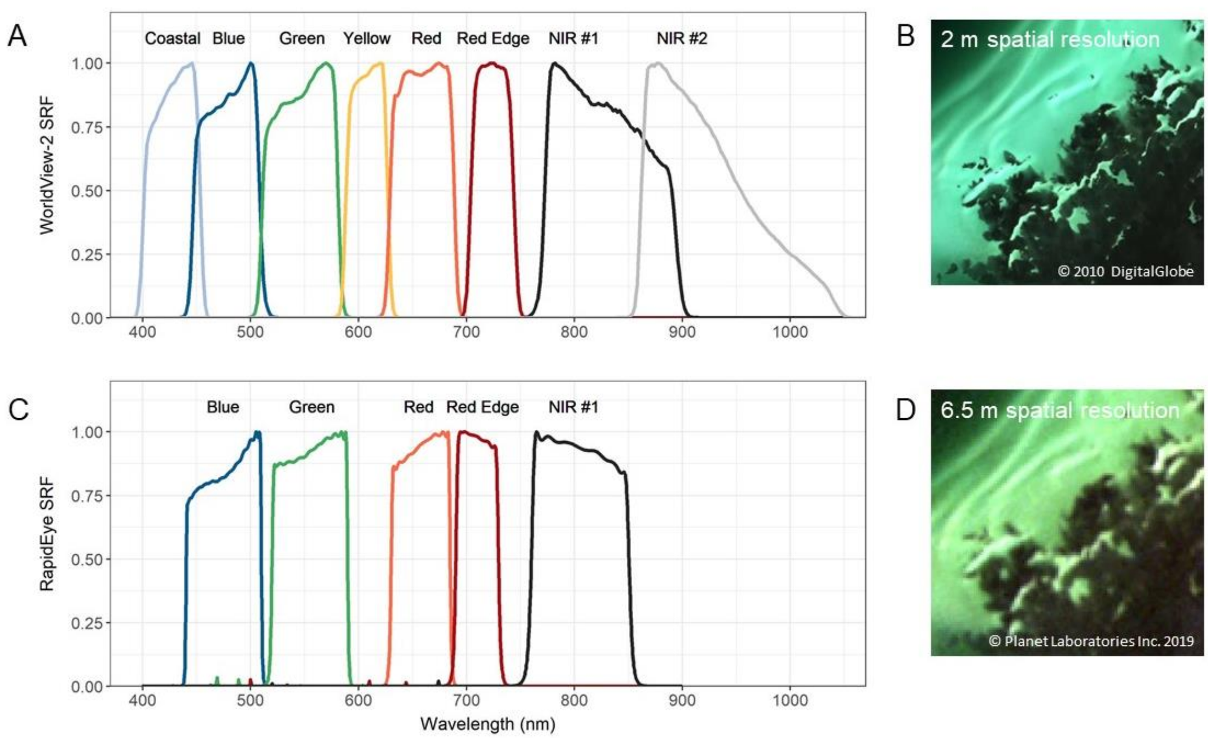

Figure 2. (A) Spectral response function (SRF) of visible and near infrared (NIR) channels for DigitalGlobe's WorldView-2 satellite and (B) a true color image of 2 m WorldView-2 data. (C) SRF of Planet's RapidEye satellite constellation and (D) a true color image of 6.5 m RapidEye data (copyright Planet Laboratories Inc. 2019 all rights reserved).

Table 1. Spectral characteristics of each sensor. FWHM represents the full width half maximum for each band. SNR indicates the signal to noise ratio computed across the scene following Dadon et al. (2011) as the ratio between the standard deviation and the mean of the satellite signal for each band, and excluded land pixels. The exclusion of land pixels is explained in Section 2.3.

Band	**WorldView-2**			**RapidEye**		
	FWHM	**Center**	**SNR**	**Range**	**Center**	**SNR**
Coastal	400–450	427.3	22.22			
Blue	450–510	477.9	7.40	440–510	475	3.10
Green	510–580	546.2	2.65	520–590	555	1.71
Yellow	585–625	607.8	1.64			
Red	630–690	658.8	1.41	630–685	657.5	1.17
Red edge	705–745	723.7	0.58	690–730	710	1.24
NIR #1	770–895	832.5	0.45	760–850	805	1.18
NIR #2	860–1040	908	0.57			

2.3. Data processing

WorldView-2 and RapidEye scenes were processed to produce orthorectified, radiometrically calibrated, and atmospherically corrected images from the Level 1B data products. The order of some steps is important (e.g., atmospheric correction must be applied after radiometric calibration), but the sequence of other steps is interchangeable. Each scene was delivered as multiple tiles. The WorldView-2 scene was divided into three tiles, and the RapidEye scene into two. Data processing was performed for each tile before being mosaicked into a single scene. Satellite data processing was performed in ENVI 8.7.0 and IDL 8.7.2 (Exelis Visual Information Solutions, Boulder, Colorado).

2.3.1. Radiometric calibration

The radiometric calibration values provided with WorldView-2 imagery were adjusted using updated vicarious calibration factors provided by Kuester (2017). Radiometric calibration required the adjusted and raw calibration coefficients for WorldView-2 and RapidEye, respectively. Next, all pixel values were divided by π to convert dimensionless reflectance values to remote sensing reflectance (R_{rs}) in units of inverse steradians (sr^{-1}).

2.3.2. Atmospheric correction

A dark object subtraction (DOS) approach was used to remove atmospheric contamination from the R_{rs} signal (Chavez, 1988). Three parameters can be optimized when performing DOS: the starting spectral band, the threshold at which pixels are considered to represent dark objects, and the value of the exponent used to correct shorter wavelengths. This study employed the red edge band as the starting spectral band, a threshold of the median of lowest 5% of the distribution of red edge pixel values, and a Rayleigh exponent of 4.75. NIR bands are commonly used to establish DOS adjustment values (Green et al., 2000); however, the signal to noise ratio of WorldView-2 and RapidEye were insufficient such that radiometrically calibrated values over the darkest water pixels in the image frequently yielded negative radiances in the NIR bands before atmospheric correction, preventing their use for DOS (**Table 1**).

Optimization of the reference contamination value and the exponent were explored by iterating through a range of values and noting the effect on the resulting spectra. Red edge distribution percentage medians ranging from 5% through 50% in increments of 5% were considered, while maintaining a constant Rayleigh exponent of 4.75. Rayleigh exponents ranging from 3.5 to 6.5 in increments of 0.25 were tested, while maintaining a constant red edge distribution percentage of 5%. Resulting spectra were visually compared against field observations.

A reproducible workflow was developed in an effort to reduce the arbitrary nature of selecting dark pixels used for DOS (**Figure 3**). A shapefile indicating the extent of estuaries along the coastline was used as an initial separation between land and water (Schaeffer and Myer, 2020), ensuring red edge anchor values were not selected from inland water pixels such as lakes and rivers. After spatial subsetting, some pixels along the shoreline remained. Therefore, a spectral threshold was applied. The normalized difference water index (NDWI) was computed (McFeeters, 1996), and pixel values flagged as water (i.e., NDWI value above zero) were retained for dark pixel consideration.

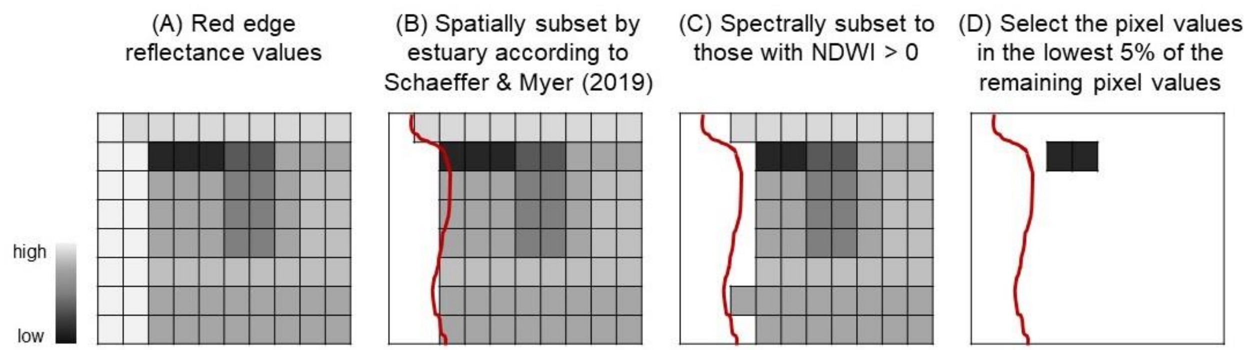

Figure 3. (A) Image showing the distribution of red edge R_{rs} values scaled from “low” to “high” across a hypothetical image. (B) Pixels retained after applying the estuary boundary of Schaeffer and Myer (2020). (C) Additional pixels removed with NDWI > 0. (D) Remaining pixels representing the lowest 5% of the R_{rs} values in the red edge band.

The median of red edge R_{rs} values was computed from those representing the darkest 5% of the distribution. We assumed half the red edge radiance represented atmospheric contamination, while the remainder represented true water-leaving radiances. This assumption was motivated by Vanhellemont and Ruddick (2014) in which a linear relationship between the two surrounding bands, red and NIR, was used to characterize atmospheric contamination in Landsat 8 imagery and was further established through a sensitivity analysis in which approximately half of the red edge signal generated retrievals that did not result in negative R_{rs} values, where negative R_{rs} indicate an atmospheric overcorrection. Determination of a red edge anchor value was repeated for all tiles within the scene, and the lowest of these values was used to compute the scattering factor for the entire scene. Red edge anchor values across tiles did not differ drastically, ranging from 0.000655 to 0.000657 for WorldView-2 and 0.00269 to 0.00279 for RapidEye. The scattering factor was computed as:

$$\sigma = \lambda_{red\ edge}^{4.75} \times \alpha_{red\ edge} \qquad \text{(Equation 1)}$$

Where σ is the scattering factor and α is the anchor value. The scattering factor was then applied to the wavelength of each band to compute the band-specific value subtracted from each pixel in each band, as:

$$\eta_{band} = \frac{\sigma}{\lambda_{band}^{4.75}} \qquad \text{(Equation 2)}$$

where η is the subtraction value. The resulting band-specific values of η were then subtracted from R_{rs} values in each band for all pixels in the scene.

2.3.3. RPC Orthorectification

Rational polynomial coefficient (RPC) orthorectification was applied to geometrically correct the image and remove distortions from image capture. The Global Multi-resolution Terrain Elevation Data 2010 (GMTED2010) dataset is provided with ENVI at a spatial resolution of 30 arc-seconds, and was used in the processing protocol presented here to ensure large-scale reproducibility and since there were no terrain-specific issues over water (Danielson and Gesch, 2011).

2.3.4. Mosaicking and resampling

Orthorectified tiles were then mosaicked into a single scene. In addition to the native resolution WorldView-2 and RapidEye scenes, a third raster was generated by resampling the 2 m WorldView-2 imagery via bilinear interpolation to match the 6.5 m spatial resolution of RapidEye. Comparing native resolution to downsampled WorldView-2 imagery revealed differences stemming from spatial resolution, given spectral resolution was the same. Comparing downsampled WorldView-2 imagery to native resolution RapidEye imagery revealed differences stemming from spectral resolutions given most other image parameters were held constant.

2.4. Field measurements of reflectance

Satellite estimates of atmospherically corrected R_{rs} were compared against hyperspectral reflectance measurements taken at 24 locations throughout the bay (Fig. 1). Statistical analyses were conducted in R Version 3.4.0 (R Core Team, 2017). Data were collected as described in Hill et al. (2014). Hyperspectral field measurements of R_{rs} were resampled to match the eight WorldView-2 and five RapidEye spectral bands by taking the mean of the hyperspectral reflectance values within the FWHM for each band. For each of the 24 observations, field measured R_{rs} was compared to satellite derived R_{rs} using the mean absolute deviation (MAD) and associated bias.

2.5. Classification of seagrass extent

A deep convolutional neural network (DCNN) developed by Islam et al. (2020) was used to classify image pixels into five classes: deep water, land, submerged sand, seagrass, and intertidal. Intertidal represents a region of filamentous red algae and microbial films, but not seagrass (Hill et al., 2014), along the land-water interface that would be submerged during high tide and exposed during low tide. Characterization of an intertidal region can be important for time series analyses in which different tidal stages are represented.

A DCNN was chosen as it achieves high accuracies with less computational complexity compared to other approaches (Islam et al., 2018, Islam et al., 2020). The DCNN model was developed with the Keras package in Python 3.5 (Python Core Team, 2015; Chollet, 2015). A DCNN model requires known input classes for training, which are provided through spectral information contained in regions of interest (ROIs). ROIs were generated across the image based on a combination of local knowledge, expected spectral response, and visual confirmation, with three polygons representing each of the five classes (**Figure 4**). The same ROIs were used for both WorldView-2 and RapidEye, ensuring differences in classification results between the two sensors were not due to differences in ROIs.

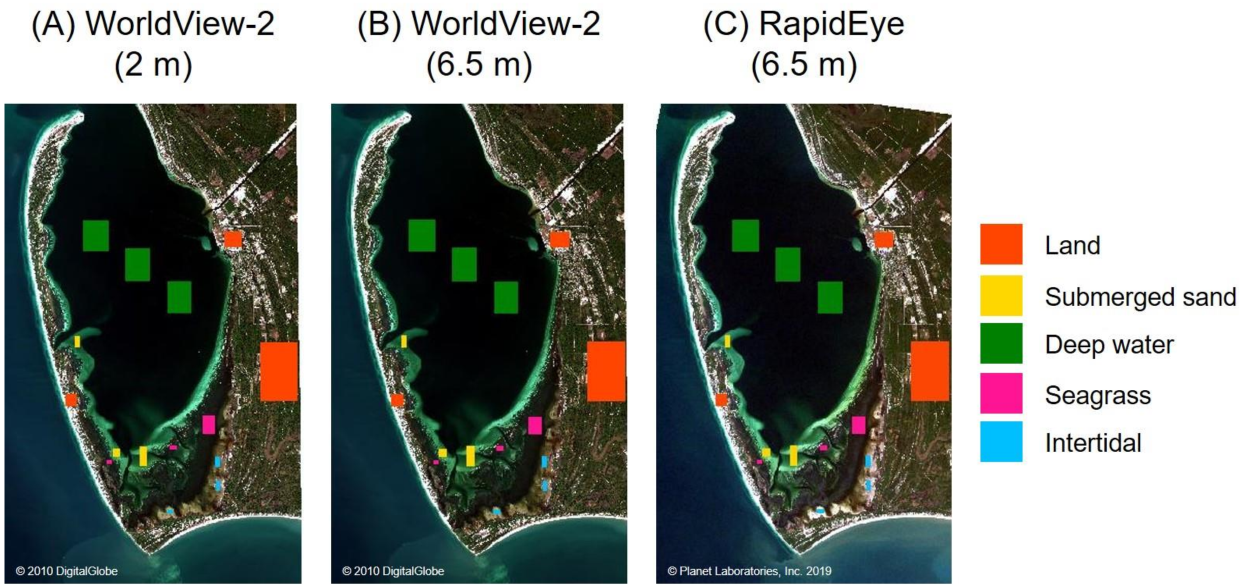

Figure 4. Regions of interest (ROIs) for each of the five classes overlaid on (A) native resolution WorldView-2 imagery, (B) downsampled WorldView-2 imagery, and (C) native resolution RapidEye imagery. ROIs were generated based on a combination of local knowledge provided by coauthors Zimmerman and Hill, expected spectral response, and visual confirmation.

We used an input patch size of 3 × 3 to extract the training samples from the selected ROIs. A sequential model, or linear stack, of six hidden layers was applied. The first layer was a convolutional layer consisting of 32 filters with a kernal size of 1 × 1 followed by a rectified linear activation function. Next a dropout layer randomly set 1% of the outputs from the first layer to zero. The second convolutional layer consisted of 16 filters with a kernal size of 3 × 3, again, followed by a rectified linear activation function. Then, another dropout layer with a dropout rate of 1% was added before flattening the model. Finally, a dense layer with a SoftMax activation function was used to compute pixel-based probabilities for each class (Bishop, 2006). This DCNN model was trained for 500 epochs, where an epoch represents the point at which all training data have been processed one time, using a batch size of 256. More information about the model can be found in **Text B1**.

2.6. Aerial estimates of seagrass extent

Seagrass pixels identified in the satellite imagery were compared to a shapefile obtained from the Florida Fish & Wildlife Conservation Commission (FL FWC) representing the distribution of seagrass beds in St. Joseph Bay derived from aerial photography. Aerial photographic images were interpreted by Quantum Spatial (2010, formerly Photo Science, Inc.) based on October 2010 natural color aerial photography acquired by the Florida Department of Transportation (Statistics Canada, 2008; Great Britain, 2009). Images were taken at high tide and only visible features were mapped.

FL FWC classified features into tidal flats, bays & estuaries, continuous seagrass, patchy seagrass, and unclassified from the aerial imagery. Descriptions of these classes were not available; thus, the ROIs chosen here were based on those presented in Islam et al. (2020) rather than attempting to match the classes presented in the FL FWC dataset. Additionally, the distinction between patchy and continuous seagrass is described as a perceived texture difference rather than percent cover; therefore, continuous and patchy seagrass were combined into a single seagrass class. FL FWC warns that the accuracy of this dataset was not verified. Typically, state programs strive to achieve a 10% mark for ground verification. Thus, this analysis assesses agreement among three remote sensing datasets, none of which have been verified through on the ground measurements: two datasets using a deep learning classifier on satellite imagery, the third using human photointerpretation of aerial imagery.

The aerial shapefile was subset to include just St. Joseph Bay and rasterized to match the spatial resolution of each satellite sensor. Before computing statistics, pixels classified in the satellite imagery as intertidal were discarded in both satellite and aerial estimates to account for differences in tidal heights between each dataset. An agreement matrix was developed for seagrass presence and seagrass absence, and agreement between aerial imagery and each satellite platform was assessed according to Congalton (1991) via the carot package in R (Kuhn et al., 2020).

Agreement matrices compare, on a class-by-class basis, the relationship between reference data (in this case, aerial imagery) and the corresponding classification results from analysis of the satellite images. Errors of ommission occur when a feature is incorrectly left out of the category being evaluated, i.e., a false negative. Errors of commission occur when a feature is incorrectly included in the category being evaluated, i.e., a false positive. Overall accuracy was computed as the number of pixels labeled as the same class in aerial and satellite imagery normalized to the total number of pixels in the scene.

The Kappa coefficient indicates how well the resulting classification performs compared to a random classification (Cohen, 1960; Goodman and Kruskal, 1954). It is represented as a ratio between -1 and 1 with higher Kappa coefficients indicating higher agreement between classification approaches. Difference maps were generated using the ArcGIS Image Analysis window to visualize areas in which satellite and aerial classifications differed (ESRI, 2016).

3. Results and discussion

3.1. Atmospheric correction

3.1.1. Optimizing DOS parameters

Adjustment of the red edge distribution percentage had a smaller effect on reflectance values than adjustment of the Rayleigh exponent, as shown for a single field location characterized by submerged sand (**Figure 5**). In WorldView-2 imagery, adjusting the red edge distribution percentage did little to change the resulting reflectance values, meaning distribution percentages ranging between 5% and 50% produced similar results. This same range of red edge distribution values applied to RapidEye data yielded a larger range of reflectance values, but the spectral shapes of corrected imagery still mimicked that of field observations.

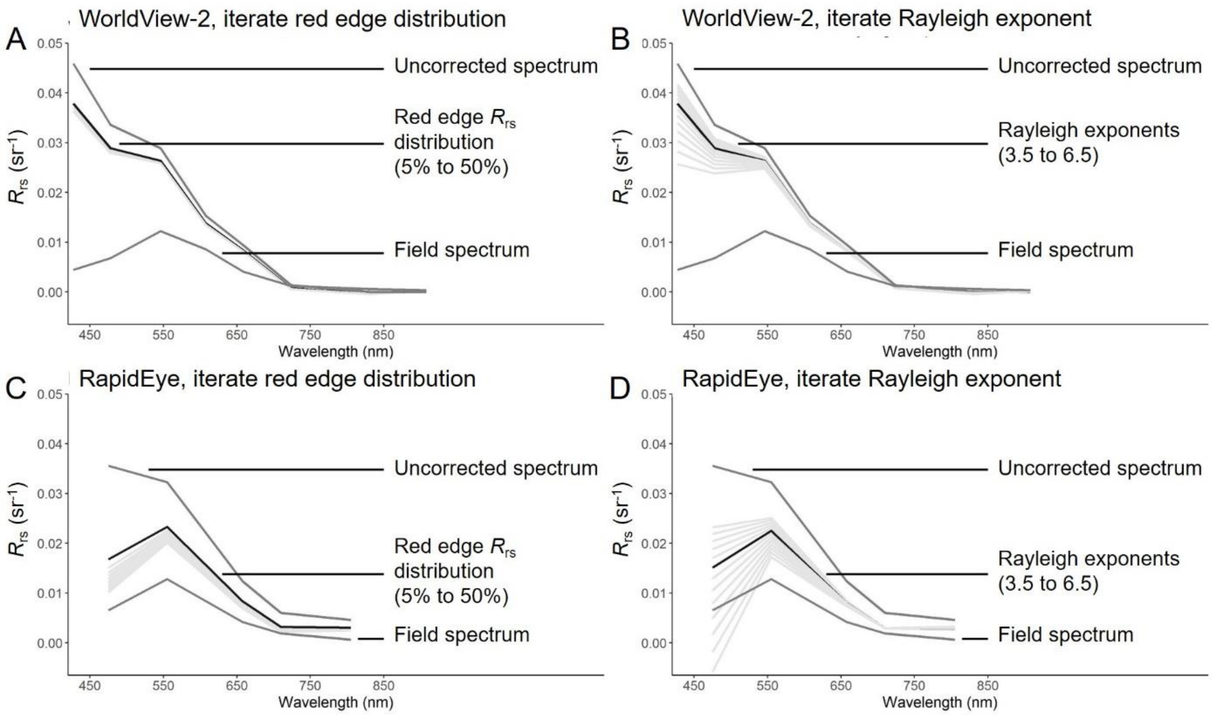

Figure 5. Example of the effect of red edge distribution percentage and Rayleigh exponent on the atmospherically corrected R_{rs} spectrum for a single pixel representing optically shallow sand. (A) WorldView-2 uncorrected spectra and field spectra compared against a DOS regime considering red edge distribution percentages between 5% and 50% in increments of 5%, while maintaining a constant Rayleigh exponent of 4.75. (B) WorldView-2 uncorrected spectra and field spectra compared against a DOS regime considering Rayleigh exponents between 3.5 and 6.5 in increments of 0.25, while maintaining a constant red edge distribution percentage of 5%. (C) Same as (A), but for RapidEye. (D) Same as (B), but for RapidEye.

When iterating the Rayleigh exponent, similarity in spectral shape between corrected satellite-derived reflectance and field reflectance was sought. A Rayleigh exponent of 4.75 provided necessary correction in shorter wavelengths while preserving non-negative values (i.e., avoiding over-correction) across the entire spectrum. In WorldView-2 imagery, a Rayleigh exponent of 6.5 was still incapable of producing reasonable reflectance values in the coastal blue and blue spectral bands. In RapidEye imagery, higher Rayleigh exponents resulted in negative reflectance values in shorter wavelengths.

Even with more stringent atmospheric correction through an increased red edge distribution and Rayleigh exponent, comparatively high reflectance values in the coastal blue and blue spectral bands of WorldView-2 could not be lowered sufficiently to match the in situ measurements of R_{rs}. Although the present study only examined one WorldView-2 scene, manual inspection of multiple WorldView-2 scenes indicates this offset is common across this platform, suggesting that radiometrically corrected values in the coastal blue and blue spectral bands are much higher than they should be over these relatively dark water targets.

A primary component of standardizing data processing for commercial imagery was the development of an atmospheric correction approach that did not require user-supplied values on a scene-by-scene basis, which is a known limitation of DOS. In addition to creating spectral separability necessary for classification, atmospheric correction is considered a requirement for change detection applications (Coppin et al., 2004), such as assessing temporal changes in seagrass extent. This effort begins to assess the applicability of a standardized processing regime, and it is encouraging that both images settled on the same parameters.

St. Joseph Bay is characterized by a large central basin of optically deep water, which explains similar reflectance values while iterating through various red edge distributions. In coastal areas characterized by waters with a more diverse distribution of optical properties, the percentage of the red edge reflectance values used to characterize dark water will certainly have a larger influence on the resulting spectra. In such environments, using a higher percentage of the red edge reflectance values will likely result in over-correction, yielding negative reflectance values in shorter wavelengths. Therefore, it is likely that a conservative threshold of 5% will allow proper atmospheric characterization even in scenes with a small area of optically deep water, but future efforts should focus on spatial and temporal applicability.

Preserving the minimum red edge anchor value for all tiles within the scene further increases confidence that the red edge anchor is representative of deep water pixels, increasing the likelihood that the atmospheric correction is an accurate representation of atmospheric contamination. If a minimum of one tile within the scene is characterized by optically deep water in at least 5% of the surface area, this DOS approach should yield a sufficient atmospheric correction. A division factor of two was used to capture atmospheric contamination while maintaining true water-leaving radiance in the red edge spectral band.

Relatively high Rayleigh exponents have been found to be more appropriate in clear conditions, whereas relatively low Rayleigh exponents are more appropriate in hazy conditions (Curcio, 1961; Slater et al., 1983; Chavez, 1988). This is because in clear conditions, shorter wavelengths are scattered more relative to longer wavelengths while in hazy conditions, scattering across all wavelengths is more equal. Thus, the focus of DOS in clearer conditions is to decrease reflectance in shorter wavelengths, thereby adjusting the spectral shape. In hazier conditions, the focus of DOS is to decrease reflectance across the entire spectrum while, more or less, preserving the spectral shape. Both scenes considered in this study represent visibly clear conditions, therefore a high Rayleigh exponent – as opposed to the idealized value of 4 – to represent the relative scattering model for this DOS approach is reasonable. Additionally, given that clear, cloud-free scenes are desired when extracting information at the surface, a Rayleigh exponent of 4.75 will likely be appropriate across a range of satellite scenes.

3.1.2. Atmospheric correction in the literature

Other automated atmospheric correction regimes have been applied to satellite remote sensing imagery, including ENVI's Fast Line-of-Sight Atmospheric Analysis of Hypercubes (FLAASH) model (Kovacs et al., 2018; Tamondong et al., 2013; Roelfsema et al., 2014; Traganos and Reinartz, 2018; Pu et al., 2014). However, FLAASH has been found to provide poorer results than those derived with DOS (Collin and Hench, 2012; Wicaksono and Hafizt, 2018).

DOS has successfully been applied to satellite imagery from a variety of platforms for seagrass detection (Hossain et al., 2015; Fauzan et al., 2017; Thalib et al., 2018; Wicaksono and Lazuardi, 2018). Despite its employment in commercial satellite processing, an investigation into its unbiased optimization has not been performed until now. Many studies apply atmospheric correction to a single scene, but the approach presented here to identify the darkest pixels in a scene can reduce bias requiring little, if any, manual intervention to the current workflow. The presented workflow could also be modified for sensors or scenes containing NIR values with better SNR. Employing NIR channels may result in an improved atmospheric correction given no assumptions need to be made regarding the actual versus perceived atmospheric contributions to the NIR reflectance values.

3.2. Deviation and bias in satellite-derived reflectance

RapidEye overpredicted reflectance values compared to field measurements for all spectral bands, but only slightly, while WorldView-2 overpredicted in shorter wavelengths (coastal blue through red) and underpredicted in longer wavelengths (**Figure 6**, **Table B2**). MAD and bias associated with the coastal blue and blue spectral bands of WorldView-2 was nearly 0.03 and 0.025, respectively, while results for the remaining bands fell below 0.015.

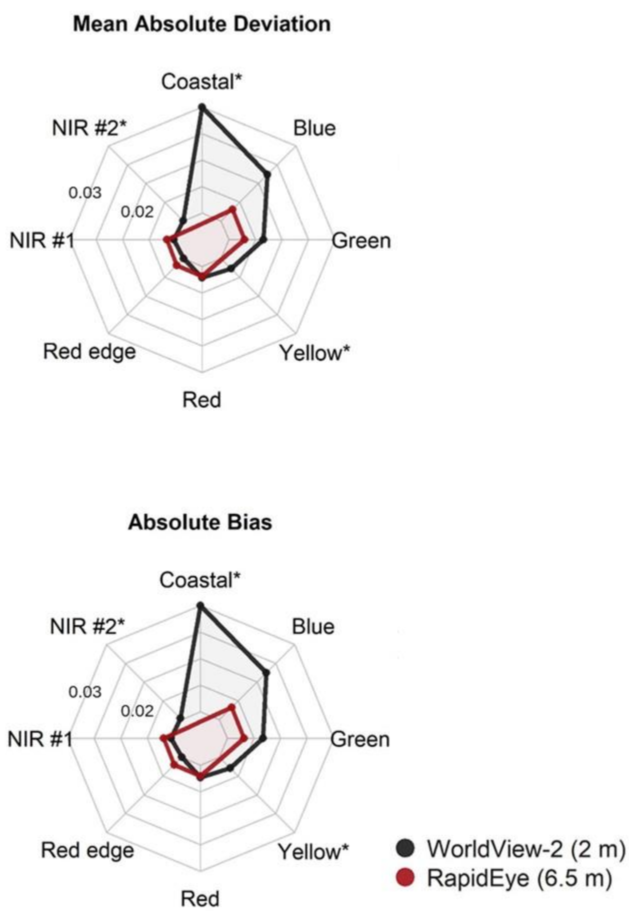

Figure 6. Radar plots indicating the average mean absolute deviation and mean absolute bias across 24 field sites throughout St. Joseph Bay. Asterisks indicate the wavelengths at which RapidEye does not collect data; therefore, RapidEye statistics were not computed for these bands.

Higher reflectance values in RapidEye imagery compared to field observations is consistent with previous studies in terrestrial ecosystems (Machwitz et al., 2014; Chander et al., 2013), and offset between WorldView-2 data and field observations is also supported (Latif et al., 2012). However, previous studies have not assessed radiometric performance over lower-reflectance aquatic environments. Difficulties in the radiometric correction are likely the reason for high reflectance values in shorter wavelengths of WorldView-2 imagery. Updated calibration factors presented in Kuester (2017) likely do not capture sensor drift, meaning updated values do not represent accurate correction factors for the 2010 image presented here. Additionally, these values should be revisited annually, but more recent correction values were not available.

While MAD and bias provide a comparison of sensor performance, a primary objective of atmospheric correction is to create realistic and separable spectral shapes for each class. Therefore, while the magnitude of MAD is a valid measure of sensor performance, a consistent MAD is more relevant for classification. Deviation associated with RapidEye was more consistent over its spectral bands than WorldView-2, suggesting that, although there was an offset, the spectral shapes of RapidEye data were more similar to those of field observations.

The temporal offset between field measurements and satellite overpass ranged from 5 to 12 days for WorldView-2 and 2 to 9 days for RapidEye. Deviation and bias for observations collected on 2 Nov 2010 (n = 2) were nearly double those of observations collected on 6 Nov 2010 (n = 11) or 9 Nov 2010 (n = 11; **Table B3**). Field observations taken on 9 Nov 2010 and early observations taken on 6 Nov 2010 coincided with the tidal stage at which satellite overpass occurred for both WorldView-2 and RapidEye (**Figure 7**). Tide predictions were obtained from the NOAA Tides & Currents database (https://tidesandcurrents.noaa.gov/). The tidal heights during field data collected on 2 Nov 2010 and later observations taken on 6 Nov 2010, however, was much lower.

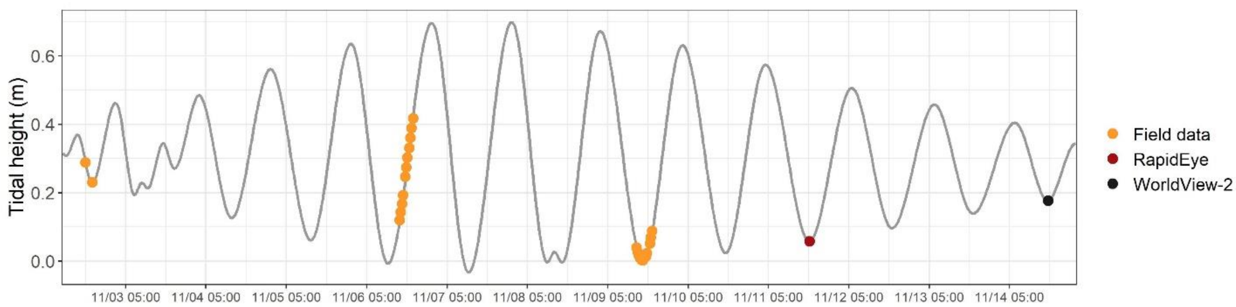

Figure 7. Predicted tidal height at Port St. Joe, FL obtained from the NOAA Tides & Currents database (https://tidesandcurrents.noaa.gov/). Acquisition times of field data are shown in orange, overpass time of RapidEye is shown in red, and overpass time of WorldView-2 is shown in black.

3.3. Agreement between satellite and aerial classifications

3.3.1. Regions of interest

Reflectance within ROIs varied between WorldView-2 and RapidEye (**Figure 8**). The intertidal class, for example, was characterized by much higher spectral signatures for RapidEye compared to WorldView-2, nearly resembling a land signature. Because of the tidal stage (**Figure 7**), deeper water at the time of image acquisition produced lower values in the WorldView-2 image relative to RapidEye.

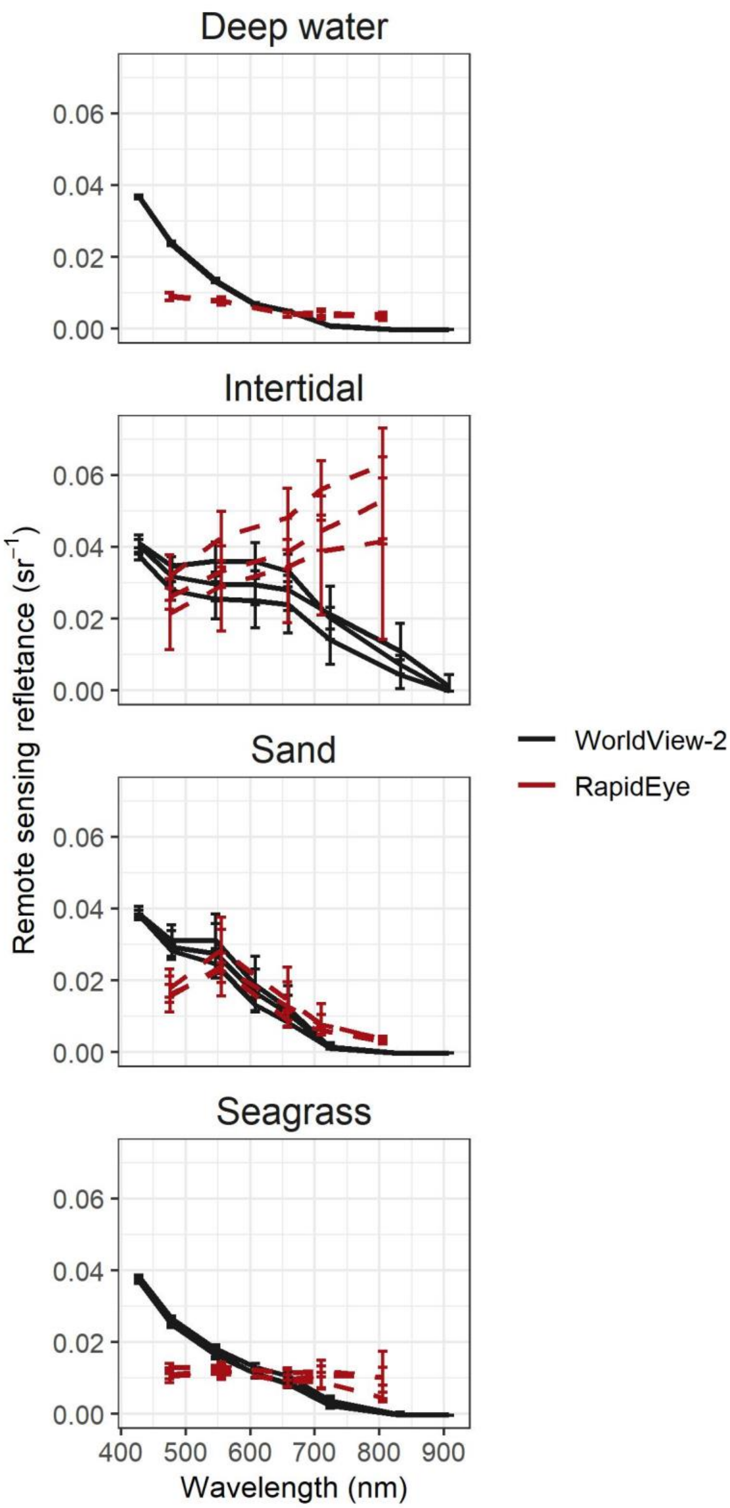

Figure 8. The 5th, 50th, and 95th percentile of the R_{rs} distribution for each region of interest (ROI) and sensor. Three ROIs were generated for land as well, but their spectra were excluded from this figure.

Reflectance values within RapidEye ROIs also demonstrated increased variability compared to WorldView-2, as shown through a larger spread between the 5th and 95th percentiles across nearly all classes. Additionally, chronically high reflectance values associated with coastal blue and blue spectral bands of WorldView-2 imagery was evident, particularly in the submerged sand spectra; RapidEye and WorldView-2 had high agreement in the green through NIR bands, but diverged in the shorter wavelengths as RapidEye followed a more expected spectral shape, decreasing in reflectance values, and WorldView-2 increased in reflectance values.

3.3.2. Classification results

Classification results were visually similar across all three datasets throughout much of St. Joseph Bay. However there were clear differences for each sensor compared to aerial photointerpretation (**Figure 9**, **Table B4**). Notably, the DCNN classified large areas of intertidal for both satellite platforms that were manually classified as seagrass from the aerial imagery. Although tidal height differed between aerial imagery acquisition and satellite overpass, Hill et al. (2014) reported much of the intertidal region to be colonized by filamentous red algae and microbial films, not seagrass. DCNN results also indicated higher coverage area of submerged sand, much of which was designated as deep water in the photointerpreted aerial imagery. Deeper water at the time of the aerial image acquisition likely explains the under-reporting of optically shallow water consisting of unvegetated sand.

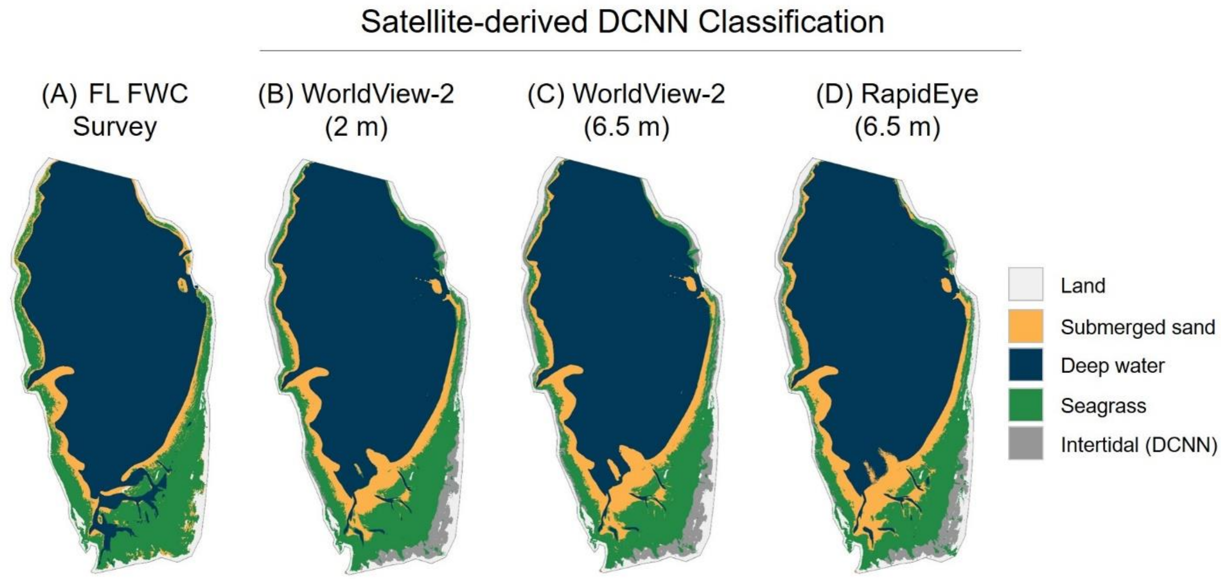

Figure 9. Classification results from Florida Fish & Wildlife Conservation Commission (FL FWC) and satellite data from native resolution WorldView-2 imagery, downsampled WorldView-2 imagery, and native resolution RapidEye imagery. FL FWC data was based on photointerpreted aerial imagery collected at high tide in October 2010. WorldView-2 and RapidEye imagery were obtained during low tide in November 2010 (WorldView-2 tidal height 0.2 m; RapidEye tidal height 0.06 m).

Quantitative assessment indicated that both satellite platforms were well-suited for seagrass detection, with overall accuracy above 96% (**Table 2**, **Table B5**). The Kappa coefficient (around 0.87) was also similar among the three images. Kappa coefficients between 0.80 and 0.90 are considered strong with 64–81% of data being reliable (McHugh, 2012). Thus, the higher disagreement between WorldView-2 and field-measured reflectance values did not appear to affect the performance of the image classification, although poor agreement could be problematic if using the imagery for pure radiometric values or atmospherically corrected reflectance values. For example, derived products such as density estimation require low disagreement (Hill et al., 2014).

Table 2. Agreement between machine learning classification of satellite imagery and photointerpretation of aerial imagery for seagrass presence and absence. Agreement was quantified through errors of ommission, errors of comission, overall accuracy, and the Kappa coefficient. Areas classified as intertidal by the DCNN were removed before computing agreement statistics to correct for differences in tidal height at time of data collection.

	Errors of omission		**Errors of commission**		**Overall accuracy**	**Kappa**
	Present	**Absent**	**Present**	**Absent**		
WorldView-2 (2m)	6%	3%	14%	1%	97%	0.88
WorldView-2 (6.5 m)	9%	2%	12%	2%	97%	0.88
RapidEye (6.5 m)	14%	2%	9%	3%	96%	0.86

Visibly identifiable seagrass pixels were misclassified by both WorldView-2 and RapidEye as sand along the fringes of seagrass before transitioning to submerged sand (**Figure 10**). RapidEye captured these areas with less accuracy than WorldView-2 as shown by large areas of orange along the the transition zone in the western portion of St. Joseph Bay. Poor capture in this area is likely due to the patchy nature of these regions, which can be problematic for classification in both satellite imagery (Knudby and Nordlund, 2011; Phinn et al., 2008b; Green et al., 1996; Baumstark et al., 2016; Pu et al., 2014; Pu and Bell, 2013) and photointerpretation (McKenzie et al., 2001; Meehan et al., 2005).

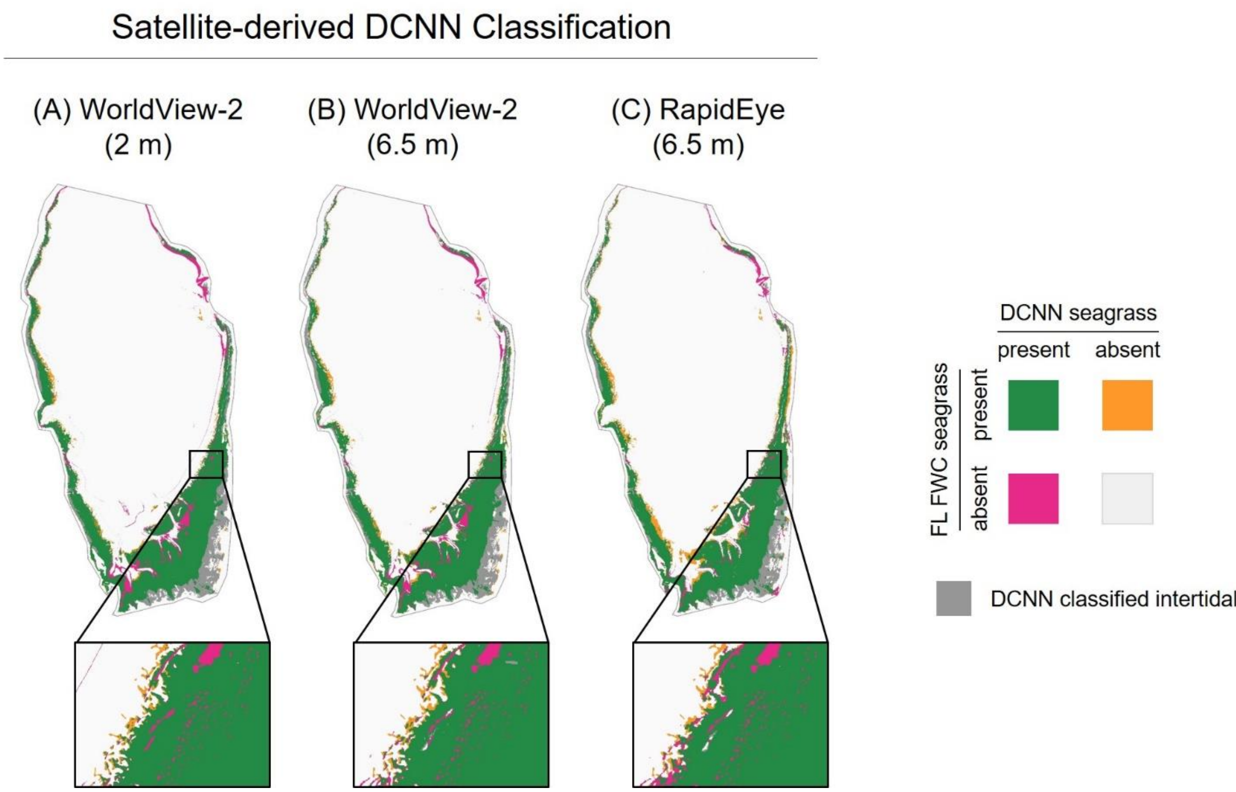

Figure 10. Difference maps illustrating areas classified through satellite imagery as seagrass present but classified through aerial imagery as seagrass absent (shaded in magenta) and areas classified through satellite imagery as seagrass absent but classified through aerial imagery as seagrass present (shaded in orange). Insets (black box) illustrate a portion of the classification difference to demonstrate performance differences along the transition from seagrass to another class.

Differences between satellite and aerial classifications along the transition from submerged sand to deep water were apparent in native resolution WorldView-2 imagery. A faint magenta line is visible along this transition zone (**Figure 10**), likely indicative of misclassification by the DCNN algorithm. Coarser spatial resolution could explain the absence of this artifact in both downsampled WorldView-2 imagery and RapidEye imagery.

WorldView-2 appears to overclassify seagrass in the southern portion of the bay compared to both the aerial photointerpretation and the RapidEye classification. Many of the inlets FL FWC labeled as either submerged sand or deep water are classified as seagrass in both the native resolution and resampled WorldView-2 imagery. Additionally, across all platforms, it appears that many smaller patches of submerged sand embedded in the seagrass beds were misclassified as seagrass. These misclassifications are likely because the spectra appear dark green to the satellite sensor since they were in relatively deep water. A spectral linear unmixing approach could offer insight into subpixel composition, allowing for improved habitat characterization in patchy environments.

The area surrounding the Gulf County Canal creates an artifact in the DCNN classification. All three scenes misidentify seagrass in this area of high CDOM discharge from the canal due to similar spectral shapes. In a spectrally similar environment, image classification approaches can fail to discern different cover types accurately (Knudby and Nordlund, 2011). The inclusion of a CDOM class could improve the classification in the future.

Agreement matrices could not be generated to compare satellite classifications to aerial photointerpretation across all classes because class labels differed between the two datasets. Instead, an agreement matrix was generated to compare classification results for deep water, land, submerged sand, seagrass, and intertidal between resampled WorldView-2 imagery with native resolution RapidEye imagery (**Table B6**).

Previous studies have found classification improvements through further image processing, particularly the application of a water column correction (Pu et al., 2014). However, in our system this correction was unnecessary to achieve sufficient spectral separability between seagrass and other classes. Additionally, none of the images considered were affected by sunglint which could present difficulties in both the proposed processing regime and the classification algorithm. Unmixing-based denoising has also improved accuracy assessments of remotely sensed seagrass (Traganos et al., 2017). Results presented here report merely on the presence or absence of seagrass. Satellite imagery has been used to report on percent cover of seagrass using a five class classification scheme of submerged aquatic vegetation (Pu and Bell, 2013; Pu et al., 2012; Roelfsema et al., 2009). Such an approach could improve classification along the transition from seagrass to another class, but ground measurements are needed to properly assess agreement.

3.3.3. Applicability across other systems

The processing protocol presented here and classification algorithm introduced in Islam et al. (2020) were used in three additional scenarios to test applicability across other systems (**Figure 11**). Because of the decomissioning of RapidEye in December 2019, only WorldView scenes were considered here, including imagery from both WorldView-2 and WorldView-3. Scenes at St. Joseph Bay, Tampa Bay, and St. George Sound were considered for the years 2010, 2016, and 2014, respectively. Tampa Bay and St. George Sound both represent similar systems to St. Joseph Bay. Tampa Bay is located along Florida's Gulf coast and St. George Sound is located along the Florida panhandle just east of St. Joseph Bay.

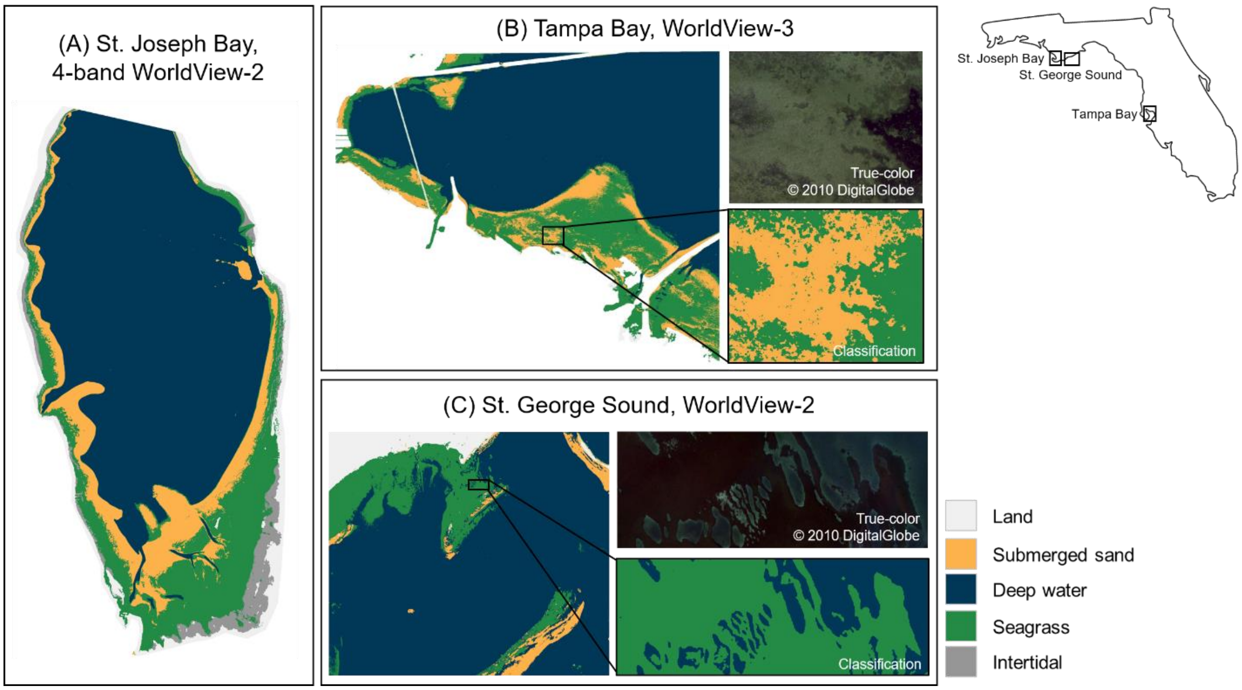

Figure 11. Classification results for (A) the same WorldView-2 scene used above, but using only the blue, green, red, and NIR #1 spectral bands, (B) a WorldView-3 scene from Tampa Bay, FL, USA from 1 Mar 2016 including a subset of the classification compared to the true-color imagery, and (C) a WorldView-2 scene from St. George Sound, FL, USA from 27 Apr 2014 including a subset of the classification compared to the true-color imagery.

First, the WorldView-2 scene presented earlier in the manuscript was considered, but using only the blue, green, red, and NIR #1 bands to mirror the spectral characteristics of other commercial platforms. Results were compared to photointerpreted aerial imagery and continued to demonstrate strong agreement (**Table B7**). Next, a WorldView-3 scene collected over Tampa Bay on 1 Mar 2016 was processed and classified using the methods presented here. Visual inspection of the results are promising, with the DCNN algorithm able to identify the patchy nature of seagrass in this system. A WorldView-2 scene collected over St. George Sound on 27 Apr 2014 also demonstrated agreement through visual inspection.

Results at Tampa Bay and St. George Sound were not quantitatively assessed for agreement with seagrass coverage maps for two reasons. First, the DCNN algorithm has already been demonstrated across sites (Islam et al., 2020). The focus of this study was instead to develop a reproducible processing regime for commercial satellite imagery, which can be demonstrated through successful creation of separable spectra required for an accurate classification. Second, the quality of photointerpretation results can vary drastically across regions. Visual comparison of true-color imagery against seagrass shapefiles at Tampa Bay, for example, revealed an important limitation of human drawn maps: areas of patchy seagrass are often aggregated into a single polygon, whereas a pixel-based approach such as a DCNN can provide more detailed estimates of seagrass coverage. Thus, using more generalized seagrass shapefiles can artificially reduce the agreement of the satellite classification as neither dataset conveys a validated representation of true seagrass coverage.

Although archives of WorldView-2 and RapidEye imagery exist, Schaeffer et al. (2013) found that mission continuity is critical for end-users. Several current satellite missions, including Airbus Defense and Space's SPOT-6 and -7 constellation and DigitalGlobe's GeoEye-1 satellite, are potentially well-suited for coastal seagrass detection, but each of these platforms offer only 4 multispectral bands: blue, green, red, and NIR. Results presented here demonstrate promise that the proposed methods are reproducible and potentially could move toward sensor independence, but additional testing across a larger range of images collected across space and time is needed. Additionally, more detailed field data would be required to quantitatively validate the performance of the DCNN at other locations.

3.3.4. The use of photointerpretation as reference data

Many studies assess the accuracy of remote sensing classifications by comparing results to photointerpretation, assuming photointerpretation results are correct. However, this assumption rarely holds and can result in a biased evaluation of remote sensing products (Congalton, 1991). Error associated with reference data is seldom known and, thus, impossible to consider when assessing classification accuracy. Moreover, while they did not offer an alternative, Rutchey and Vilchek (1999) cautioned against quantitative comparisons between aerial photointerpretation and satellite classification, noting the two approaches rely on very different mechanisms for classifying ground cover data. This is a gap that must be closed in order to transition from human to automated interpretation of remotely sensed imagery.

McKenzie et al. (2001) noted a particular area of error along the boundary of seagrass beds, which was an area of disagreement between the satellite and aerial imagery. The authors suggested these regions be assigned a quality flag to reflect lower confidence associated with human error. Moreover, findings from Meehan et al. (2005) argue that photointerpretation methods can overestimate seagrass area by amalgamating disjunct seagrass patches into continuous meadows. Edwards and Lowell (1996) and Thierry and Lowell (2001) proposed a 'fuzzy boundary' concept, where transition zones from one class to another were labeled or interpolated to indicate decreased confidence. These suggestions were not adopted in the FL FWC data, although such an approach could help quantify uncertainty in aerial estimates.

To our knowledge, no comprehensive study exists to assess the human error rates associated with image classification in aquatic systems. One study assessed the overall accuracy of a single photointerpretation in a wetland ecosystem, finding a 95% agreement with 34 field survey sites (Rutchey and Vilchek, 1999). While not explicitly quantified, Edwards and Lowell (1996) found texture differences and the presence of straight versus curved lines to influence photointerpretation accuracy.

In addition to error inherent in a single photointerpretation event, inconsistencies also exist from one individual to another (Edwards and Lowell, 1996), and for the same individual from one occasion to another (Nantel, 1993). Interpretor error can significantly affect results when comparing maps for temporal trends (Ward et al., 1997). Artificial intelligence approaches for image classification such as a DCNN are likely to be more consistent over time versus traditional photointerpretation methods.

3.4. Future work

This study aimed to retrieve seagrass extent in coastal waters. However, satellite imagery has also demonstrated utility for estimation of leaf area index (LAI) and biomass (Dierssen et al., 2003; Hill et al., 2014), which could aid in addressing uncertainty regarding global estimates of seagrass carbon storage. Moreover, the image processing and classification regime presented here could be used to monitor additional water quality parameters, such as chlorophyll. Future work testing this approach for other applications would require extensive field data for validation.

Ongoing work is focused on testing whether ROIs defined for each class for a single area of interest can be reused in other scenes from that same area of interest, or if ROIs defined for each class for a single area of interest can be reused in other areas of interest. Islam et al. (2020) suggests promise in this pursuit by successfully defining a generalizable DCNN model for seagrass detection from one location to another. Excellent performance was achieved by utilizing labeled samples from new environments to adapt a previously trained classifier. Additionally, extensive evaluation of which machine learning algorithms are best for seagrass detection is planned for future efforts.

Applicability of the proposed processing regime to 4-band sensors was shown here, but the incorporation of additional sensors could improve temporal resolution as compared to commercial platforms. Future work should focus on expanding the presented methods to openly available imagery from sensors such as the Landsat series and Sentinel-2. The Landsat series offers a longer imagery archive than either of the platforms presented here, and Sentinel-2 offers consistent temporal coverage with a revisit frequency of 2 to 3 days.

4. Conclusions

A reproducible workflow was developed to process commercial satellite imagery from WorldView-2 and RapidEye. This workflow transforms basic, level 1B imagery into an atmospherically corrected product. Corrected imagery were compared to field observations of R_{rs}. ENVI/IDL source code and associated documentation accompanying this workflow can be found at doi:10.23719/1518572. WorldView-2 imagery indicated higher disagreement and a positive bias in shorter wavelengths, particularly the coastal blue and blue spectral bands. Longer wavelengths had lower disagreement and a slight negative bias. RapidEye imagery showed lower overall disagreement, and a slight positive bias compared to field data. Despite spectral and spatial differences, image classification via a DCNN demonstrated nearly 97% agreement for both satellite platforms compared to aerial photointerpretation, although neither the satellite classification nor the aerial photointerpretation were validated through ground measurements. Methods were tested at two additional Florida sites, St. George Sound and Tampa Bay, and results demonstrated visual agreement with the imagery, suggesting the presented methods can be transferable to other locations.

REFERENCES

Baumstark, R., Dixon, B., Carlson, P., Palandro, D., Kolasa, K., 2013. Alternative spatially enhanced integrative techniques for mapping seagrass in Florida's marine ecosystem. International Journal of Remote Sensing 34, 1248–1264. doi:10.1080/01431161.2012.721941.

Baumstark, R., Duffey, R., Pu, R., 2016. Mapping seagrass and colonized hard bottom in Springs Coast, Florida using WorldView-2 satellite imagery. Estuarine, Coastal and Shelf Science 181, 83–92. doi:https://doi.org/10.1016/j.ecss.2016.08.019.

Bishop, C.M., 2006. Pattern recognition and machine learning. Springer, New York, NY. URL: http://cds.cern.ch/record/998831.

Björk, M., Short, F., Mcleod, E., Beer, S., 2008. Managing Seagrasses for Resilience to Climate Change. Technical Report. IUCN. Gland, Switzerland.

CEC, 2016. North America's Blue Carbon: Assessing Seagrass, Salt Marsh and Mangrove Distribution and Carbon Sinks. Technical Report. Commission for Environmental Cooperation. Montreal, Canada.

Chander, G., Haque, M.O., Sampath, A., Brunn, A., Trosset, G., Hoffmann, D., Roloff, S., Thiele, M., Anderson, C., 2013. Radiometric and geometric assessment of data from the RapidEye constellation of satellites. International Journal of Remote Sensing 34, 5905–5925. doi:10.1080/01431161.2013.798877.

Chavez, P.S., 1988. An improved dark-object subtraction technique for atmospheric scattering correction of multispectral data. Remote Sensing of Environment 24, 459–479. doi:https://doi.org/10.1016/0034-4257(88)90019-3.

Chollet, F., 2015. keras. URL: https://github.com/fchollet/keras%7D%7D.

Cohen, J., 1960. A coefficient of agreement for nominal scales. Educational and Psychological Measurement 20, 37–46. doi:10.1177/001316446002000104.

Collin, A., Hench, J.L., 2012. Towards Deeper Measurements of Tropical Reefscape Structure Using the WorldView-2 Spaceborne Sensor. Remote Sensing 4, 1425–1447. doi:10.3390/rs4051425.

Congalton, R.G., 1991. A review of assessing the accuracy of classifications of remotely sensed data. Remote Sensing of Environment 37, 35–46. doi:https://doi.org/10.1016/0034-4257(91)90048-B.

Conmy, R.N., Schaeffer, B.A., Schubauer-Berigan, J., Aukamp, J., Duffy, A., Lehrter, J.C., Greene, R.M., 2017. Characterizing light at547 tenuation within Northwest Florida

Estuaries: Implications for RESTORE Act water quality monitoring. Marine Pollution Bulletin 114, 995–1006. doi:https://doi.org/10.1016/j.marpolbul.2016.11.030.

Coppin, P., Jonckheere, I., Nackaerts, K., Muys, B., Lambin, E., 2004. Digital change detection methods in ecosystem monitoring: a review. International Journal of Remote Sensing 36, 1565–1596. doi:https://doi.org/10.1080/0143116031000101675.

Curcio, J.A., 1961. Evaluation of Atmospheric Aerosol Particle Size Distribution from Scattering Measurements in the Visible and Infrared. Journal of the Optical Society of America 51, 548–551. doi:10.1364/JOSA.51.000548.

Dadon, A., Ben-Dor, E., Beyth, M., Karnieli, A., 2011. Examination of spaceborne imaging spectroscopy data utility for stratigraphic and lithologic mapping. Journal of Applied Remote Sensing 5, 1–15. URL: https://doi.org/10.1117/1.3553234.

Danielson, J., Gesch, D., 2011. Global Multi-resolution Terrain Elevation Data 2010 (GMTED2010). Technical Report. U.S. Geological Survey Open-File Report 2011-1073. URL: http://pubs.usgs.gov/of/2011/10pdf/of2011-1073.pdf.

Dekker, A., Brando, V., Anstee, J., Fyfe, S., Malthus, T., Karpouzli, E., 2006. Remote Sensing of Seagrass Ecosystems: Use of Spaceborne and Airborne Sensors, in: Larkum, A., Orth, R., Duarte, C. (Eds.), Seagrasses: Biology, Ecology and Conservation. Springer Netherlands, Dordrecht, pp. 347–359.

Dekker, A.G., Brando, V.E., Anstee, J.M., 2005. Retrospective seagrass change detection in a shallow coastal tidal Australian lake. Remote Sensing of Environment 97, 415–433. doi:https://doi.org/10.1016/j.rse.2005.02.017.

Dierssen, H.M., Zimmerman, R.C., Leathers, R.A., Downes, T.V., Davis, C.O., 2003. Ocean color remote sensing of seagrass and bathymetry in the Bahamas Banks by high-resolution airborne imagery. Limnology and Oceanography 48, 444–455. URL: https://doi.org/10.4319/lo.2003.48.1_part_2.0444.

Duarte, C.M., 2017. Reviews and syntheses: Hidden forests, the role of vegetated coastal habitats in the ocean carbon budget. Biogeosciences 14, 301–310. doi:10.5194/bg-14-301-2017.

Duarte, C.M., Losada, I.J., Hendriks, I.E., Mazarrasa, I., Marbà, N., 2013. The role of coastal plant communities for climate change mitigation and adaptation. Nature Climate Change 3, 961–968. doi:10.1038/nclimate1970.

Edwards, G., Lowell, K., 1996. Modeling Uncertainty in Photointerpreted Boundaries. Photogrammetric Engineering and Remote Sensing 62, 377–390.

ESRI, 2016. ArcGIS Desktop: Release 10.5.

Fauzan, M.A., Kumara, I.S.W., Yogyantoro, R., Suwardana, S., Fadhilah, N., Nurmalasari, I., Apriyani, S., Wicaksono, P., 2017. Assessing the Capability of Sentinel-2A Data for Mapping Seagrass Percent Cover in Jerowaru, East Lombok. The Indonesian Journal of Geography 49, 195–203. doi:http://dx.doi.org/10.22146/ijg.28407.

Fourqurean, J.W., Duarte, C.M., Kennedy, H., Marbà, N., Holmer, M., Mateo, M.A., Apostolaki, E.T., Kendrick, G.A., Krause-Jensen, D., McGlathery, K.J., Serrano, O., 2012. Seagrass ecosystems as a globally significant carbon stock. Nature Geoscience 5, 505–509. doi:10.1038/ngeo1477.

Goodman, L.A., Kruskal, W.H., 1954. Measures of Association for Cross Classifications. Journal of the American Statistical Association 49, 732–764. doi:10.1080/01621459.1954.10501231.

Great Britain, 2009. Ordnance Survey. EDINA Digimap Ordnance Survey Service. OS Code-Point with Polygons [Shapefile geospatial data] Aberdeen District. Updated May 2008. URL: http://edina.ac.uk/digimap.

Green, E.P., Mumby, P.J., Edwards, A.J., Clark, C.D., 1996. A review of remote sensing for the assessment and management of tropical coastal resources. Coastal Management 24, 1–40. doi:10.1080/08920759609362279.

Green, E.P., Mumby, P.J., Edwards, A.J., Clark, C.D., 2000. Remote sensing handbook for tropical coastal management.

Hill, V.J., Zimmerman, R.C., Bissett, W.P., Dierssen, H., Kohler, D.D.R., 2014. Evaluating Light Availability, Seagrass Biomass, and Productivity Using Hyperspectral Airborne Remote Sensing in Saint Joseph's Bay, Florida. Estuaries and Coasts 37, 1467–1489. doi:10.1007/s12237-013-9764-3.

Hossain, M.S., Bujang, J.S., Zakaria, M.H., Hashim, M., 2015. Application of Landsat images to seagrass areal cover change analysis for Lawas, Terengganu and Kelantan of Malaysia. Continental Shelf Research 110, 124–148. doi:https://doi.org/10.1016/j.csr.2015.10.009.

Huang, H., Roy, D., Boschetti, L., Zhang, H., Yan, L., Kumar, S., Gomez-Dans, J., Li, J., 2016. Separability Analysis of Sentinel-2A Multi-Spectral Instrument (MSI) Data for Burned Area Discrimination. Remote Sensing 8, 873. doi:https://doi.org/10.3390/rs8100873.

Islam, K.A., Hill, V., Schaeffer, B., Zimmerman, R., Li, J., 2020. Semi-supervised adversarial domain adaptation for seagrass detection using multispectral images in coastal areas. Data Science and Engineering.

Islam, K.A., Pérez, D., Hill, V., Schaeffer, B., Zimmerman, R., Li, J., 2018. Seagrass Detection in Coastal Water Through Deep Capsule Networks, in: Lai, J.H., Liu, C.L., Chen, X., Zhou, J., Tan, T., Zheng, N., Zha, H. (Eds.), Pattern Recognition and Computer Vision, Springer International Publishing, Cham. pp. 320–331.

Knudby, A., Nordlund, L., 2011. Remote sensing of seagrasses in a patchy multi-species environment. International Journal of Remote Sensing 32, 2227–2244. doi:10.1080/01431161003692057.

Kovacs, E., Roelfsema, C., Lyons, M., Zhao, S., Phinn, S., 2018. Seagrass habitat mapping: how do Landsat 8 OLI, Sentinel-2, ZY-3A, and Worldview-3 perform? Remote Sensing Letters 9, 686–695. doi:10.1080/2150704X.2018.1468101.

Krizhevsky, A., Sutskever, I., Hinton, G.E., 2012. ImageNet Classification with Deep Convolutional Neural Networks, in: Pereira, F., Burges, C.J.C., Bottou, L., Weinberger, K.Q. (Eds.), Advances in Neural Information Processing Systems 25. Curran Associates, Inc., pp. 1097–1105.

Kuester, M., 2017. Absolute Radiometric Calibration: 2016v0. Technical Report. DigitalGlobe.

Kuhn, M., Wing, J., Weston, S., Williams, A., Keefer, C., Engelhardt, A., Cooper, T., Mayer, Z., Kenkel, B., R Core Team, Benesty, M., Lescarbeau, R., Ziem, A., Scrucca, L., Tang, Y., Candan, C., Hunt, T., 2020. caret: Classification and Regression Training. URL: https://github.com/topepo/caret/.

Latif, Z.A., Zamri, I., Omar, H., 2012. Determination of tree species using Worldview-2 data, in: 2012 IEEE 8th International Colloquium on Signal Processing and its Applications, pp. 383–387. doi:10.1109/CSPA.2012.6194754.

Lyons, M., Phinn, S., Roelfsema, C., 2011. Integrating Quickbird Multi-Spectral Satellite and Field Data: Mapping Bathymetry, Seagrass Cover, Seagrass Species and Change in Moreton Bay, Australia in 2004 and 2007. Remote Sensing 3, 42–64. doi:10.3390/rs3010042.

Machwitz, M., Giustarini, L., Bossung, C., Frantz, D., Schlerf, M., Lilienthal, H., Wandera, L., Matgen, P., Hoffmann, L., Udelhoven, T., 2014. Enhanced biomass prediction by assimilating satellite data into a crop growth model. Environmental Modelling & Software 62. doi:10.1016/j.envsoft.2014.08.010.

Maxar, 2019. System-Ready Imagery. URL: https://www.digitalglobe.com/resources.

McFeeters, S.K., 1996. The use of the Normalized Difference Water Index (NDWI) in the delineation of open water features. International Journal of Remote Sensing 17, 1425–1432. doi:10.1080/01431169608948714.

McHugh, M.L., 2012. Interrater reliability: the kappa statistic. Biochemia medica 22, 276–282. URL: https://www.ncbi.nlm.nih.gov/pmc/articles/PMC3900052/.

McKenzie, L.J., Finkbeiner, M.A., Kirkman, H., 2001. Methods for mapping seagrass distribution, in: Short, F.T., Coles, R.G. (Eds.), Global Seagrass Research Methods.

Elsevier Science, Amsterdam. chapter 5, pp. 101–121. URL: https://doi.org/10.1016/B978-044450891-1/50006-2.

Meehan, A.J., Williams, R.J., Watford, F.A., 2005. Detecting trends in seagrass abundance using aerial photograph interpretation: Problems arising with the evolution of mapping methods. Estuaries 28, 462–472. URL: https://doi.org/10.1007/BF02693927, doi:10.1007/BF02693927.

Mélin, F., Sclep, G., Jackson, T., Sathyendranath, S., 2016. Uncertainty estimates of remote sensing reflectance derived from comparison of ocean color satellite data sets. Remote Sensing of Environment 177, 107–124. doi:https://doi.org/10.1016/j.rse.2016.02.014.

Meyer, C.A., Pu, R., 2012. Seagrass resource assessment using remote sensing methods in St. Joseph Sound and Clearwater Harbor, Florida, USA. Environmental Monitoring and Assessment 184, 1131–1143. doi:10.1007/s10661-011-2028-4.

Mumby, P., Green, E., Edwards, A., Clark, C., 1997. Measurement of seagrass standing crop using satellite and digital airborne remote sensing. Marine Ecology Progress Series 159, 51–60.

Nantel, J., 1993. A new and improved digitizing method based on the Thiessen (Voronoi) algorithm. Proceedings Sixth Annual Genasys International Users Conference, Fort Collins, Colorado, 12–25.

Pasqualini, V., Pergent-Martini, C., Pergent, G., Agreil, M., Skoufas, G., Sourbes, L., Tsirika, A., 2005. Use of SPOT 5 for mapping seagrasses: An application to Posidonia oceanica. Remote Sensing of Environment 94, 39–45. doi:https://doi.org/10.1016/j.rse.2004.09.010.

Phinn, S., Roelfsema, C., Dekker, A., Brando, V., Anstee, J., 2008a. Mapping seagrass species, cover and biomass in shallow waters: An assessment of satellite multi-spectral and airborne hyper-spectral imaging systems in Moreton Bay (Australia). Remote Sensing of Environment 112, 3413–3425. doi:https://doi.org/10.1016/j.rse.2007.09.017.

Phinn, S., Roelfsema, C., Dekker, A., Brando, V., Anstee, J., 2008b. Mapping seagrass species, cover and biomass in shallow waters: An assessment of satellite multi-spectral and airborne hyper-spectral imaging systems in Moreton Bay (Australia). Remote Sensing of Environment 112, 3413–3425. doi:https://doi.org/10.1016/j.rse.2007.09.017.

Photo Science Inc. Panhandle_Seagrass_2010. vector digital data. URL: \fwc-spfs1_2013_Update_Seagrass_2010.shp.

Planet Labs Inc., 2019. Planet Imagery Product Specifications. Technical Report. URL: https://assets.planet.com/docs/Planet_Combined_Imagery_Product_Specs_letter_screen.pdf.

Planet Team, 2017. Planet Application Program Interface: In Space for Life on Earth. San Francisco, CA. URL: https://api.planet.com.

Pottier, C., Garçon, V., Larnicol, G., Sudre, J., Schaeffer, P., Le Traon, P.Y., 2006. Merging SeaWiFS and MODIS/Aqua ocean color data in North and Equatorial Atlantic using weighted averaging and objective analysis. IEEE transactions on geoscience and remote sensing 44, 3436–3451.

Pu, R., Bell, S., 2013. A protocol for improving mapping and assessing of seagrass abundance along the West Central Coast of Florida using Landsat TM and EO-1 ALI/Hyperion images. ISPRS Journal of Photogrammetry and Remote Sensing 83, 116–129. doi:https://doi.org/10.1016/j.isprsjprs.2013.06.008.

Pu, R., Bell, S., Meyer, C., 2014. Mapping and assessing seagrass bed changes in Central Florida's west coast using multitemporal Landsat TM imagery. Estuarine, Coastal and Shelf Science 149, 68–79. doi:https://doi.org/10.1016/j.ecss.2014.07.014.

Pu, R., Bell, S., Meyer, C., Baggett, L., Zhao, Y., 2012. Mapping and assessing seagrass along the western coast of Florida using Landsat TM and EO-1 ALI/Hyperion imagery. Estuarine, Coastal and Shelf Science 115, 234–245. doi:https://doi.org/10.1016/j.ecss.2012.09.006.

Python Core Team, 2015. Python: A dynamic, open source programming language. URL: https://www.python.org/.

R Core Team, 2017. R: A Language and Environment for Statistical Computing. URL: http://www.R-project.org/.

Roelfsema, C.M., Lyons, M., Kovacs, E.M., Maxwell, P., Saunders, M.I., Samper-Villarreal, J., Phinn, S.R., 2014. Multi-temporal mapping of seagrass cover, species and biomass: A semi-automated object based image analysis approach. Remote Sensing of Environment 150, 172–187. doi:https://doi.org/10.1016/j.rse.2014.05.001.

Roelfsema, C.M., Phinn, S.R., Udy, N., Maxwell, P., 2009. An integrated field and remote sensing approach for mapping Seagrass Cover, Moreton Bay, Australia. Journal of Spatial Science 54, 45–62. doi:10.1080/14498596.2009.9635166.

Rutchey, K., Vilchek, L., 1999. Air Photointerpretation and Satellite Imagery Analysis Techniques for Mapping Cattail Coverage in a Northern Everglades Impoundment. American Society for Photogrammetry and Remote Sensing 65, 185–191.

Schaeffer, B., Myer, 2020. Resolvable estuaries for satellite derived water quality within the continental United States. Remote Sensing Letters.

Schaeffer, B.A., Schaeffer, K.G., Keith, D., Lunetta, R.S., Conmy, R., Gould, R.W., 2013. Barriers to adopting satellite remote sensing for water quality management. International Journal of Remote Sensing 34, 7534–7544. doi:10.1080/01431161.2013.823524.

Slater, P.N., Doyle, F.J., Fritz, N.L., Welch, R., 1983. Photographic systems for remote sensing, in: Colwell, R.N. (Ed.), Manual of Remote Sensing. 2 ed. American Society of Photogrammetry, Falls Church, VA. chapter 6, pp. 231–291.

Statistics Canada, 2008. 2006 Census. Census subdivisions (cartographic boundary file gcsd000b06a_e). Indian Reserves in Canada. Created by McMaster University Library Lloyd Reeds Map Collection, using ArcView 3.2, as a subset of the original dataset with csdtype = IRI .

Tamondong, A.M., Blanco, A.C., Fortes, M.D., Nadaoka, K., 2013. Mapping of seagrass and other benthic habitats in Bolinao, Pangasinan using Worldview-2 satellite image, in: 2013 IEEE International Geoscience and Remote Sensing Symposium - IGARSS, pp. 1579–1582. doi:10.1109/IGARSS.2013.6723091.

Thalib, M.S., Nurdin, N., Aris, A., 2018. The Ability of Lyzenga's Algorithm for Seagrass Mapping using Sentinel-2A Imagery on Small Island, Spermonde Archipelago, Indonesia. IOP Conference Series: Earth and Environmental Science 165, 012028. doi:10.1088/1755-1315/165/1/012028.

Thierry, B., Lowell, K., 2001. An uncertainty-based method of photointerpretation. Photogrammetric Engineering and Remote Sensing 67, 65–72.

Traganos, D., Cerra, D., Reinartz, P., 2017. CubeSat-derived detection of seagrasses using Planet imagery following unmixing-based denoising: is small the next big? ISPRS - International Archives of the Photogrammetry, Remote Sensing and Spatial Information Sciences XLII-1/W1, 283–287. doi:10.5194/isprs-archives-XLII-1-W1-283-2017.

Traganos, D., Reinartz, P., 2017. Mapping Mediterranean seagrasses with Sentinel-2 imagery. Marine Pollution Bulletin 134, 197–209. doi:https://doi.org/10.1016/j.marpolbul.2017.06.075.

Traganos, D., Reinartz, P., 2018. Interannual Change Detection of Mediterranean Seagrasses Using RapidEye Image Time Series. Frontiers in Plant Science 9, 96. URL: https://www.frontiersin.org/article/10.3389/fpls.2018.00096.

Vanhellemont, Q., Ruddick, K., 2014. Turbid wakes associated with offshore wind turbines observed with Landsat 8. Remote Sensing of Environment 145, 105–115.

Vantrepotte, V., Mélin, F., 2011. Inter-annual variations in the SeaWiFS global chlorophyll a concentration (1997–2007). Deep Sea Research Part I: Oceanographic Research Papers 58, 429–441.

Ward, D.H., Markon, C.J., Douglas, D.C., 1997. Distribution and stability of eelgrass beds at Izembek Lagoon, Alaska. Aquatic Botany 58, 229–240. doi:https://doi.org/10.1016/S0304-3770(97)00037-5.

Ward, D.H., Morton, A., Tibbitts, T.L., Douglas, D.C., Carrera-González, E., 2003. Long-term change in eelgrass distribution at Bahía San Quintín, Baja California, Mexico, using satellite imagery. Estuaries 26, 1529. doi:10.1007/BF02803661.

Wicaksono, P., Hafizt, M., 2018. Dark target effectiveness for dark-object subtraction atmospheric correction method on mangrove above-ground carbon stock mapping. IET Image Processing 12, 582–587. doi:10.1049/iet-ipr.2017.0295.

Wicaksono, P., Lazuardi, W., 2018. Assessment of PlanetScope images for benthic habitat and seagrass species mapping in a complex optically shallow water environment. International Journal of Remote Sensing 39, 5739–5765. doi:10.1080/01431161.2018.1506951.

CHAPTER 5: CONCLUSION

This dissertation is comprised of three manuscripts which explore and support the use of satellite imagery for monitoring aquatic systems, including the use of publicly available imagery for assessing cyanobacterial blooms in inland freshwater ecosystems and the use of high-resolution, commercial imagery for mapping seagrass extent in coastal ecosystems. Results presented throughout these manuscripts are relevant for both remote sensing technologies and the ecosystems these technologies were used to monitor. This dissertation includes the first national scale analysis of cyanobacterial occurrence at over 2,000 inland lakes and of cyanobacterial frequency and abundance at nearly 700 drinking water sources. Additionally, the first semi-automated approach for processing commercial imagery from the WorldView-2, WorldView-3, and RapidEye satellites is presented as well as the first analysis of their radiometric performance in an aquatic system. Methods outlined in these manuscripts have immediate applicability to resource managers and stakeholders. Collaboration with individuals at the local, state, and national levels has led to direct implementation of the remote sensing methods presented here in monitoring protocol and has the potential to improve resource management and prioritization in the future.

Chapters 2 and 3 provide methods for assessing the occurrence (Chapter 2) and frequency (Chapter 3) of cyanobacterial blooms across over 2,000 large inland lakes and at nearly 700 drinking water intakes in the continental United States. These studies are some of the first to offer national-scale analyses of cyanobacterial blooms. Findings in Chapter 2 were particularly interesting in the South and Southeast climate regions, where cyanobacterial occurrence reached maximum values in the winter months and reached minimum values in the summer months which is contrary to the ecological patterns seen in the remaining climate regions (Coffer et al., 2020a). Future work will focus on investigating this phenomenon at a smaller spatial scale. The current hypothesis for explaining this pattern is that the cyanobacterial blooms are lower in the water column during the summer months, as to avoid long periods of direct sunlight, and thus are not as readily detectable by the satellite sensor. Cyanobacterial abundance measurements at multiple depths throughout the water column for lakes experiencing winter blooms and lakes not experiencing winter blooms will be needed to either support to refute this hypothesis.

Chapter 3 offered insight into the frequency of cyanobacterial blooms for nearly 700 drinking water sources across 44 states. However, this study considered only a subset of UCMR 4 observations (n = 99). Future work will focus on expanding this comparison to include all qualitative responses submitted as part of UCMR 4. This expanded comparison will provide additional data for supporting both the satellite algorithm used to quantify cyanobacterial abundance and the quality of the responses provided at each public water system. Moreover, as additional data become available, the trend analyses presented in Chapter 3 can be expanded to continue to monitor if cyanobacterial abundances are increasing, decreasing, or staying the same at drinking water sources.

Chapter 4 offered a semi-automated method for mapping seagrass in coastal systems using a case study at St. Joseph Bay in Florida (Coffer et al., 2020b). While agreement statistics were not presented, the efficacy of this approach was also demonstrated at St. George Sound and Tampa Bay, both in Florida. Future efforts are focused on expanding this effort across time and space.

More specifically, nine additional sites, one for each of the climate regions defined by Karl & Koss (1984), have been identified and will be used to demonstrate this approach across different locations, water types, and seagrass ecosystems. Additionally, quality flagging is being explored to improve the performance of the pixel-based classification in more optically complex systems. While these methods are still being improved, and limitations exist in both acquisition and bulk data processing and of high-resolution imagery, methods presented in Chapter 4 can help in refining global estimates of seagrass coverage. Combined with additional data, such maps could be used to quantify the amount of carbon currently store in seagrass ecosystems.

Results of this dissertation have immediate benefits to both the scientific community and water quality managers. A focus of this dissertation has been direct communication and involvement with stakeholders, including at the local, state, and national levels. This collaboration included both sharing of satellite-derived results and guidance on how to implement the methods themselves to allow stakeholders to continue to process imagery as additional data is collected by the satellites. Schaeffer et al. (2013) emphasized the need for researchers to take additional steps past publication to ensure environmental managers are equipped to apply the tools or methods suggested through scientific research. This direct communication and involvement has led to many applications of this research from a management perspective. Chapter 1 detailed several use cases of results for each of the three manuscripts. Additionally, after methods presented in Chapter 3 were used to assist the city of Salem, OR in understanding cyanobacterial frequency upstream of a drinking water intake, satellite imagery was included as an acceptable monitoring technique for cyanobacteria in Oregon Rule 333-061-0510 (2018). Results presented in Chapter

4 have been recommended by The Scientific and Technical Advisory Committee as a cost-effective approach for mapping seagrass systems in the Chesapeake Bay.

The work presented throughout this manuscript should be considered as a complement to field monitoring that has the potential to greatly improve the temporal and spatial coverage of water quality monitoring. Future efforts will focus on refining these approaches and on expanding their applications across space and time. Continued collaboration with stakeholders and decision makers will ensure methods presented here will continue to improve the efficiency of water quality monitoring and assist in improving both scientific understanding of these systems and in protecting human and ecosystem health.

REFERENCES

Coffer, M.M., Schaeffer, B.A., Darling, J.A., Urquhart, E.A. and Salls, W.B., 2020a. Quantifying national and regional cyanobacterial occurrence in US lakes using satellite remote sensing. Ecological Indicators, 111. https://doi.org/10.1016/j.ecolind.2019.105976.

Coffer, M.M., Schaeffer, B.A., Zimmerman, R.C., Hill, V., Li, J., Islam, K.A. and Whitman, P.J., 2020. Performance across WorldView-2 and RapidEye for reproducible seagrass mapping. Remote Sensing of Environment, 250. https://doi.org/10.1016/j.rse.2020.112036.

Karl, T., Koss, W.J., 1984. Regional and National Monthly, Seasonal, and Annual Temperature Weighted by Area, 1895–1983.

Schaeffer, B.A., Schaeffer, K.G., Keith, D., Lunetta, R.S., Conmy, R., Gould, R.W., 2013. Barriers to adopting satellite remote sensing for water quality management International Journal of Remote Sensing, 34, pp. 7534-7544. 10.1080/01431161.2013.823524.

APPENDICES

APPENDIX A: SUPPLEMENTAL MATERIAL ACCOMPANYING CHAPTER 2: QUANTIFYING NATIONAL AND REGIONAL CYANOBACTERIAL OCCURRENCE IN US LAKES USING SATELLITE REMOTE SENSING

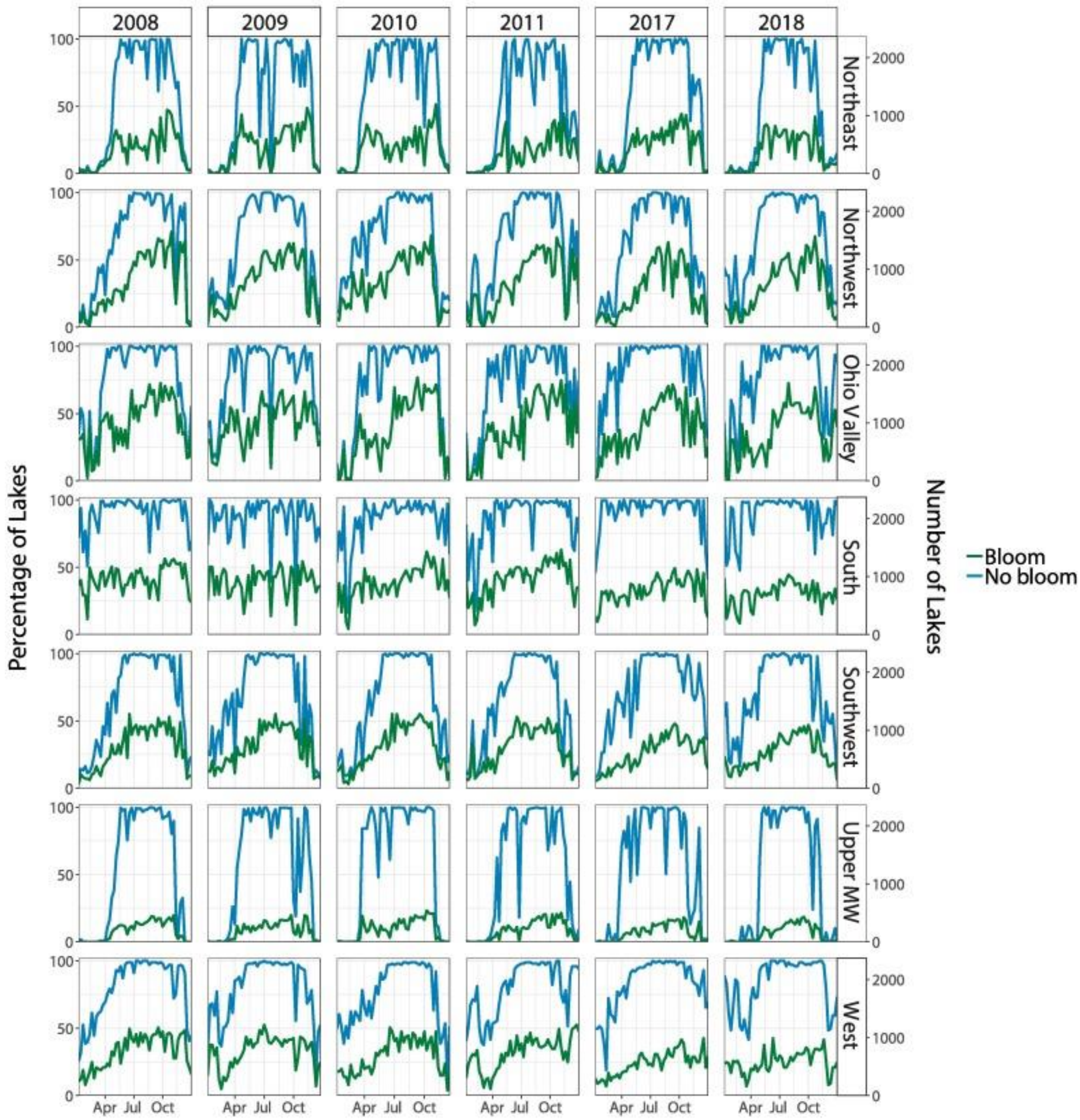

Figure A1. Stacked time series indicating the regional percentage (left axis) and number (right axis) of lakes experiencing a bloom and percentage of lakes not experiencing a bloom for each weekly composite from 2008 through 2011, 2017, and 2018. Results are based on a 10% minimum surface area threshold for a waterbody to be classified as experiencing a bloom. Climate regions include Northeast, Northwest, Ohio Valley, South, Southwest, Upper Midwest, and West. Results for the Northwestern Rockies & Plains and the Southeast are shown in **Figure 3**.

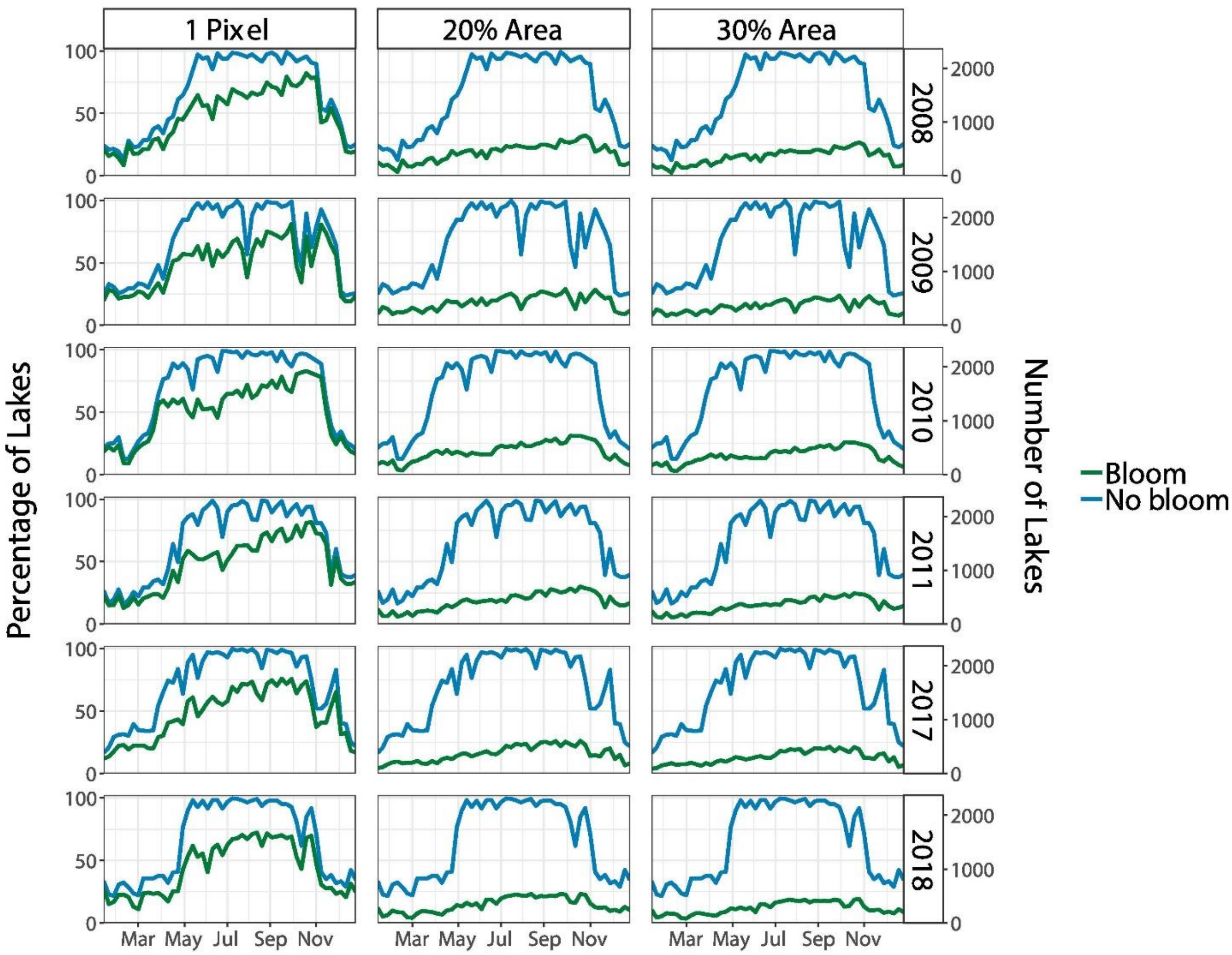

Figure A2. Stacked time series indicating the national percentage (left axis) and number (right axis) of lakes experiencing a cyanobacterial bloom (green) and not experiencing a cyanobacterial bloom (blue). Results are shown for each week for the years 2008 through 2011, 2017 and 2018 based on spatial area thresholds of 1 pixel, 20%, and 30%.

APPENDIX B: PERFORMANCES ACROSS WORLDVIEW-2 AND RAPIDEYE FOR REPRODUCIBLE SEAGRASS MAPPING

Text B1: An overview of deep convolutional neural networks (DCNN)

Deep convolutional neural networks (DCNN) have been successfully employed for seagrass detection in multispectral imagery (Islam et al., 2020). A DCNN is a deep learning approach which achieved state-of-the-art classification performances in many image recognition tasks (Krizhevsky et al., 2012). A DCNN typically consists of two types of layers: a convolutional layer and a fully connected layer. Convolutional layers use small kernals to filter the input image and extract useful features for classification. A fully connected layer is also referred to as a dense layer. Dense layers mimic the functionality of the traditional neural network for classification.

A DCNN model can have one or more convolutional layers depending on the complexity of the tasks. These layers can be thought of as feature identifiers are adept at extracting hierarchical features for classification. Lower layers extract low-level characteristics of the image such as edges, curves, and colors. Higher layers compute more complex features as different combinations of low-level features to achieve robust image classification. The final step before the classification layer is to flatten the model. Flattening transforms the features into a vector that can be fed into the dense layer for classification. The dense layer takes the vector and computes probabilities for the input image. Additionally, dropout layers are usually dispersed throughout the network, helping control overfitting. During training, if the output probabilities are incorrect, the errors are then backpropagated back to the model to adjust the model parameters. This process allows the model to slowly approach the optimum point where the model performs best.

In our experiments, instead of training the DCNN model on the full image, we used small subsets of the image to achieve pixel-wise classification. These subsets of the image are known as patches. We assigned a class label to each patch according to the center pixel of the patch. We extracted fifty thousand patches per class from the selected ROIs to train the DCNN model. Once trained, the model scanned across the entire image patch-by-patch to produce a pixel-wise classification of the entire image. We set the size of the patch to 3×3 and set the step size of the scanning process to one so that adjacent patches were overlapped during testing.

Table B1. Image information for WorldView-2 and RapidEye.

	WorldView	**RapidEye**
Satellite	WorldView-2	RapidEye-2
Collection date	14 Nov 2010	11 Nov 2010
Collection time	16:34 UTC	17:16 UTC
Pixel resolution	2 m	6.5 m
Cloud cover	3.0%	3.0%
Off nadir angle	15.6°	10.4°
Sun elevation	40.5°	42.8°
Image Source	DigitalGlobe	Planet

Table B2. Average mean absolute deviation (MAD) and mean bias for each spectral band, and for all spectral bands, across 24 field sites throughout St. Joseph Bay. A native resolution WorldView-2 image, a resampled WorldView-2 image, and a native resolution RapidEye image were considered.

	WorldView-2 (2 m)		**WorldView-2 (6.5 m)**		**RapidEye (6.5 m)**	
Band	**MAD**	**Bias**	**MAD**	**Bias**	**MAD**	**Bias**
Coastal	0.03254	0.03254	0.03256	0.03256		
Blue	0.02031	0.02031	0.02030	0.02030	0.00544	0.00544
Green	0.01104	0.01104	0.01099	0.01099	0.00528	0.00528
Yellow	0.00492	0.00492	0.00486	0.00486		
Red	0.00406	0.00406	0.00404	0.00404	0.00357	0.00357
Red edge	0.00059	-0.00021	0.00057	-0.00020	0.00329	0.00329
NIR #1	0.00113	-0.00113	0.00112	-0.00112	0.00329	0.00329
NIR #2	0.00077	-0.00077	0.00077	-0.00077		
Average	0.00942	0.00885	0.00940	0.00883	0.00422	0.00422

Table B3. Average mean absolute deviation (MAD) and mean bias for each field collection day at St. Joseph Bay. Field measurements were collected on 2, 6, and 9 Nov 2010. WorldView-2 imagery was collected on 14 Nov 2010, RapidEye imagery on 11 Nov 2010. A native resolution WorldView-2 image, a resampled WorldView-2 image, and a native resolution RapidEye image were considered.

	2 Nov 2010	**6 Nov 2010**	**9 Nov 2010**
WorldView-2 (2 m)			
MAD	0.01656	0.00862	0.00892
Bias	0.01553	0.00802	0.00845
WorldView-2 (6.5 m)			
MAD	0.01629	0.00863	0.00891
Bias	0.01530	0.00804	0.00845
RapidEye (6.5 m)			
MAD	0.00890	0.00341	0.00419
Bias	0.00890	0.00341	0.00419
Number of stations	2	11	11

Table B4. Seagrass area according to each classification in square kilometers.

FL FWC			**WorldView-2 DCNN**		**RapidEye DCNN**
Native shapefile	**Resample 2 m**	**Resample 6.5 m**	**Native res. 2 m**	**Resample 6.5 m**	**Native res. 6.5 m**
34.172	34.172	34.168	29.808	27.516	26.608

Table B5. Agreement matrices indicating the number of pixels classified as seagrass present and absent through satellite imagery and through aerial imagery. Areas classified as intertidal by the DCNN were removed before computing agreement statistics to correct for differences in tidal height at time of data collection.

FL FWC	**WorldView-2 (2 m)**			**WorldView-2 (6.5 m)**			**RapidEye (6.5 m)**		
	Present	**Absent**	**Total**	**Present**	**Absent**	**Total**	**Present**	**Absent**	**Total**
Present	6427271	1024833	7452104	573628	77643	651271	573326	56451	629777
Absent	442370	34245859	34688229	55738	3254251	3309989	94867	3277256	3372123
Total	6869641	35270692	42140333	629366	3331894	3961260	668193	3333707	4001900

Table B6. Agreement matrix indicating the number of pixels classified for each class through resampled WorldView-2 imagery and native resolution RapidEye imagery.

WorldView-2	**RapidEye**				
	Deep water	**Submerged sand**	**Seagrass**	**Intertidal**	**Land**
Deep water	2559353	16734	8086	0	8
Submerged sand	3913	411261	33105	30	0
Seagrass	3615	21842	598375	10080	10756
Intertidal	53	9	27564	165551	24125
Land	43	1	4320	8848	275695

Table B7. Agreement between machine learning classification of satellite imagery and photointerpretation of aerial imagery using just the blue, green, red, and NIR spectral bands to match the resolution of existing satellite missions. Areas classified as intertidal by the DCNN were removed before computing agreement statistics to correct for differences in tidal height at time of data collection.

	WV-2 (2 m)	**WV-2 (6.5 m)**	**RE (6.5 m)**
Overall accuracy	96%	96%	95%
Kappa coefficient	0.85	0.87	0.82